

Impact of Free Long Waves on Dune Erosion Predictions in Numerical Modelling

H.Daouk

This page is intentionally left blank

Impact of Free Long Waves on Dune Erosion

Predictions in Numerical Modelling

By

Haisam Daouk

to obtain the degree of

Master of Science in Hydraulic Engineering

at the Delft University of Technology,

to be defended publicly on Monday November 30, 2020 at 12:00 AM.

Student number: 4793390
Project duration: February 2020 – November 2020
Supervisor: Prof. dr. ir. A. Reniers
Thesis committee: Dr.IR. M.A. de Schipper, TU Delft
Dr. M.S.F. Tissier, TU Delft
Ir. G. Akrish, TU Delft

An electronic version of this thesis is available at <http://repository.tudelft.nl/>.

Epigraph

“

No man can reveal to you aught but that which already lies half
asleep in the dawning of your knowledge.

The teacher who walks in the shadow of the temple, among his
followers, gives not of his wisdom but rather of his faith and his
lovingness.

If he is indeed wise he does not bid you enter the house of his
wisdom, but rather leads you to the threshold of your mind.

The astronomer may speak to you of his understanding of space,
but he cannot give you his understanding.

The musician may sing to you of the rhythm which is in all space,
but he cannot give you the ear which arrests the rhythm nor the
voice that echoes it.

And he who is versed in the science of numbers can tell of the
regions of weight and measure, but he cannot conduct you thither.

For the vision of one man lends not its wings to another man.

And even as each one of you stands alone in God's knowledge, so
must each one of you be alone in his knowledge of God and in his
understanding of the Earth.

“

– *Khalil Gibran*

“

All models are wrong
But some are useful

“

– *George Box*

Preface

This thesis concludes the final piece to obtaining my Master of Science in Hydraulic Engineering at Delft University of Technology. The past two years have been a steep learning curve on both an academic and personal level. Despite only having one author on the title page, this thesis is the product of the continuous support from all of my closest friends and family who gave me the impetus to accomplish the goals I set out to achieve when I came to the Netherlands.

I would like to first and foremost offer the utmost gratitude to my parents, Salim and Iman, who throughout the 2-year process have been overwhelmingly enthusiastic, encouraging, and supportive. I am eternally grateful for their commitment in helping me succeed in my endeavours and develop myself on a more personal level.

I would also like to thank Omar, Adam, Sari, Mustafa, Ali, Nick, and Bahjat for the entertainment they bring me on a daily basis. My life would not be the same without our endless debates on politics sports, existential life questions, and music. It would have been nearly impossible to navigate these stressful times without our regular calls and your music recommendations.

I would like to thank Marco and Sjoerd, with whom I've enjoyed many pleasant talks and coffees. And my housemate Nisarg; together we have somehow managed to endure a pandemic whilst working on our theses and prepare some impeccable meals throughout. Anna to whom I owe a great deal of gratitude for her unrelenting support and motivation; we have enjoyed some great talks which have contributed immeasurably to my personal development. Nina, who pushes me to explore new facets of my life and is a sincerely great friend. And Sushruta for her infectious energy and happiness.

Finally, I would like to acknowledge my supervisor Ad Reniers for his guidance and passion in all things related to waves and the seas. I am truly grateful for the wisdom and expertise which you have shared with me throughout this process, and for accommodating my needs when I was confronted with hurdles along the way. I would also like to thank my graduation committee members, Marion Matthieu and Gal, for their constructive and hugely beneficial contributions during our meetings.

Haisam Daouk,
The Hague, November 2020

This page is intentionally left blank

Abstract

This report presents the methodology and findings of a study on the impacts of free long waves on dune erosion predictions in XBeach. In this paper a distinction is made between two types of infragravity waves: *bound infragravity waves* and *free infragravity waves*. *Bound infragravity waves* are generated by short-wave group forcings and are bound to the propagation of the wave groups. Conversely, *free waves* are infragravity waves that are released from the wave-group in the surfzone, reflect at the shoreline, and propagate back out of the surf zone. In a semi-enclosed basin with mild bathymetric changes such as the North Sea, free long waves that reflect off one coast can propagate large distances and impact other coastlines.

Modelling the response of a coastline during a storm event requires an offshore boundary condition that represents the incident short and long waves. The boundary condition for the incident infragravity waves is often derived by assuming a local equilibrium between the directionally spread sea-swell waves and bound infragravity waves following the K. Hasselmann (1962) method. This approach has proven to be problematic for two main reasons. First, the method tends to overestimate the incident infragravity wave height by assuming a local equilibrium is achieved at the model boundary; however, observations have shown that the transfer of energy from the short-wave groups to the underlying bound wave is gradual on a sloping bed. Second, by applying the equilibrium K. Hasselmann (1962) method it is implied that only bound infragravity waves are present at the boundary underestimating the total incident infragravity wave energy.

An analysis of XBeach in *surfbeat mode* revealed that the model can confidently predict infragravity wave behaviour on a natural beach slope with two well-developed bars during a storm event by calibrating the roller breaker slope coefficient and wave breaker coefficient. Infragravity wave heights were reasonably accurately predicted in the surfzone, but the model generally overpredicted the most energetic infragravity waves.

Further, the study investigated the impact of free infragravity waves on dune erosion predictions by simulating the behaviour of two 1D planar beach slopes to the inclusion of free long waves at the boundary. The study revealed that on a beach with a 1:35 slope the relative increase in dune erosion volume was 44.1% when the bound infragravity energy is equal to the free infragravity energy relative to the case excluding free waves. For the same conditions, a 20.6% increase was observed in the maximum runup. For a milder 1:70 slope a 36.4% and 6.1% increase in dune erosion and maximum runup was observed.

The results demonstrate that the dune response of a coastline is sensitive to the inclusion of incident free infragravity waves at the boundary. Moreover, neglecting the presence of free infragravity waves at the boundary may underpredict the dune response during a storm event.

Keywords: Infragravity waves, long waves, dune-erosion, XBeach, numerical modelling

List of Symbols and Abbreviations

IG	Infragravity	
rms	Root-mean square	
RMSE	Root-mean square error	
ss	Sea-swell	
WTI	<i>Wattelijk Toets Instrumentarium</i>	
A	Wave action density	$[\text{m}^2\text{Hz}^2\text{radian}^{-1}]$
A_{sb}, A_{ss}	Bed and suspended load coefficient	[-]
c	Wave celerity	$[\text{ms}^{-1}]$
c_g	Wave group celerity	$[\text{ms}^{-1}]$
C	Bound-wave interaction coefficient	[-]
C_{sed}	Depth-averaged sediment concentration	$[\text{m}^3\text{m}^{-3}]$
C_{eq}	Equilibrium sediment concentration	$[\text{m}^3\text{m}^{-3}]$
D_d	Wave breaking depth	[m]
D_h	Sediment diffusion coefficient	[-]
$D(\theta)$	Directional energy distribution	$[1/\text{rad}]$
D_{50}	Median grain size	$[\mu\text{m}]$
$E(f)$	Wave energy density	$[\text{m}^2\text{Hz}^{-1}]$
E_r	Roller energy	$[\text{kgs}^{-2}]$
f	Frequency	[Hz]
f_{peak}	Peak frequency	[Hz]
g	Gravitational acceleration	$[\text{ms}^{-2}]$
H_m	Maximum wave height	[m]
h	Water depth	[m]
h_x	Bed slope	$[\text{m}/\text{m}]$
H	Wave height	[m]
H_s	Significant wave height	[m]
H_{rms}	Root-mean square wave height	[m]
k	Wave number	$[\text{m}^{-1}]$
m_n	n^{th} order spectral moment	$[\text{m}^2]$ for $n=0$
m	Wave-energy distribution width	[-]
R	Roller area	$[\text{m}^2]$
r^2	Correlation coefficient	[-]

S_{xx}	Short wave radiation stress	[kgs ⁻²]
T_s	Sediment adaptation time	[s]
T_p	Peak period	[s]
\bar{u}	Wave-group averaged velocity	[ms ⁻¹]
u_{lo}	Low-frequency oscillatory component	[ms ⁻¹]
u_{hi}	High-frequency oscillatory component	[ms ⁻¹]
U_{cr}	Critical entrainment velocity	[ms ⁻¹]
Z_{s0}	Surge-level	[m]
a	Wave amplitude	[m]
β_h	Normalized bed-slope	[-]
η	Water-surface elevation	[m]
θ	Wave direction	[degrees]
ρ	Water Density	[kgm ⁻³]
σ	Intrinsic frequency	[Hz]
τ_{roller}	Roller induced shear stress	[kgs ⁻² m ⁻¹]
ϕ_f	Wave phase	[radian]

Table of Contents

1	INTRODUCTION	1
1.1	PROBLEM STATEMENT	2
1.2	HYPOTHESIS	5
1.3	RESEARCH QUESTIONS	5
2	THEORETICAL BACKGROUND	6
2.1	INFRAGRAVITY WAVE GENERATION AND TRANSFORMATION	6
2.1.1	<i>Bound-Wave Theory</i>	6
2.1.2	<i>Moving Breakpoint Theory</i>	8
2.1.3	<i>Bore Merging Theory</i>	8
2.2	DUNE EROSION REGIMES	9
2.3	XBEACH MODEL EQUATIONS AND SETUP	12
2.3.1	<i>Governing Equations</i>	12
2.3.2	<i>Roller Energy Balance</i>	13
2.3.3	<i>Wave Breaking</i>	16
2.3.4	<i>Sediment Transport</i>	16
3	METHODOLOGY	18
3.1	PHASE I: COAST3D MODEL-DATA COMPARISON	18
3.1.1	<i>Coast -3D Field Measurement Campaign</i>	18
3.1.2	<i>Coast-3D Data Processing</i>	19
3.1.3	<i>Xbeach model at Egmond aan Zee</i>	20
3.1.4	<i>Boundary Conditions</i>	21
3.1.5	<i>Model-Data Comparison</i>	21
3.2	PHASE II: IMPACT OF FREE LONG WAVES ON DUNE-EROSION	24
3.2.1	<i>Model Profiles</i>	24
3.2.2	<i>Boundary conditions</i>	25
3.2.3	<i>Correlation coefficient</i>	28
3.2.4	<i>Model Setup</i>	30
3.2.5	<i>Wave runup and Dune Erosion Estimation</i>	31
4	RESULTS	32
4.1	PHASE I: COAST-3D MODEL-DATA COMPARISON	32
4.1.1	<i>Short Wave Pattern</i>	33
4.1.2	<i>Long Wave Pattern</i>	35
4.2	PHASE II: IMPACT OF FREE LONG WAVES ON DUNE EROSION	40
4.3	STEEP PROFILE	40

4.4	MILD PROFILE	44
4.5	STEEP AND MILD PROFILE COMPARISON	47
5	DISCUSSION	51
5.1	PHASE I: MODEL-DATA COMPARISON	51
5.2	PHASE II: IMPACT OF FREE LONG WAVES ON DUNE EROSION.....	52
6	CONCLUSION.....	54
7	RECOMMENDATIONS	56
8	APPENDIX A: MODEL RESULTS FOR THE OCTOBER 24, 1998 STORM EVENT	57

1 Introduction

With the growing need to address coastal resilience to flooding due to fluctuating climate patterns, a comprehensive understanding of the near-shore processes that impact dune erosion and wave runup are an imperative. However, field observations of waves in the surf zone and runup on beaches during extreme storm events are limited. Therefore, predictions of runup and dune erosion are largely based on empirical models derived from data sets of relatively milder conditions. Furthermore, the contribution of infragravity waves to morphological changes at the coastline is relatively poorly understood partially due to the lack of field observations of long waves (Ardhuin, Rawat, & Aucan, 2014; Bromirski, Sergienko, & MacAyeal, 2010; Kannberg, 2018). Additionally, it is relatively difficult to recreate field conditions that are conducive to infragravity wave formation in a laboratory setting, further complicating studies of low frequency waves. For this reason, numerical models such as XBeach have proven to be an attractive alternative to physical modelling. Numerical models offer researchers the opportunity to recreate field conditions and easily alter them to better understand infragravity wave generation and dissipation mechanisms and their effects on nearshore hydrodynamics and morphodynamics. However, numerical models require an offshore wave boundary condition that characterizes the wave climate entering the model domain. Hence, the aim of the following study is to investigate the impact of the imposed offshore boundary condition for long waves on the reliability and robustness of wave run-up and dune erosion predictions at the shoreline.

The frequency and directional spreading of propagating free surface waves leads to the formation of wave-groups. This in turn leads to water surface level modulations on the scale of the wave-group typically ranging from 25s to 250s which are referred to as infragravity waves (D. J. A. Roelvink & Reniers, 2011). The phenomenon was first recognized by Munk (1949) who identified a relation between low frequency motions along the shoreline with amplitudes proportional to incident short-wave groups. Tucker and Deacon (1950) were the first to identify a linear relation between the short-wave energy envelope and the infragravity wave amplitude. Subsequently, Biésel (1952) demonstrated that there was a 180° phase lag between the incident short-wave group and bound infragravity wave suggesting that there was a negative relationship between the wave height of the short-wave group and the mean water level. However, it was Longuet-Higgins and Stewart (1962) who later theorized that the water-surface modulations within the short-wave group were the result of the spatial variability of the short-wave momentum flux. As the short-wave groups propagate into the surf zone and begin breaking, the bound infragravity waves are subsequently released and reflect at the shoreline. Upon reflection at the coast the waves can propagate outside of the surf zone and are referred to as leaky (free) waves. Conversely, some waves are refractively trapped in the surf-zone, referred to as edge waves, and can lead to periodic alongshore-travelling patterns on

the coastline, such as beach cusps (A. Reniers, Roelvink, & Dongeren, 2001; A. J. H. M. Reniers, van Dongeren, Battjes, & Thornton, 2002).

Infragravity waves are abundant in the surfzone and can lead to the formation of rip-currents, contribute to wave run-up and dune erosion, and sediment transport amongst other phenomena (Bertin et al., 2018). However, the phenomena most relevant to this study are wave run-up and dune erosion. Several studies have shown that there is a significant contribution to wave run-up due to the extensive length of infragravity waves (Stockdon, Holman, Howd, & Sallenger, 2006). Additionally, it was observed by Guza and Thornton (1982) that on dissipative beaches wave run-up is dominated by infragravity waves. Therefore, in order to accurately model the morphodynamic response of a coastline during extreme storm conditions the energy contained in the infragravity wave band must be well represented at the boundary. Current numerical models such as XBeach compute the bound-long wave energy by employing the frequency directional spectrum equilibrium estimate introduced by K. Hasselmann (1962) which is dependent on the incoming short-wave climate imposed at the offshore boundary.

1.1 Problem Statement

In numerical models such as XBeach, infragravity-wave boundary conditions are imposed by assuming a local equilibrium between the directionally spread sea-swell wave forcing and the bound infragravity waves (K. Hasselmann, 1962; Longuet-Higgins & Stewart, 1962; A. J. H. M. Reniers et al., 2002). This approach has proven to be problematic in several cases. Bound wave solutions such as the K. Hasselmann (1962) approach lose their validity with increasing short-wave nonlinearity. Additionally, the transfer of energy between the short waves and long waves on a sloping bed is gradual and therefore the equilibrium solution is not met resulting in an overestimation of the incoming bound long wave energy. Moreover, the method implies that only bound long waves are present at the boundary which can underestimate the total incident long wave energy. Free infragravity waves can be generated at distant sources and propagate large distances before arriving at the model domain; therefore, it is difficult to predict and anticipate the free shoreward propagating infragravity waves in advance. Consequently, intermediate water depths ranging between 10-30m, where numerical model domain boundaries are frequently defined, are often dominated by directionally spread free infragravity waves. (Ardhuin et al., 2014; Bromirski et al., 2010; Fiedler, Smit, Brodie, McNinch, & Guza, 2019).

Several studies including Naporowski (2020) have demonstrated the prevalence of free infragravity waves in The North Sea to be significant. Naporowski (2020) observed surface elevation measurements at several wave buoys in The North Sea presented in Figure 1. Observations during the *Sinterklaas Storm*, which occurred towards the end of December 2013, were considered for the analysis. The water-surface elevation measurements were processed with a low-pass filter with a frequency cut-off of 0.005 Hz to capture the energy contained in the infragravity frequency band. The difference in the observed infragravity significant wave height and predicted bound infragravity wave height can be seen in panel B of Figure 2. From the difference in the observed significant infragravity wave height signal (blue) and predicted bound infragravity wave height signal (red) it is evident that there is a clear discrepancy between the two. This trend is further reinforced by the observations at station Q1, closer to the shoreline, shown in Figure 3. The observations demonstrate that only considering bound long waves in coastal models may considerably under-estimate the incoming long wave energy.

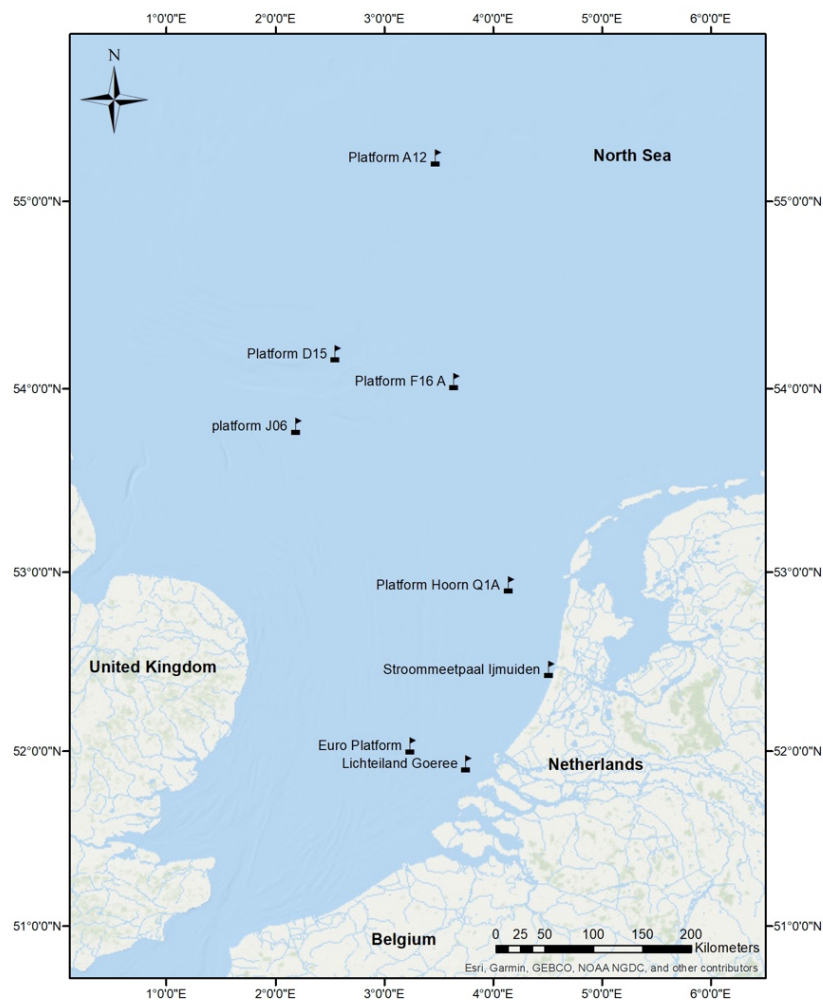


Figure 1: Wave measurement stations in the North Sea.

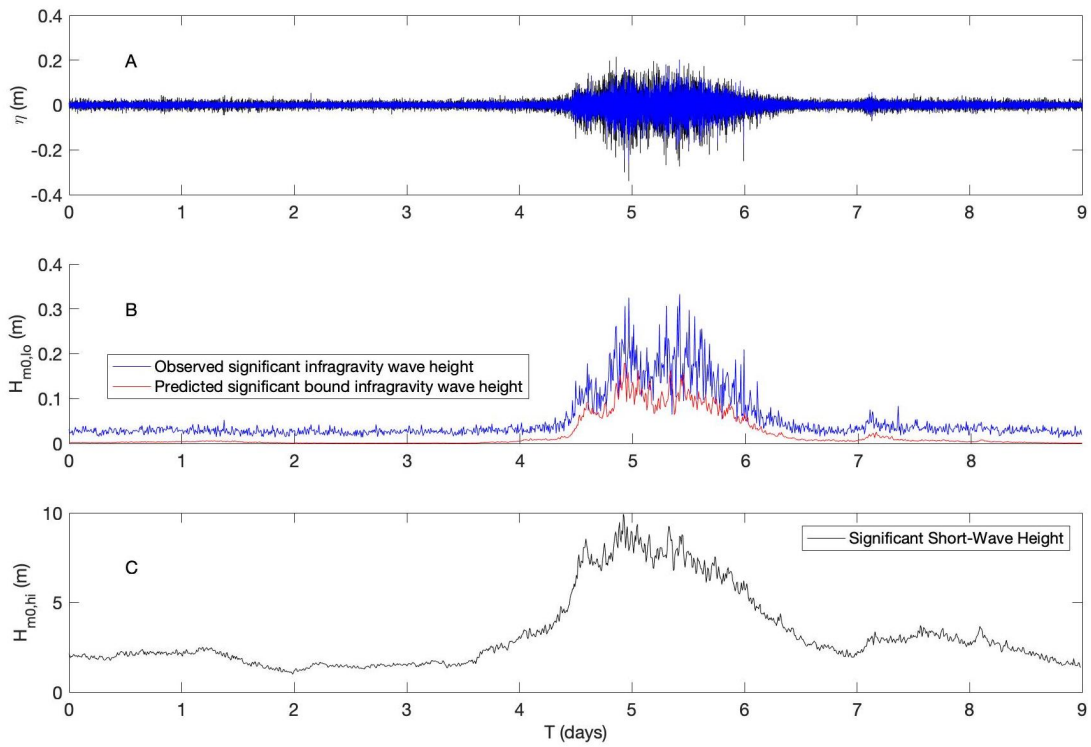


Figure 2: Infragravity observations at station A12 (Naporowski, 2020) where (A) water surface elevation; (B) long wave significant wave height; (C) short wave significant wave height.

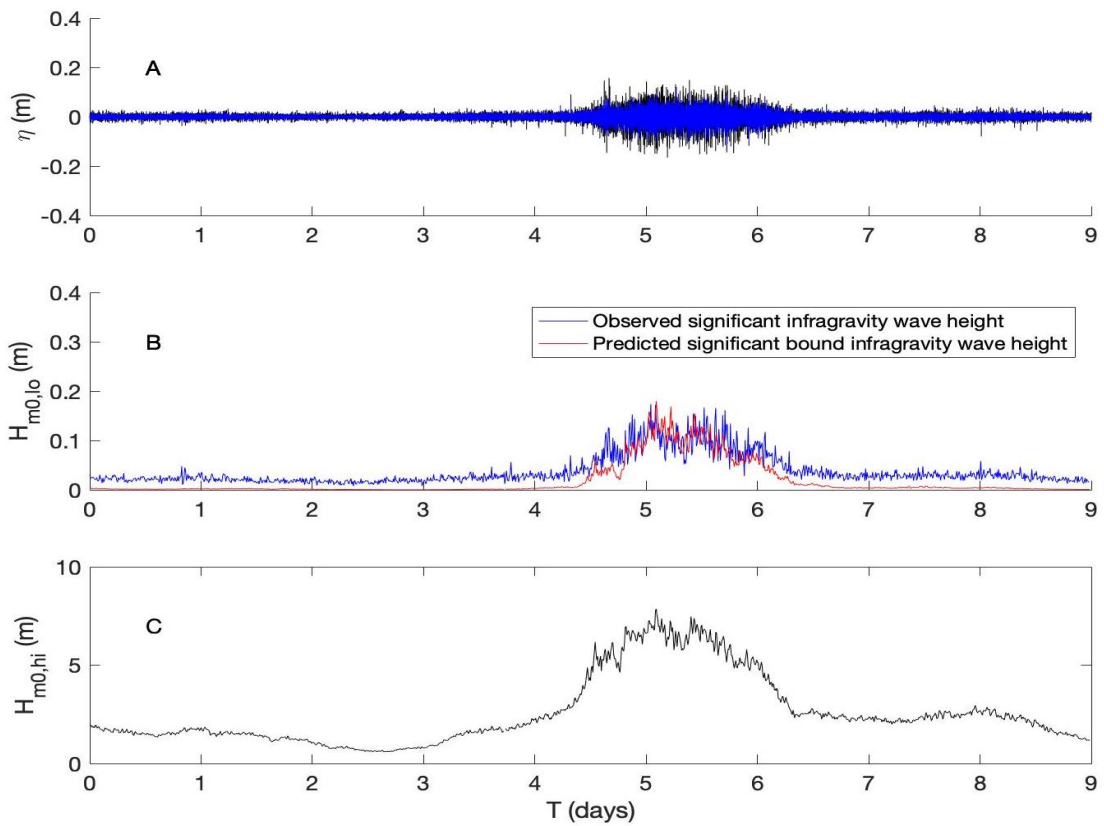


Figure 3: Infragravity observations at station Q1 (Naporowski, 2020). where (A) water surface elevation; (B) long wave significant wave height; (C) short wave significant wave height.

1.2 Hypothesis

The K. Hasselmann (1962) method assumes that an equilibrium condition is reached between the short-wave group and infragravity waves. However, for steep beaches changes in water depth and changes in the incident sea-swell waves are rapid and hence the equilibrium condition may not be satisfied. Ultimately, this will lead to an over-estimation of the infragravity wave height at the boundary. In addition, if free waves are not explicitly imposed at the offshore boundary of numerical models the only incoming long waves at the boundary are bound long waves. Nonetheless, Arduin et al. (2014) and Rawat et al. (2014) have demonstrated that infragravity waves that reflect against one coastline may travel large distances and impact other coasts. In basins such as the North Sea, where bathymetric changes are mild and gradual, a considerable portion of infragravity waves that reflect off one coast may travel and effect wave run-up and dune erosion on other coastlines. As a result, neglecting the contribution of free (leaky) infragravity waves may significantly under-estimate dune erosion predictions.

1.3 Research Questions

The overarching goal of this thesis is to understand the role of free infragravity wave boundary conditions imposed on offshore boundaries of numerical models such as XBeach, and thus the thesis will address two main research questions:

1. Can XBeach confidently predict the evolution of long waves in the surf zone during storm events?
2. What is the relative contribution of free infragravity waves imposed at the offshore boundary on dune erosion and wave run-up predictions during storm events?

2 Theoretical Background

Infragravity waves are formed by the spatial variability in short-wave momentum flux within a wave group. There are several other generation mechanisms that explain the energy transfer from the short-wave envelope to the infragravity waves namely: *bound wave*, *moving breakpoint*, and *Bore merging* theories. The three generation mechanisms and their respective impacts on the transformation and propagation of infragravity waves in the surf-zone is explained in the following section. In addition, dune erosion regimes and wave runup are pertinent to this study. The fundamental dune erosion mechanisms associated with long waves expected during storm events are explained and discussed.

2.1 Infragravity Wave Generation and Transformation

In the following section the various generation and transformation mechanisms of infragravity waves in the surf zone are outlined and explained. Furthermore, the governing equations and their respective relevance to the assessments pertinent to this study are elucidated.

2.1.1 Bound-Wave Theory

Due to the frequency dispersion relation of waves in deep water, short waves tend to travel in groups. As a result, the groupy behavior of waves forces secondary modulations of the water surface on the scale of the wave group. The spatial variability of the short-wave momentum flux within a wave group results in modulations of the water surface that propagate with, and are bound to, the wave group forcing and are called *bound infragravity waves*, see Figure 4. The term *bound* highlights the fact that the waves are confined to the propagation of the wave group in deep water; however, in the surf-zone the release of short-wave energy in the form of wave-breaking releases the bound long-wave.

In deep water the height of infragravity waves is small, on the order of 1cm (Bertin et al., 2018), due to the limited exchange of energy between the short-waves and the bound long wave. Longuet-Higgins and Stewart (1962) derived an equilibrium solution that relates the height of the resulting bound infragravity wave to the energy contained in the short-wave group envelope given by equation (1).

$$\eta(x, t) = \frac{-S_{xx}(x, t)}{\rho(gh - c_g^2)} + K \quad (1)$$

Where:

- S_{xx} [kgs⁻²] = Short wave radiation stress
- ρ [kgm⁻³] = Water density
- g [ms⁻²] = Gravitational acceleration
- h [m] = Mean water depth
- c_g [ms⁻¹] = Short wave group celerity
- K [-] = Constant

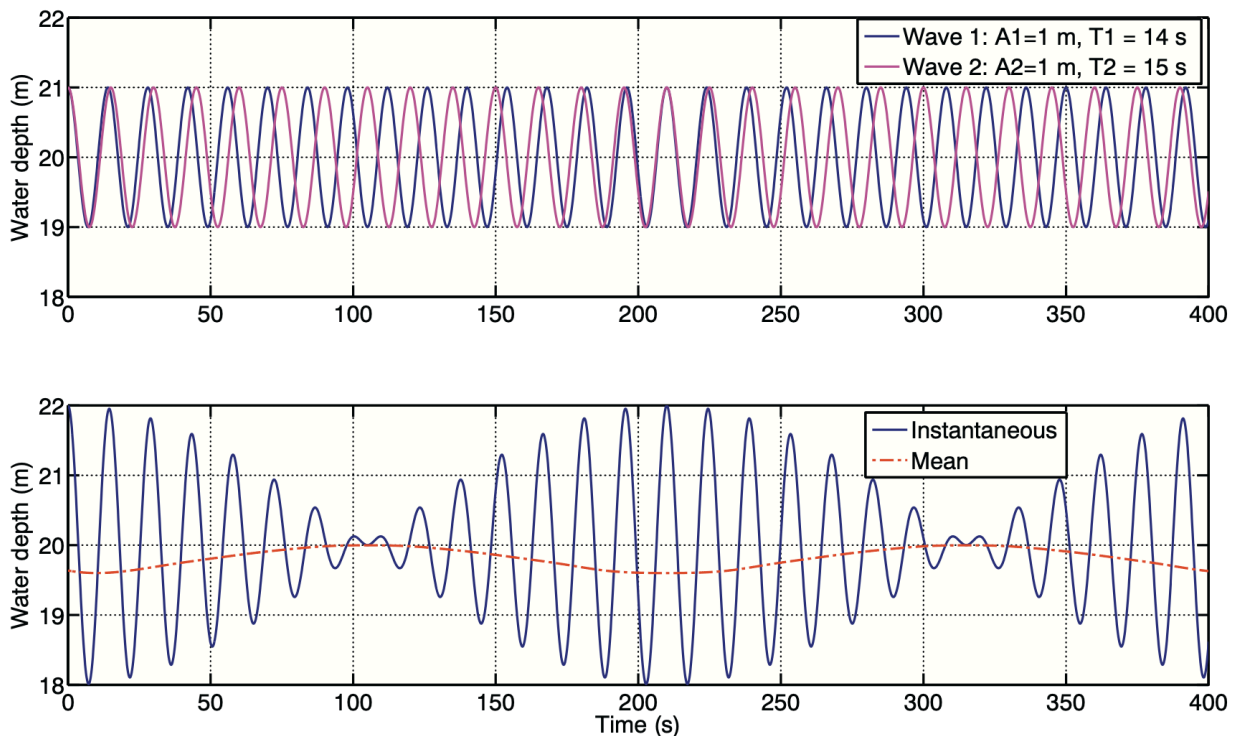


Figure 4: Time series of two sinusoidal waves and the resulting bound infragravity wave (Bertin et al., 2018).

The equilibrium solution proposed by Longuet-Higgins and Stewart (1962) is only applicable for a flat bottom, or for deep water conditions. For a sloping bottom the bound infragravity wave is no longer in equilibrium with the short-wave group and the bound wave begins to deviate from the 180° phase shift observed under equilibrium conditions, so the bound long wave is lagging behind the wave group (Bertin et al., 2018). The phase shift promotes the transfer of energy between the short waves and the underlying infragravity wave allowing the infragravity wave to grow in amplitude. It was theorized by van Dongeren et al. (2007) that the rate of growth of infragravity waves lies between the rate of conservative shoaling, referred to as Greens' Law, which is proportional to $h^{-\frac{1}{4}}$, and the

equilibrium solution proposed by Longuet-Higgins and Stewart (1962) ($h^{-\frac{5}{2}}$), where h refers to the water depth. As a result of this non-linear depth dependence, the *bound wave* generation mechanism is dominant in mildly sloping conditions. However, in a steep-slope beach regime the growth of infragravity waves is dominated by the *Moving Breakpoint* mechanism.

2.1.2 Moving Breakpoint Theory

The spatially varying short-wave height within a wave group means that the short-wave breakpoint varies in time as the wave group propagates in the surf zone. It follows that the largest waves in the wave group break before the smallest ones causing a time-variation of the radiation stress gradient in the surf zone which in turn results in a time-variation in the wave induced set-up (Symonds, Huntley, & Bowen, 1982). As the short waves propagate into the surf zone the waves shoal and increase in height, thus amplifying the variation in radiation stress within the wave group and increasing the amplitude of the bound infragravity wave. Subsequently, the waves begin to break as they approach the shoreline. As the short waves begin breaking, their energy is dissipated and the radiation stress is diminished, so the set-down effect also vanishes. In order to achieve a force equilibrium, the set-down is compensated by a water level setup at the shoreline (Symonds et al., 1982). The result is a gradual change from a standing wave at the shoreline to a seaward progressive wave offshore of the breaking point being created at infragravity frequencies (Bertin et al., 2018). Likewise, the shoaling and breaking of short waves in the surf zone leads to another mechanism that contributes to the amplification of infragravity waves known as *Bore Merging*.

2.1.3 Bore Merging Theory

After short waves propagate into the surf zone and begin breaking, the waves produce bores analogous to bores observed in a hydraulic jump. A bore can overtake the bore ahead of it and they can combine into a single larger wave front. This non-linear process leads to the formation of a resultant wave with a larger period - with respect to its constituents - in the surf zone and contributes to the transfer of energy to the infragravity spectrum. Based on field observations, Huntley and Bowen (1975) remarked that bore merging tends to be most prevalent in mildly sloping beaches due to the wide surf-zone.

2.2 Dune Erosion Regimes

In addition to infragravity wave generation mechanisms, dune erosion and cross-shore sediment transport mechanisms are pertinent to this study. During storm conditions dunes are especially vulnerable as a result of increased wave attack due to storm surge (Bosboom & Stive, 2015). The mechanisms by which dunes erode are fundamentally dictated by the level at which the waves attack with respect to the dune-foot level, which is determined by wave run-up and near-shore set-up, (A.H. Sallenger, 2000). A.H. Sallenger (2000) defined four distinct impact regimes that are categorized by comparing the wave run-up levels to the dune foot and dune crest levels. The various storm impact regimes are summarized in Table 1.

Table 1: Storm Impact Regimes (A.H. Sallenger, 2000)

<p>Swash Regime</p>	<ul style="list-style-type: none"> • Run-up is confined to the foreshore. • Foreshore typically erodes and sand is transported offshore. • After the storm, sand is gradually transported back onshore. 	
<p>Collision Regime</p>	<ul style="list-style-type: none"> • Run-up collides with the base of the foredune ridge. • The impact causes sand to be eroded from the dune and transported offshore. • Eroded sand is not readily restored to the dune. 	
<p>Overwash Regime</p>	<ul style="list-style-type: none"> • Run-up exceeds the level of the dune foot or berm. • Wave overtopping is expected occasionally. • Sediment is transported to the landward side of the dune. 	
<p>Inundation Regime</p>	<ul style="list-style-type: none"> • The elevation of the swash motion exceeds the level of the dune foot, and the entire dune is inundated. • Results in the landward migration of the dune. 	

Moreover, cross-shore sediment dynamics are highly topical and are governed by complex mechanisms which seldom have analytical solutions (Bosboom & Stive, 2015). Sediment transport formulations are often dominated by the third power of the flow velocity near the bed where the expected suspended sediment concentrations are highest. The near-bed flow velocity under a propagating wave group is comprised of three main components as described by equation 2 (J. A. Roelvink & Stive, 1989).

$$u = \bar{u} + u_{lo} + u_{hi} \quad (2)$$

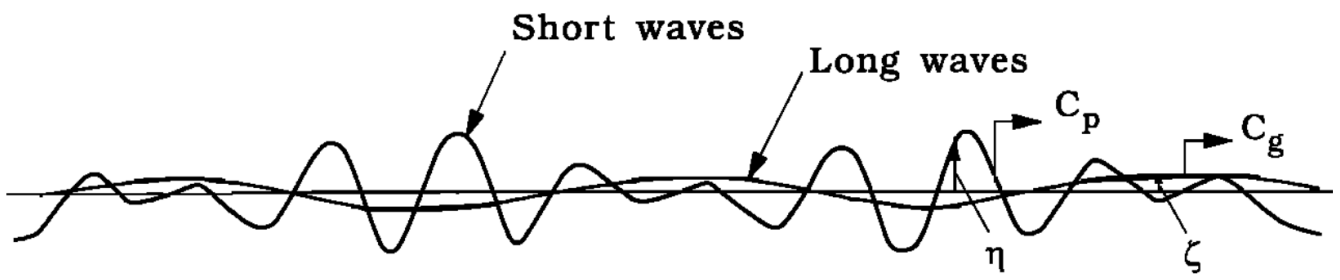
Where \bar{u} is the wave-group averaged component which is the under-tow flow velocity in the surf zone. Additionally, the components u_{lo} and u_{hi} are the oscillatory components corresponding the low and high frequency waves respectively. To distinguish between the relative contribution of the time-varying flow components the third odd velocity moment is considered. J. A. Roelvink and Stive (1989) demonstrated that the most significant contributions to the third odd velocity moment are given by the following relation:

$$\langle u|u|^2 \rangle = \underbrace{3\langle \bar{u}|u_{hi}|^2 \rangle}_{(1)} + \underbrace{\langle u_{hi}|u_{hi}|^2 \rangle}_{(2)} + \underbrace{3\langle u_{lo}|u_{hi}|^2 \rangle}_{(3)} \quad (3)$$

Where term (1) is related to transport by the mean current, (2) represents the contribution of the oscillatory component of the short wave instantaneous velocity, and (3) represents the interaction between the long wave velocity and short-wave velocity variance.

Beneath a long wave bound to a shoreward propagating wave group, the trough of the bound long wave coincides with the crests of the largest waves in the wave group, and hence the corresponding oscillatory flow components for the short and long waves are 180° out of phase as shown in Figure 5. The high frequency velocity component, corresponding to the short waves, is thought to stir the sediments up when the low frequency component corresponding to the bound wave is offshore directed resulting in a net offshore directed transport of sediments. The occurrence of this phenomenon is contingent on the 180° phase shift between the short and long waves. However, as the wave group propagates into the surf zone and the bound long wave is subsequently released at breaking, the phase relationship deviates from 180° resulting in a net onshore directed sediment transport contribution from the long waves.

Surface elevations:



Motion induced by long waves



Suspended sediment concentration.

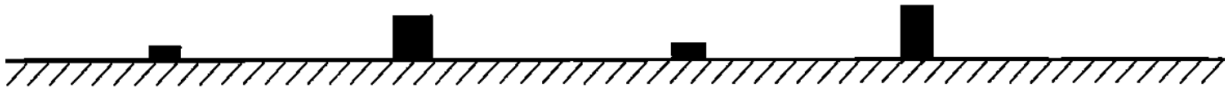


Figure 5: Offshore directed sediment transport under bound long waves (Deigaard, Jakobsen, & Fredsøe, 1999)

In addition, σ is the relative (or intrinsic) frequency defined as a function of space (x,y) and time (t) as per the following (Leo H. Holthuijsen, 2007):

$$\sigma(x, y, t) = \sqrt{g \cdot k(x, y, t) \tanh(k(x, y, t) \cdot h(x, y, t))} \quad (6)$$

In which k is the wave number and h is the water depth. The action balance equation consists of three main terms (L. H. Holthuijsen et al., 1989):

- (1) The Local rate of change of spectral action density.
- (2) The propagations terms including refraction and shoaling describe the net transport of action in the x , y , and θ .
- (3) The source term which envelopes the total generation and dissipation of wave action as a function of x , y , and θ .

2.3.2 Roller Energy Balance

Further relevant to this study is the roller energy balance adopted by XBeach. When short waves begin to break there is a short delay between the breaking of a wave, or the point at which the radiation stress gradients are greatest, and the resulting water-level setup and longshore current. This delay is explained by the presence of a roller which serves as a momentary storage of shoreward momentum. Furthermore, the roller promotes the spatial displacement of the short-wave energy, moving energy further into shallower water and enhancing the generation of infragravity waves. The development of infragravity waves in the surf zone is related to the transfer of energy from the short-wave frequencies to the long wave frequency band. This transfer of energy is facilitated by the infragravity wave generation mechanisms discussed in sections 2.1.1, 2.1.2, and 2.1.3. Hence, the model's ability to capture and reproduce the generation and propagation of infragravity waves in the surf zone is contingent on the model's ability to accurately reproduce short-wave breaking mechanisms.

A roller can be described as a disturbance of entrapped air and water, with section area R , that slides down a wave front, with wavelength L , of a breaking wave as shown in Figure 6. The tangent of the wave front at the interface between the undisturbed and disturbed water is represented by β . The slope of the wave front, β , dictates the storage of wave energy and momentum and is a user defined XBeach model input which by default is set to 0.1 . For relatively large values of β large

stresses are expected which corresponds to an instantaneous dissipation of energy resulting in a small roller area. Consequently, the roller doesn't develop and less energy is transported into shallow water. On the other hand, relatively small values of β result in a well-developed roller which promotes the transport of wave energy into shallow water depths. In a one-dimensional model, the absence of longshore currents can be counteracted by adjusting β to fine tune the infragravity response in the surf zone. (Longuet-Higgins & Turner, 1974; Nairn, Roelvink, & Southgate, 1991; A. J. H. M. Reniers & Battjes, 1997; J. A. Roelvink & Stive, 1989; Stive & Vriend, 1995; Svendsen, 1984).

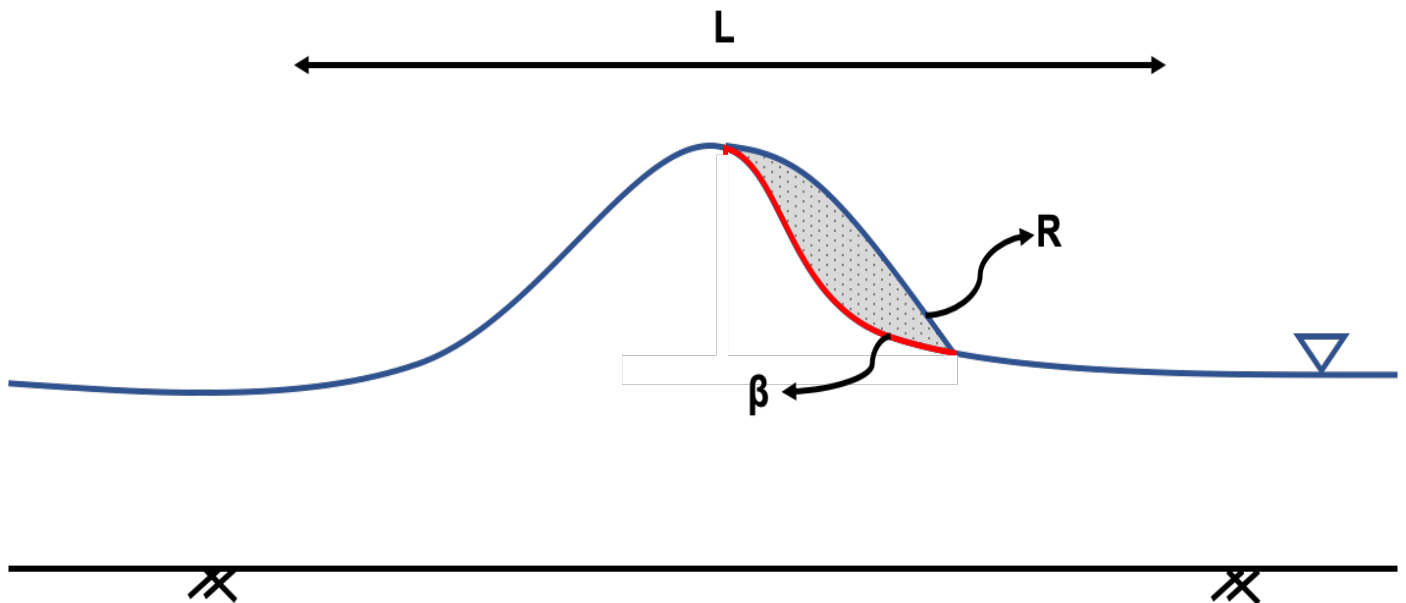


Figure 6: Schematization of wave roller

Fundamentally, wave-energy released at breaking is transferred to the roller energy which travels on the wave front with the same phase speed as the wave underneath. The disparity between the phase speed of the roller and the velocities of the water particles at the wave front results in a shear stress between the roller and the undisturbed water at the wave front. Therefore, the energy dissipated by the roller is equivalent to the work done by the shear stress at the interface between the roller and the wave front. The roller serves as a momentary storage of energy causing a spatial lag between the point at which the waves break and the point at which they subsequently dissipate their energy (Nairn et al., 1991). Henceforth, the roller exerts a shear stress, τ , on the water beneath it which is described by the relation given by (Duncan, 1981):

$$\tau_{roller} = \frac{\rho g \cdot R}{L} \cdot \beta_s \quad (7)$$

Additionally, the roller area, R , is related to the roller energy given by (Svendsen, 1984):

$$E_r = \frac{\rho R c^2}{2L} \quad (8)$$

Where c is the phase speed given by the linear dispersion relation:

$$c = \sqrt{\frac{g}{k} \tanh(kd)} \quad (9)$$

The roller contributes to the water-level setup and energy balance through the cross-shore momentum balance, the energy balance, and time-averaged wave energy balance (A. J. H. M. Reniers & Battjes, 1997). The contribution of the roller energy to the cross-shore radiation stress is given by the wave-averaged roller momentum flux (Svendsen, 1984):

$$S_{xx,r} = 2E_r \cos^2(\theta) = \frac{\rho R c^2}{L} \cdot \cos^2(\theta) \quad (10)$$

The relation proposed by Svendsen (1984) serves as an upper limit approximation of the radiation stress contribution of the roller assuming the propagation of the roller is purely horizontal. Accordingly, the depth averaged momentum equation in the cross-shore direction is given by Svendsen (1984):

$$\frac{\partial S_{xx,w}}{\partial x} + \frac{\partial S_{xx,r}}{\partial x} = \rho g h \frac{\partial \bar{\eta}}{\partial x} = 0 \quad (11)$$

Where $S_{xx,w}$ and $S_{xx,r}$ denote the momentum flux for the wave and roller respectively. The relation suggests that a decrease in shoreward momentum flux results in a set-up of the water level.

2.3.3 Wave Breaking

In addition to the roller energy balance, the short-wave breaking formulation used in Xbeach is relevant to the study. In the instationary *Surfbeat* mode, the wave breaking formulation introduced by J. A. Roelvink (1993) is used:

$$\begin{aligned} D_b &= \frac{\alpha}{4} \rho g f H_m^2 \\ H_m^2 &= \gamma(d + \bar{\eta}) \end{aligned} \quad (12)$$

Where α is a calibration coefficient, f is the frequency, and H_m denotes the maximum wave height. In accordance with (Battjes & Janssen, 1978) the maximum wave height, H_m , is defined as a fraction, γ , of the water depth. The breaker index γ is a user defined input variable in Xbeach and is set to 0.5 by default. Increasing the breaker index means the maximum wave height can be a larger fraction of the water depth. Consequently, a larger breaker index allows more wave energy to propagate to shallower depths. Conversely, a smaller breaker index results in waves breaking further offshore and limits the wave energy that propagates to shallower water depths.

2.3.4 Sediment Transport

In XBeach sediment concentrations are modelled using a depth-averaged advection diffusion equation given by equation 13 (Galappatti, 1983).

$$\frac{\delta h C_{sed}}{\delta t} + \frac{\delta h C_u^E}{\delta x} + \frac{\delta h C_v^E}{\delta y} + \frac{\delta}{\delta x} \left[D_h h \frac{\delta C}{\delta x} \right] + \frac{\delta}{\delta y} \left[D_h h \frac{\delta C}{\delta y} \right] = \frac{h C_{eq} - h C}{T_s} \quad (13)$$

Where C represents the depth-averaged sediment concentration which varies on the wave-group time scale, D_h is the sediment diffusion coefficient, and T_s represents the sediment adaptation time. In this model, the entrainment and deposition of sediments is determined by the disparity between the actual sediment concentration in the water column C and the equilibrium sediment concentration C_{eq} represented by equation 14.

$$C_{eq} = \max \left(\min \left(C_{eq,b}, \frac{1}{2} C_{max} \right) + \min \left(C_{eq,s}, \frac{1}{2} C_{max} \right), 0 \right) \quad (14)$$

When the depth-averaged sediment concentration C is greater than the equilibrium sediment concentration C_{eq} sediments are deposited on the bed. Conversely, when C is smaller than C_{eq} then sediments are entrained in the water column. The transport formulation used in this study is derived by (Rijn, 2007); van Thiel de Vries (2009), known as the Van Thiel – Van Rijn formulation. The equilibrium sediment concentrations are computed according to the following equations:

$$C_{eq,b} = \frac{A_{sb}}{h} \left(\sqrt{v_{mg}^2 + 0.64u_{rms,2}^2} - U_{cr} \right)^{1.5} \quad (15)$$

$$C_{eq,s} = \frac{A_{ss}}{h} \left(\sqrt{v_{mg}^2 + 0.64u_{rms,2}^2} - U_{cr} \right)^{2.4} \quad (16)$$

3 Methodology

The thesis is split up into two main numerical modelling exercises with the ultimate goal of answering the previously stated research questions. First, the skill and ability of XBeach to model the generation and propagation of infragravity waves during a storm event is evaluated. Field measurements near Egmond aan Zee, The Netherlands obtained between October and November 1998, are used to compare the observed hydrodynamic changes in the surf zone with XBeach predictions. Second, the relative importance of free infragravity waves on dune erosion and surf zone hydrodynamics is investigated. Two synthetic 1-D planar beach profiles are constructed by extracting an existing dune profile characteristic of the Dutch coast and altering the bed slope of the shoreface. XBeach simulations are run for both profiles with a synthetic wave field imposed at the offshore boundary to determine if morphological predictions produced by XBeach are sensitive to the inclusion of incoming free infragravity waves at the offshore boundary.

3.1 Phase I: Coast3D Model-Data Comparison

In the following section the Coast 3D field experiment and model-data comparison procedure is outlined and explained. First, the conditions observed at the Dutch coast at Egmond aan Zee are outlined. Subsequently, the adopted methodology for comparing the results yielded from the Xbeach model and the Coast3D field measurement campaign is discussed.

3.1.1 Coast -3D Field Measurement Campaign

Data was collected near the town of Egmond aan Zee, The Netherlands from October to November 1998 known as the Coast-3D measurement campaign. The site is characterized by a sandy beach with two well developed-bars as shown in Figure 8. Offshore conditions such as significant zero-down crossing wave height, mean direction, and peak period have been measured at an offshore directional-wave buoy located at 16m depth approximately 5km offshore. Furthermore, an array of sensors located in the surf zone included bidirectional current meters and pressure sensors as illustrated in Figure 8. Data from the sensors was captured for approximately 34min per hour at a sampling rate of 2 or 4Hz. In addition, the alongshore water level gradient was measured by two tidal stations separated by 30km centred at the town of Egmond aan Zee. Bathymetric changes were measured every few days with an amphibious vehicle, and noted relatively insignificant alongshore variations of the beach until the formation of a cross-shore profile at approximately 500hrs after the

start of the measurement campaign (Ruessink, Miles, Feddersen, Guza, & Elgar, 2001; Ruessink, van Enkevort, Kingston, & Davidson, 2000). During the measurement campaign a wide range of sea states were observed. The significant wave heights ranged between 0.2 – 5.2m and the peak period ranged 2.1 – 11.1s with the mean wave direction ranging between $\pm 45^\circ$ (relative to the shore normal) (Rijnsdorp, Ruessink, & Zijlema, 2015).

3.1.2 Coast-3D Data Processing

The Coast-3D field measurement campaign is comprised of several series of sensors aligned along cross-shore transects, see Figure 8. Sensor series 1 is comprised of a transect of four collocated bidirectional current meter and pressure sensors. The sensors report the pressure head under a wave in meters. The pressure head time series, sampled at 2Hz, is linearly detrended and divided into 2048s segments with 50% overlap. Afterwards, the segments are tapered with a Hanning window and co-spectra are computed with 30 degrees of freedom based on ensemble average Fourier transforms (Rijnsdorp et al., 2015; Sheremet, Guza, Elgar, & Herbers, 2002); subsequently, the energy densities are integrated over the infragravity wave frequency band. The following frequency bands are used:

- $f_{ss} \geq 0.3 \text{ Hz}$
- $f_{IG} = 0.04 - 0.005 \text{ Hz}$

Next, the variance density of the surface elevation, or the zeroth order spectral moment for the desired frequency band denoted by m_0 , is then computed as the integral of the spectrum between the desired cut-off frequencies:

$$m_0 = \int_{f_1}^{f_2} E(f) df \quad (17)$$

Finally, the root mean square (rms) wave height, H_{rms} , is then computed as the following:

$$H_{rms} = \sqrt{8m_0} \quad (18)$$

The rms infragravity wave height is computed for hourly bursts of data at each sensor, thus producing one representative wave height for each hour.

3.1.3 Xbeach model at Egmond aan Zee

An Xbeach model for the coastline at Egmond aan Zee, where the Coast-3D field measurement campaign was conducted, is setup for the October 24, 1998 storm. The bathymetry prior to the storm is shown in Figure 7 along with the corresponding locations of sensor series 1 and 7 that will be used for the model-field data comparison. The user-defined settings for the model are summarized in Table 2. Apart from the listed user-defined parameters, the default XBeach parameters are used as the model has been optimized for the conditions observed along the Dutch coast (Geer, Bieman, Hoonhout, & Boers, 2015). The model is run for a simulation time of 72 hours, in order to capture the nearshore wave behaviour across the entire storm event.

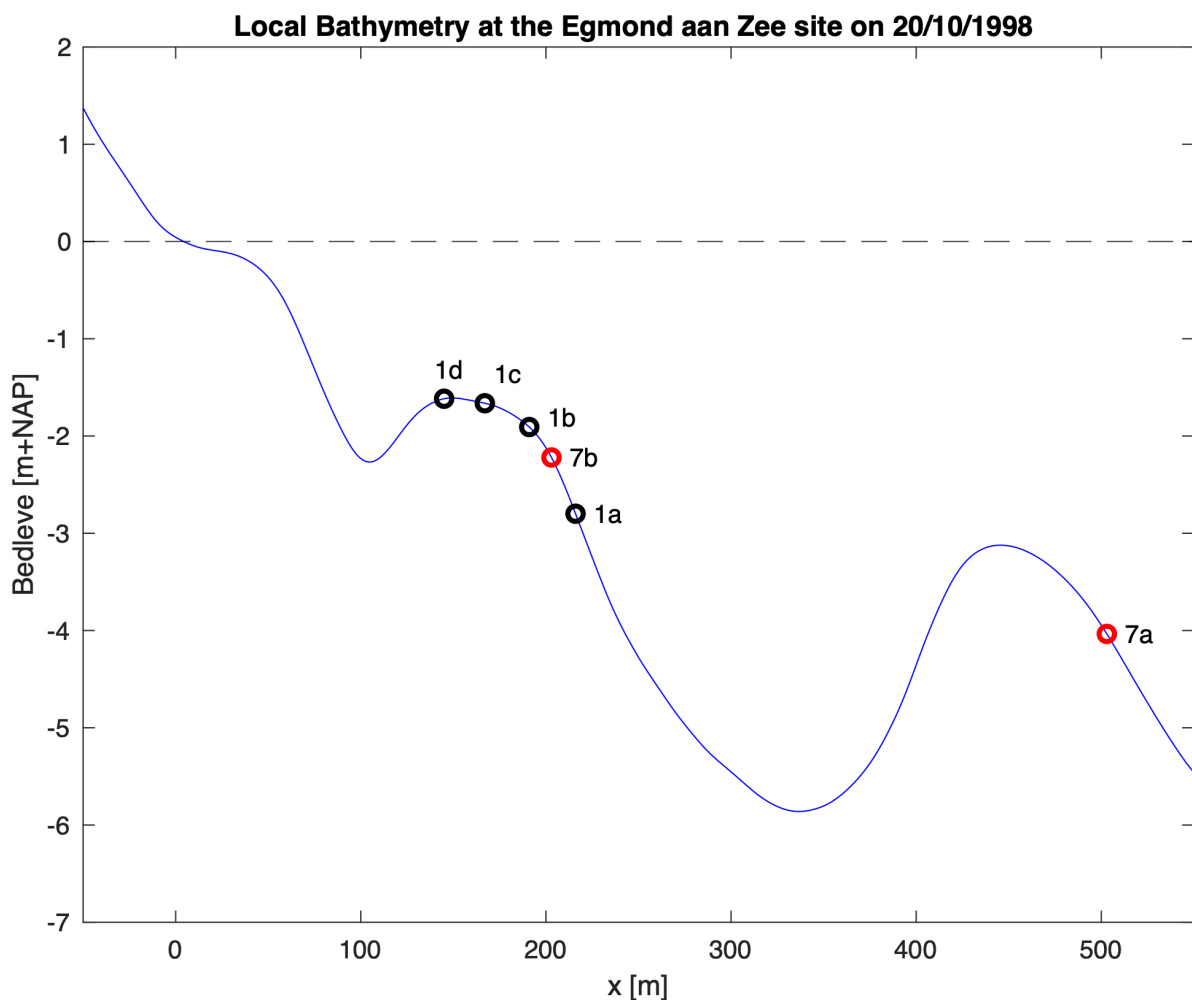


Figure 7: Local Bathymetry at the Coast-3D measurement site on 24/10/1998 indicating location of the pressure sensors.

The output results of the XBeach model are defined at locations coinciding with the locations of the sensors in the Coast-3D field measurements to facilitate the comparison of the numerical model

results and field results. The model produces a time-series of hydrodynamic parameters such as instantaneous water-surface elevation, instantaneous wave height, and water depth at each output location represented by the points in Figure 7.

Table 2: Phase I model settings.

Xbeach parameter	Description	Value	
nuhfac+	Roller induced turbulent horizontal viscosity	0.5	$\left[\frac{m^2}{s}\right]$
Beta+	Breaker slope coefficient for roller model	0.05 – 0.15	[-]
bedfriccoef	Bed friction (Chèzy)	53	$[m^{1/2}s^{-1}]$
Wavemodel	Wave model type	<i>Surfbeat</i> (1)	[-]
Gamma	Breaker parameter	0.4 – 0.55	[-]
σ_θ	Directional spreading	10 - 30	[°]

3.1.4 Boundary Conditions

Hourly significant wave height and peak period measurements were collected at an offshore directional wave buoy during the Coast-3D measurement campaign. The depth of the offshore buoy corresponds to the depth at which the model boundary is defined. A spectral wave boundary condition is employed to capture the incoming wave climate at the model boundary. The incoming waves at the model boundary are derived from a JONSWAP spectrum defined by the significant wave height, peak period, and directional spreading measured at the offshore buoy. XBeach then computes a random wave time-series from the defined spectrum and computes the underlying bound long wave.

3.1.5 Model-Data Comparison

A comparison between the XBeach model results and the Coast-3D field measurement campaign at Egmond aan Zee is used to verify that XBeach has skill at predicting near shore hydrodynamics of infragravity waves along the Dutch coast. A 1-D XBeach model is setup due to the alongshore uniformity of the coastline in the early stages of the considered storm. The bulk wave parameters produced by the XBeach models are resampled to hourly estimates to correspond with the hourly measurements produced by the Coast 3D data analysis. When Xbeach is run in *surfbeat* (instationary) mode the propagation of wave energy in the surf zone is computed by resolving the wave-action balance equation. Therefore, the instantaneous short-wave amplitude, and hence the wave height, at a particular temporal and spatial step is computed from the instantaneous wave energy as follows (Leo H. Holthuijsen, 2007):

$$E(x, t) = \frac{1}{8} \rho g H(x, t)^2 \rightarrow H(x, t) = \sqrt{\frac{8 \cdot E(x, t)}{\rho g}} \quad (19)$$

Where H is the instantaneous wave height, ρ is the water density, and g is the gravitational acceleration. Following the computation of the instantaneous wave height, the root mean square wave height is computed for each hourly burst as follows:

$$H_{rms,ss} = \sqrt{\frac{1}{N} \sum_n^N H_n^2} \quad (20)$$

The infragravity wave height is then computed by a spectral analysis of the surface elevation time series at each sensor. Analogous to the method adopted for processing the Coast-3D data, the surface elevation time series yielded at each output location is linearly detrended and divided into 2048s segments with 50% overlap. Subsequently, the co-spectra are computed and the energy densities are integrated over the frequency band ranging from $f_1 = 0.04 \text{ Hz}$ (25s) to $f_2 = 0.005 \text{ Hz}$ (200s). The result is a representative $H_{rms,IG}$ wave height for each hourly burst of the simulation run time.

The performance of the 1D Xbeach model is assessed based on the root mean squared error (RMSE) and skill factor of bulk wave parameters such as the root mean square sea-swell wave height and root mean square infragravity wave height. The RMSE is defined as the following:

$$RMSE = \sqrt{\langle (\alpha_P - \alpha_O)^2 \rangle} \quad (21)$$

Where $\langle \dots \rangle$ indicates time averaging over the measurement gauges and α refers to the bulk wave parameters denoted by P and O to indicate the predicted and observed values respectively. In addition, the skill factor is used as an indicator of the performance of XBeach to reproduce the conditions observed during the Coast3D measurement campaign. The skill factor is defined as the following (Gallagher, Elgar, & Guza, 1998):

$$Skill = 1 - \frac{\sqrt{\langle (\alpha_P - \alpha_O)^2 \rangle}}{\sqrt{\langle (\alpha_O)^2 \rangle}} \quad (22)$$

Where similarly $\langle \dots \rangle$ indicates averaging over the measurement gauges and α_p and α_o denote the predicted and observed bulk wave parameters respectively.

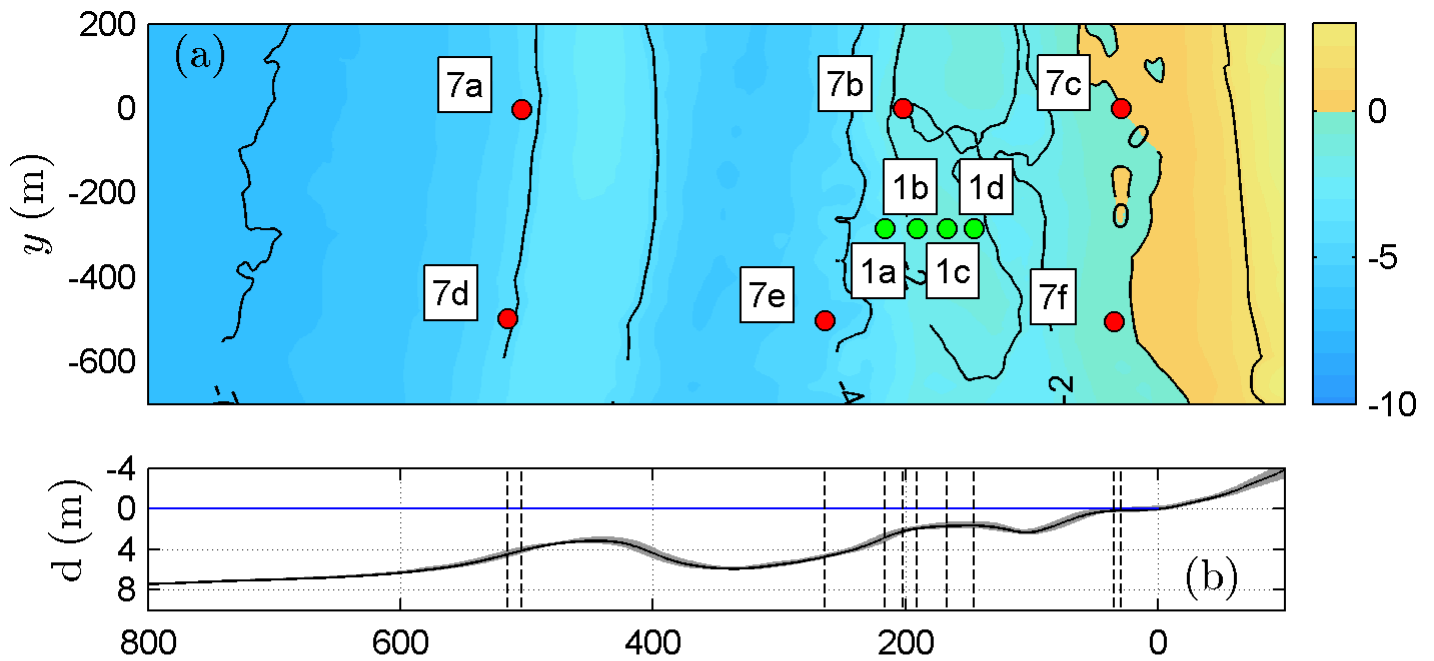


Figure 8: Plan view of bathymetry near Egmond aan Zee relative to mean sea level for (a) October 24, 1998 where red circles indicate pressure sensors, and green circles indicate collocated bidirectional current meters and pressure sensors; (b) The depth (alongshore mean, line; alongshore standard deviation, grey shading); Reproduced from code by Dirk Rijnsdorp.

3.2 Phase II: Impact of Free Long Waves on Dune-erosion

In order to assess the relative impact of incoming free infragravity waves on shoreline processes a second XBeach model is setup in *surfbeat* mode for two distinct beach profiles. In the following section the profiles, boundary conditions, and model parameters used for this phase of the study are explained.

3.2.1 Model Profiles

Two distinct profiles are distinguished in the study: a *steep* profile and a *mild* profile. Studies by J. A. Roelvink (1993); van Dongeren et al. (2007) have shown that the frequency dependent reflection of waves at the shoreline is related to the normalized bed slope, β , given by:

$$\beta_H = \frac{h_x}{\omega} \sqrt{\frac{g}{h'}} \quad (23)$$

Where:

h_x [-]	= Bed slope
ω [s ⁻¹]	= Radial frequency
g [ms ⁻²]	= Gravitational acceleration
h' [m]	= Representative depth

Battjes, Bakkenes, Janssen, and van Dongeren (2004) found that the normalized bed slope, β , governs the dissipation regime of infragravity waves at the shoreline. For large values of β ($\beta > 0.3$), a steep-slope regime is expected. A steep-slope regime entails that the amplitude growth in the shoaling zone is weak, and for steep bed slopes long waves nearly fully reflect at the shoreline (Battjes et al., 2004). Conversely on coasts with mild-slope regimes ($\beta < 0.06$), large amplitude growth in the shoaling zone and small reflections at the shoreline is expected. By considering several beach slopes, the effect of the bed slope on the propagation and transformation of infragravity waves in the surf zone can be distinguished. Consequently, the sensitivity if the dune response to the inclusion of free infragravity waves at the boundary is assessed for two different beach regimes.

The two profiles are assembled by combining a dune profile characteristic of the Dutch coast and a planar shoreface with the desired slope at mean sea level (MSL). The results is a representative

dune profile above MSL and a planar slope below MSL. The steep and mild profiles are shown in panels A and B of Figure 9 respectively.

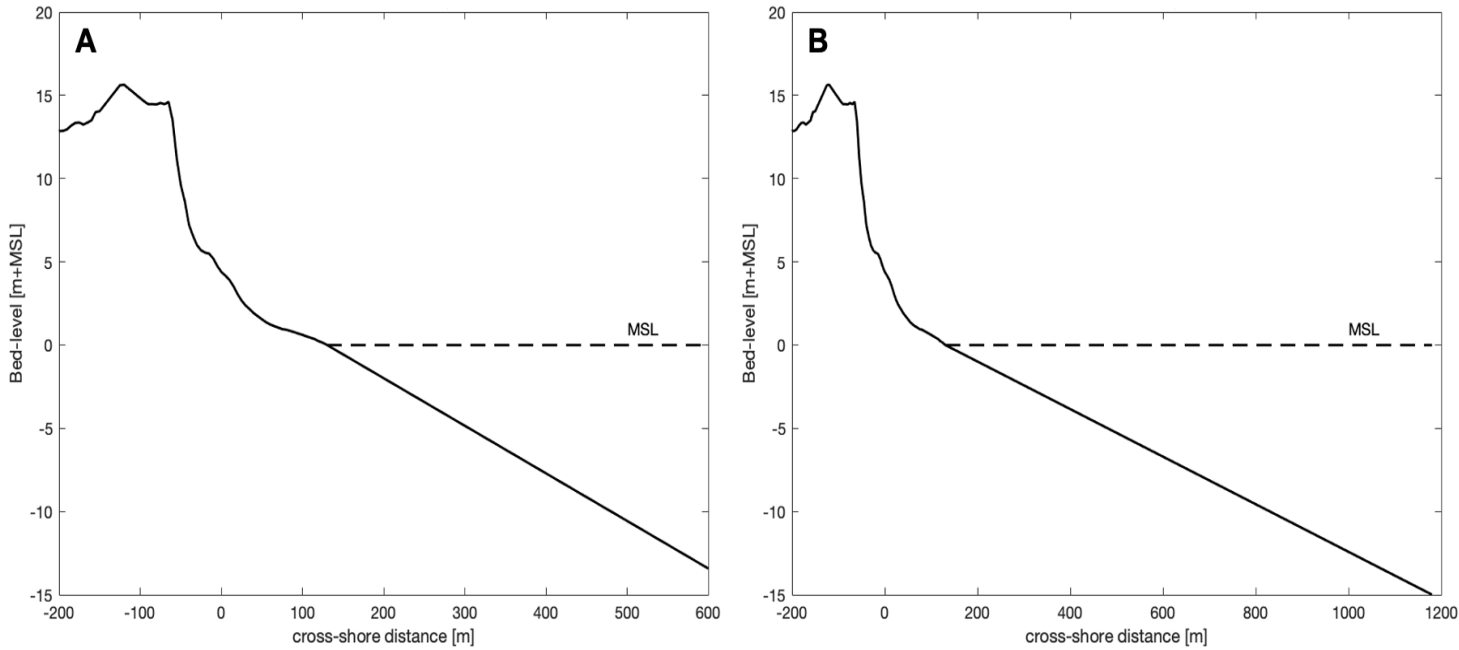


Figure 9: (A) Steep profile ($m=1:35$, $\beta\sim 0.4$); (B) Mild profile ($m=1:70$, $\beta\sim 0.2$)

3.2.2 Boundary conditions

The wave climate entering the model domain is described by a synthetic water surface elevation time series imposed at the offshore model boundary. The synthetic time-series is generated by applying a random phase model to a synthetic JONSWAP spectrum. The JONSWAP spectrum is a variance density spectrum developed by the *Joint North Sea Wave Project* (Klaus Hasselmann et al., 1973) and is used to describe the wave conditions observed in the North Sea. The spectral shape of the JONSWAP spectrum is an adaptation of the Pierson-Moskowitz spectrum to better describe the wave climate in the North Sea and is described by the following equation (K. Hasselmann, 1962; Leo H. Holthuijsen, 2007):

$$E(f) = \alpha g^2 (2\pi)^{-4} f^{-5} \exp\left[-\frac{5}{4}\left(\frac{f}{f_{peak}}\right)^{-4}\right] \gamma \exp\left[-\frac{1}{2}\left(\frac{f/f_{peak}-1}{\sigma}\right)^2\right] \quad (24)$$

Where γ is a peak-enhancement factor, σ is a peak-width parameter, and α is a scale parameter. In this study a peak enhancement factor of $\gamma = 3.3$ is used yielding the JONSWAP spectrum shape illustrated in Figure 10. The spectrum is then scaled as a function of the desired significant wave height by $\alpha = H_s^2/16$.

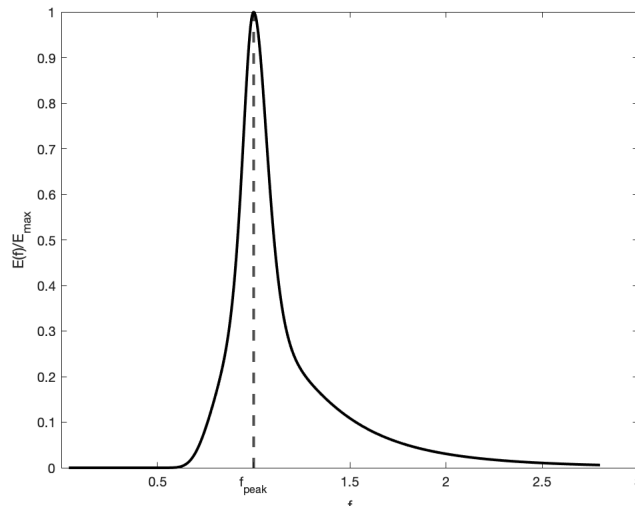


Figure 10: JONSWAP spectrum shape with $\gamma = 3.3$

Subsequently, the directional spreading of the waves is captured by the $\cos^m \theta$ model. (Willard J. Pierson, John, & John, 1952):

$$D(\theta) = A_1 \cos^m \theta \quad \text{for } |\theta| < 90^\circ$$

$$A_1 = \Gamma\left(\frac{1}{2}m + 1\right) / \Gamma\left(\frac{1}{2}m + \frac{1}{2}\right) \quad (25)$$

Where Γ denotes the gamma function and the exponent m controls the width of the distribution. for this study the exponent m is defined as $m \sim 2.5$ for a directional width of $\sigma_\theta = 30^\circ$. The resulting frequency directional spectrum is illustrated in Figure 11.

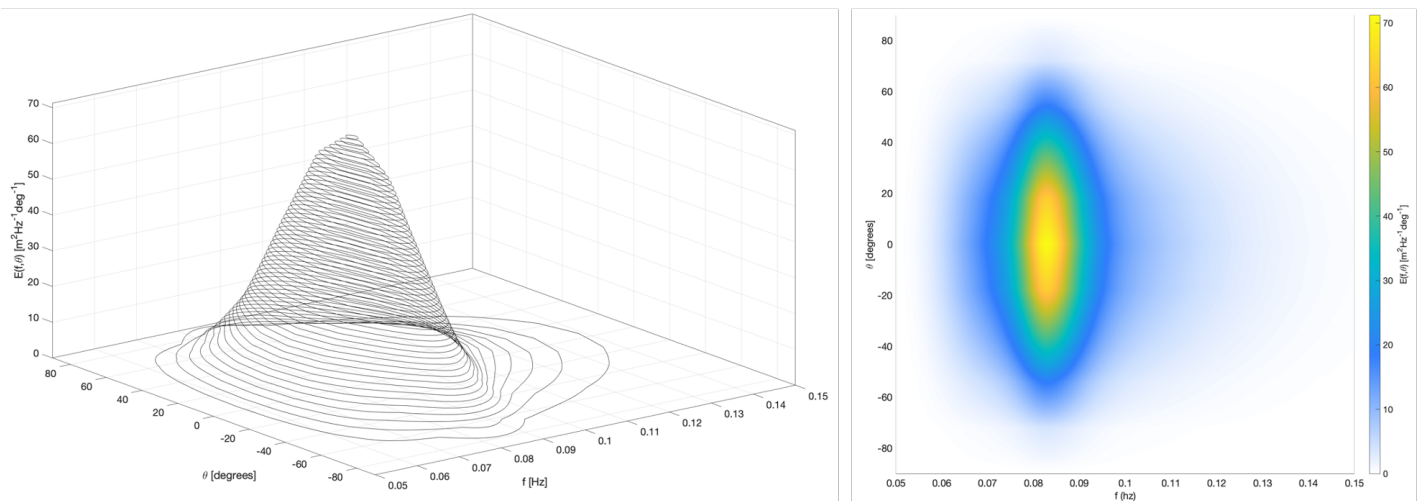


Figure 11: Directional energy distribution across the total frequency range.

Afterwards, the bound long wave energy is estimated using the non-linear coupling derived by K. Hasselmann (1963) and Herbers, Elgar, Guza, and O'Reilly (1995). The bound long wave variance

density is computed by the non-linear difference interaction between two short waves given by Herbers et al. (1995):

$$E_{bound}(f) = \int_{0.04}^{f_{max}} \int_0^{2\pi} \int_0^{2\pi} C^2(f - f', f', \Delta\theta) E(f - f', \theta_1) E(f', \theta_2) d\theta_1 d\theta_2 df \quad (26)$$

Where $E(f, \theta)$ denotes the frequency-directional variance density spectrum of the sea-swell waves. The corresponding interaction coefficient, C , is given by:

$$C(s_1 f_1, s_2 f_2, \Delta\theta) = \frac{g k_1 k_2 \cos(\Delta\theta)}{2\sigma_1 \sigma_2} + \frac{g(\sigma_1 + \sigma_2) \cosh(k_1 h) \cosh(k_2 h)}{[g k_3 \tanh(k_3 h) - (\sigma_1 + \sigma_2)^2] \sigma_1 \sigma_2 \cosh(k_3 h)} \quad (27)$$

$$\times \left((\sigma_1 + \sigma_2) \left[\frac{(\sigma_1 \sigma_2)^2}{g^2} - k_1 k_2 \cos(\Delta\theta) \right] - \frac{1}{2} \left[\frac{\sigma_1 k_2^2}{\cosh^2(k_2 h)} + \frac{\sigma_2 k_1^2}{\cosh^2(k_1 h)} \right] \right)$$

Where the radial frequencies are given by $\sigma_i = 2\pi s_i f_i$ and the wave numbers k_1 and k_2 are obtained from the linear dispersion relation. The difference wave number k_3 is obtained from the following:

$$k_3 = \sqrt{k_1^2 + k_2^2 + k_1 k_2 \cos(\Delta\theta)} \quad (28)$$

Therefore, the bound infragravity wave is imposed where the phase is derived from the difference of the two short wave components shifted by 180° . The free infragravity wave variance density is subsequently derived as a multiple of the bound long wave variance density as follows:

$$E_{free}(f) = IG_{free} \times E_{bound}(f) \quad (29)$$

Conveniently, the multiplier IG_{free} is used to name the different boundary conditions summarized in Table 3. The free infragravity wave amplitudes are then computed by linear wave theory:

$$a(f) = \sqrt{2 \cdot E_{free}(f) \cdot df} \quad (30)$$

The water surface elevation is then calculated by assigning random phases to the previously computed wave amplitudes:

$$\eta = a \cdot \cos(2\pi t + \phi_f) \quad (31)$$

Where ϕ_f represents the random phases assigned to the free infragravity waves independent of the short wave phases. The three boundary conditions used in the study are presented in Figure 12 where panel A represents the boundary condition time series excluding free infragravity waves and panels B and C represent the time series for the $IG_{\text{free}} = 1$ and $IG_{\text{free}} = 2$ conditions.

Table 3: Boundary condition summary.

Name	Significant wave height [m]	Peak period [s]	IG_{free}
$IG_{\text{free}} = 0$	9	12	0
$IG_{\text{free}} = 1$	9	12	1
$IG_{\text{free}} = 2$	9	12	2

3.2.3 Correlation coefficient

The correlation between the long wave velocity component and the short-wave orbital velocity component provides an indication of the transport potential by the interaction of long and short waves. The *Pearson Correlation Coefficient* is computed by the following:

$$r^2(X, Y) = \left(\frac{1}{N-1} \sum_{i=1}^N \left(\frac{X_i - \mu_x}{\sigma_X} \right) \left(\frac{Y_i - \mu_Y}{\sigma_Y} \right) \right)^2 \quad (32)$$

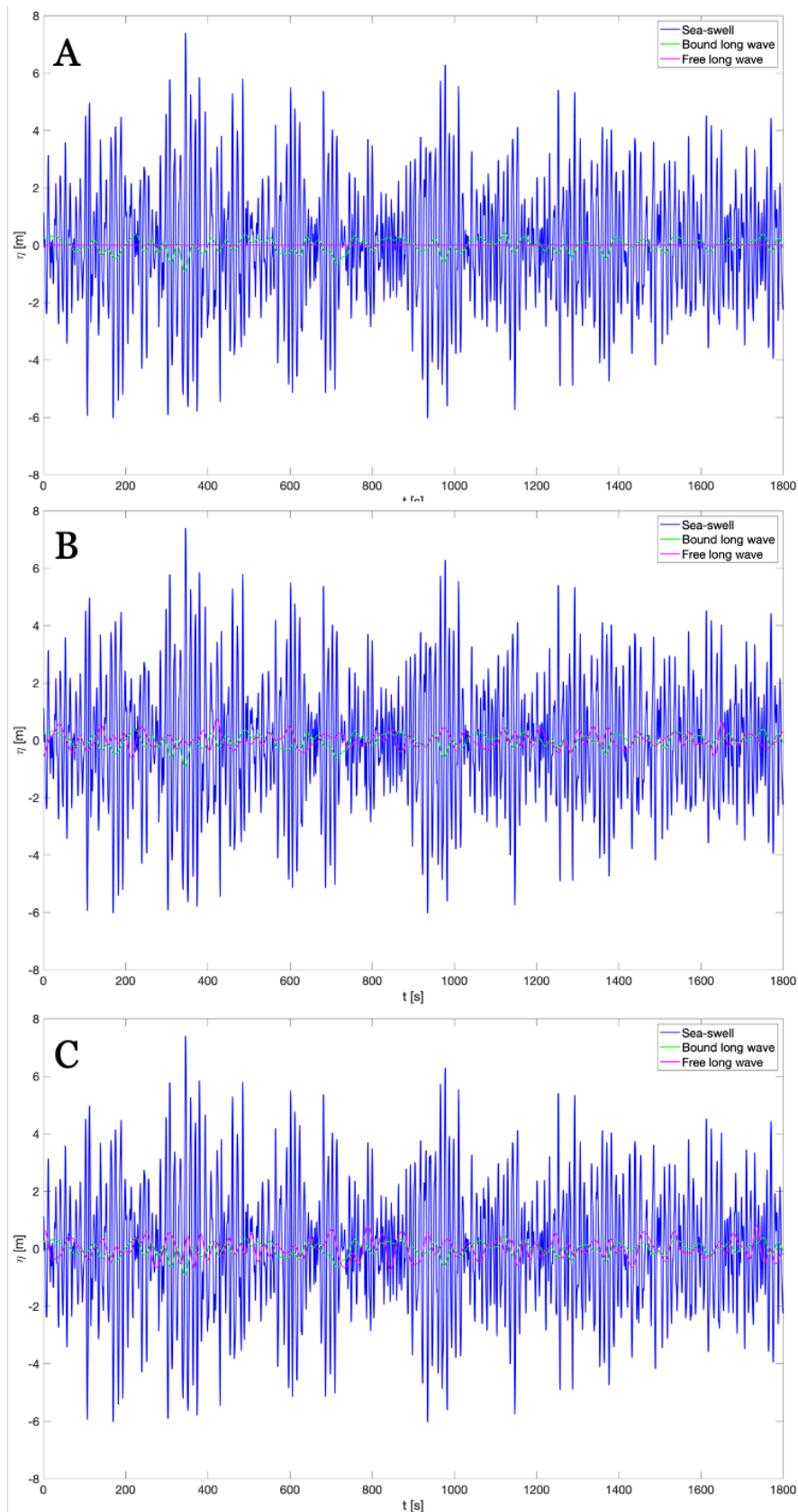


Figure 12: 30 minute sample of the generated offshore boundary condition for (A) $IG_{free} = 0$; (B) $IG_{free} = 1$; (C) $IG_{free} = 2$; Where blue represents the short waves, green represents the bound long waves, and magenta represents the free long waves.

3.2.4 Model Setup

Xbeach has many input parameters used to define the hydrodynamic and morphodynamic response of a coastline to wave attack. A number of semi-empirical formulations are used to predict complex processes such as sediment transport and dune behaviour under wave attack. Therefore, in this study the models are simulated with the *Wattelijk Toets Instrumentarium* (WTI) calibration parameters used in studying coastal protection and sand dune behaviour along the Dutch coastline in order for the results to be comparable to other relevant studies (Do, Shin, Cox, & Yoo, 2018; D. Roelvink et al., 2009; Van Geer, Den Bieman, Hoonhout, & Boers, 2015). The WTI parameters used in the models are summarized in Table 4.

Table 4: WTI Xbeach settings (Van Geer et al., 2015)

Xbeach parameter	Description	WTI settings
f_w	Short wave friction coefficient	0.000
c_f	Dimensionless friction coefficient	0.001
Gammamax	Maximum wave height to water depth	2.364
Gamma	Breaker parameter for Roelvink model	0.541
beta	Breaker slope coefficient in roller model	0.138
wetslp	Critical avalanching slope underwater	0.260
alpha	Wave dissipation coefficient	1.262
facSk	Skewness factor	0.375
facAs	Asymmetry factor	0.123

For each profile, the wave runup and dune erosion is estimated for stationary extreme storm conditions for a duration of 5 hours. Experiments have shown that the dune response after 5 hours of stationary extreme storm conditions are representative of the behavior when observing a time series of varying storm conditions (Vellinga, 1982). The representative extreme storm conditions used in the simulations are summarized in Table 5.

Table 5: Representative extreme storm conditions (Heijer, 2012)

Xbeach parameter	Description	Value
Z_{s0}	Surge level	5.0 [m+MSL]
H_s	Significant wave height model	9.0 [m]
T_p	Peak period	12 [s]
D_{50}	Median grain size	225 [μm]

A summary of all the simulations carried out in this phase of the study are summarized in Table 6.

Table 6: Model simulation summary

Profile	Wave boundary condition
Steep	$IG_{free} = 0$
	$IG_{free} = 1$
	$IG_{free} = 2$
Mild	$IG_{free} = 0$
	$IG_{free} = 1$
	$IG_{free} = 2$

3.2.5 Wave runup and Dune Erosion Estimation

Xbeach features a runup gauge output type which tracks the temporal variation of the waterline at the shoreline. The resulting output file is a time series of the water level elevation at the runup tongue. First, the runup level time series is detrended by subtracting the surge-level from the time-series signal. Second, a zero-down crossing analysis is carried out to distinguish between individual runup events. Subsequently the individual runup events are ranked by their respective crest heights and the 2% exceedance runup level is computed as the value corresponding to the 98th percentile. Additionally, the maximum runup level for each simulation is considered for the analysis. The Dune-erosion volumes per unit width of shoreline for the various simulations are estimated by computing the difference between the final and initial bed levels above the dune foot level, defined as (+3.00m).

4 Results

In the following section the results of the various XBeach modelling exercises are discussed. First, the results of the XBeach model validation exercise are discussed. Second, the impact of the infragravity wave boundary conditions of the three model profiles is elucidated.

4.1 Phase I: Coast-3D Model-Data Comparison

The October 28, 1998 storm was simulated in XBeach with several combinations of input variables in order to find the hydrodynamic parameters that produce the most robust bulk-wave predictions. The list of the different simulations and their respective prediction errors are listed in Table 7. In addition, the skill factor of the bulk-wave parameter predictions for infragravity and sea-swell waves are presented in Table 8. The results presented in Table 7 show a 0.13m and 0.05m improvement is realized for the infragravity wave and short wave predictions respectively when the roller breaker slope coefficient β is set to 0.15, and the short wave breaker parameter γ is set to 0.40 (see column 4 of Table 7). Likewise, the results presented in Table 8 show the predictive skill increases from 0.08 to 0.69 and 0.66 to 0.73 for the infragravity waves and short-wave predictions respectively for the same conditions. The predicted rms wave heights are of a similar order of magnitude as the observed values during this storm event. Likewise, significant improvements were realized when the directional spread of the waves was increased to 30° to better represent conditions observed in The North Sea (Leo H. Holthuijsen, 2007). Although the simulations were run for a 1-D bathymetry, XBeach retains directional spreading in *Surfbeat* mode. Initially the simulations were run with the default directional spreading of 10° yielding the results shown in columns 1 through 3 in Table 7. Column 4 in Table 7 represents the results for the simulation with the increased directional spreading exhibiting considerable improvements. The influence of the directional spreading is also exhibited in improvements in the predictive skill factor for infragravity waves as summarized in column 4 of Table 8.

For purposes of simplicity, all the figures and predictions presented in the following section correspond to the results of the simulation with a roller breaker slope coefficient of $\beta=0.15$, and breaker coefficient of $\gamma=0.40$, and directional width of $\sigma_\theta=30^\circ$. It is imperative to note that the model tended to over-estimate the infragravity wave heights. Also, it is noteworthy to highlight the fact that the predictions at the deepest sensor (7a) had the weakest predictive potential of all the observed

sensors. This trend was common across all the simulations with different input variables and was persistent throughout the entire simulated storm.

Table 7: Root-Mean-Square Error (RMSE) of the H_{rms} predictions for infragravity and sea-swell waves

Sensor	[1] $\beta=0.10; \gamma=0.55;$ $\sigma_{\theta}=10^{\circ}$ (Default) [m]		[2] $\beta=0.15; \gamma=0.40;$ $\sigma_{\theta}=10^{\circ}$ [m]		[3] $\beta=0.15; \gamma=0.40;$ $\sigma_{\theta}=10^{\circ}$ (morphology off) [m]		[4] $\beta=0.15; \gamma=0.40;$ $\sigma_{\theta}=30^{\circ}$ (morphology off) [m]	
	Hrms _{IG}	Hrms _{SS}	Hrms _{IG}	Hrms _{SS}	Hrms _{IG}	Hrms _{SS}	Hrms _{IG}	Hrms _{SS}
1a	0.19	0.20	0.09	0.22	0.09	0.22	0.06	0.22
1b	0.17	0.21	0.08	0.27	0.07	0.27	0.05	0.28
1c	0.18	0.30	0.08	0.21	0.07	0.21	0.06	0.22
1d	0.20	0.29	0.09	0.20	0.08	0.20	0.07	0.20
7a	0.21	0.59	0.09	0.49	0.09	0.50	0.06	0.50
7b	0.19	0.35	0.09	0.21	0.09	0.21	0.06	0.21
Average	0.19	0.32	0.09	0.27	0.08	0.27	0.06	0.27

Table 8: Skill¹ factor of the H_{rms} predictions for infragravity and sea-swell waves

Sensor	[1] $\beta=0.10; \gamma=0.55;$ $\sigma_{\theta}=10^{\circ}$ (Default)		[2] $\beta=0.15; \gamma=0.40;$ $\sigma_{\theta}=10^{\circ}$		[3] $\beta=0.15; \gamma=0.40;$ $\sigma_{\theta}=10^{\circ}$ (morphology off)		[4] $\beta=0.15; \gamma=0.40;$ $\sigma_{\theta}=30^{\circ}$ (morphology off)	
	Hrms _{IG}	Hrms _{SS}	Hrms _{IG}	Hrms _{SS}	Hrms _{IG}	Hrms _{SS}	Hrms _{IG}	Hrms _{SS}
1a	0.05	0.82	0.57	0.57	0.54	0.81	0.68	0.81
1b	0.23	0.80	0.67	0.67	0.66	0.75	0.75	0.74
1c	0.13	0.61	0.65	0.65	0.62	0.73	0.71	0.72
1d	-0.03	0.58	0.58	0.58	0.52	0.71	0.61	0.71
7a	0.05	0.55	0.58	0.58	0.59	0.63	0.71	0.63
7b	0.04	0.61	0.56	0.56	0.55	0.77	0.68	0.77
Average	0.08	0.66	0.60	0.60	0.58	0.73	0.69	0.73

¹A skill factor of 1 signifies a perfect agreement between the predicted and observed values

4.1.1 Short Wave Pattern

A time series of the water surface elevation and instantaneous wave energy for sensors 7a and 7b are shown in Figure 13 and Figure 14 respectively. The storm begins to grow in intensity at around 18hrs and persists until approximately hour 60 of the simulation. From the figures it is discernible that there is variability in the instantaneous energy signal, and hence the instantaneous wave height signal, during peak storm intensity. This can be explained by the fact that waves are depth limited at the location of sensor 7a. Between hours 0 and 12 variability above and below the mean line is visible in Figure 13. However, after hour 12 of the simulation as the storm grows in intensity and the offshore wave heights grow, the only discernible variability is below the mean signal. This behaviour

suggests that at the early stages of the simulation unsaturated conditions are observed at the seaward face of the outer bar at sensor 7a. Nonetheless, as the storm grows the wave conditions at 7a become saturated, meaning the largest waves in the incoming wave groups are breaking but the smaller waves in the signal are passing unbroken. Henceforth, the wave height at sensor 7a is capped by the local water depth indicating a saturated surf zone. This observation is further supported by the instantaneous wave energy time series for sensor 7b shown in Figure 14. Sensor 7b is located at a shallower depth and therefore the variability in the signal is smaller. The reduction in the observed variability can be explained by the fact that one can expect smaller waves to reach the shallower depth at sensor 7b and hence less waves are subject to depth induced breaking.

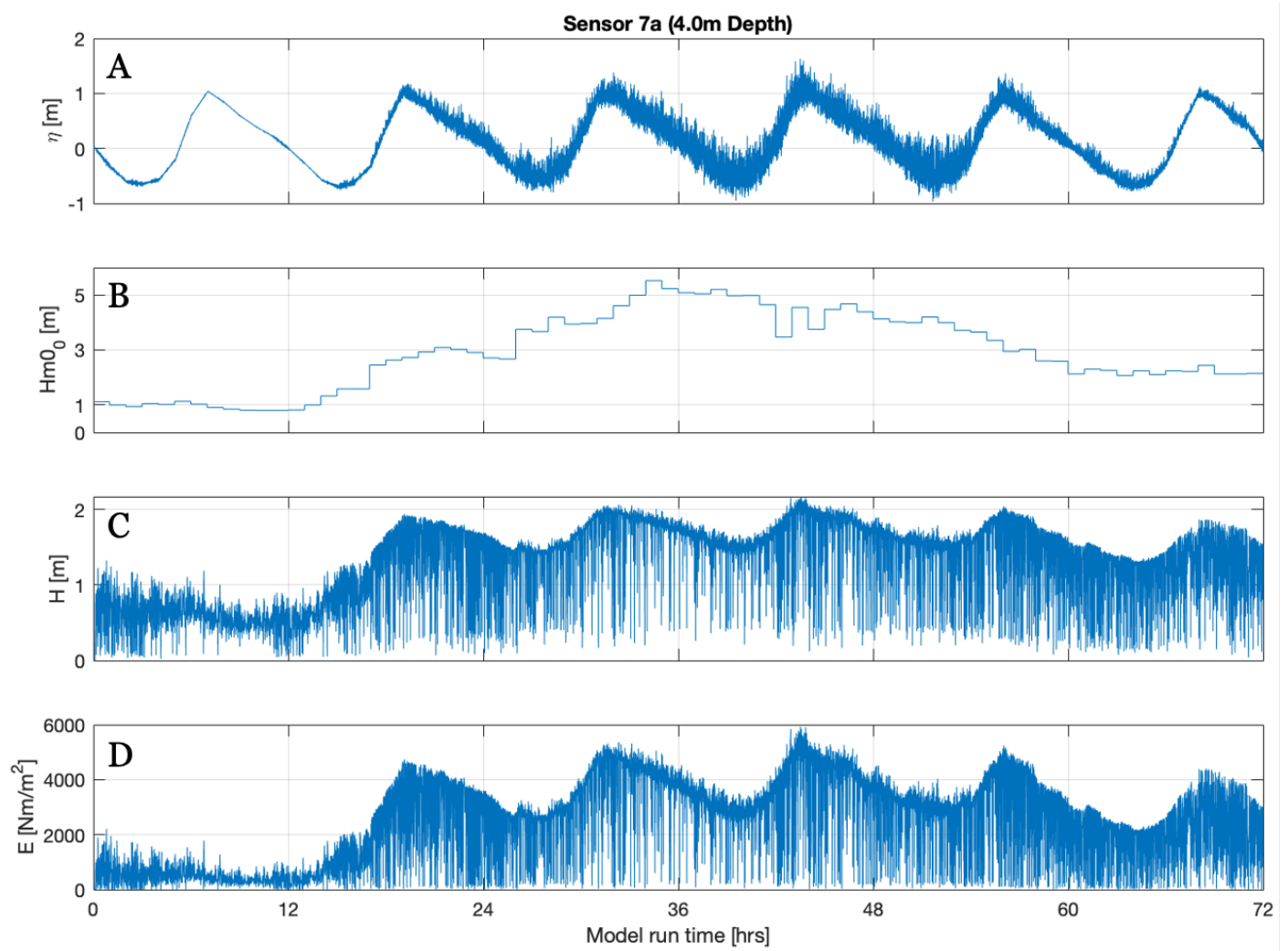


Figure 13: (A) Low frequency water surface elevation; (B) Offshore wave height; (C) instantaneous short wave height; and (D) instantaneous wave energy time series for sensor 7a located on the seaward edge of the outer bar.

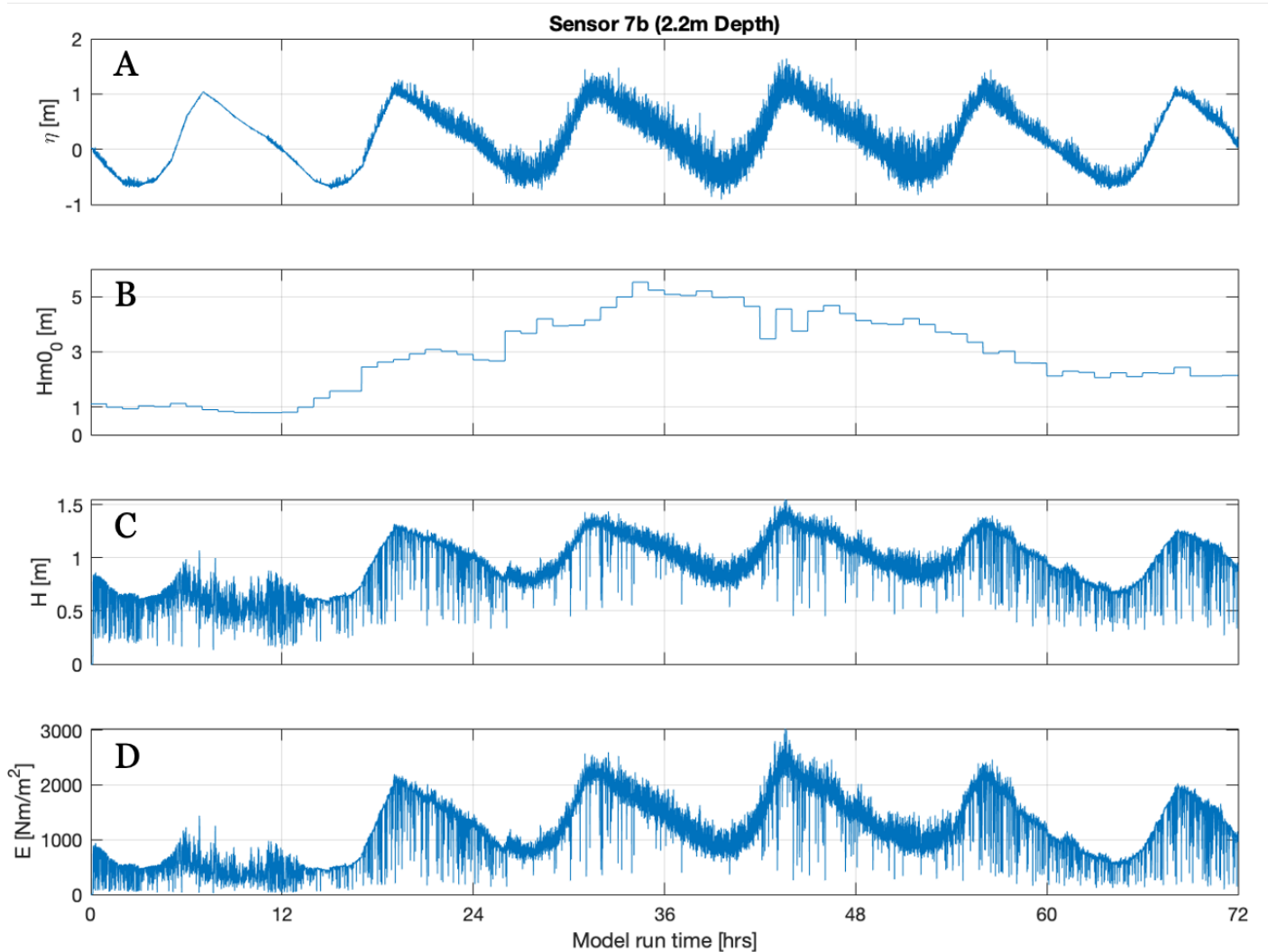


Figure 14: (A) Low frequency water surface elevation; (B) Offshore wave height; (C) instantaneous short wave height; and (D) instantaneous wave energy time series for sensor 7a located on the seaward edge of the inner bar.

4.1.2 Long Wave Pattern

The comparison of the time series at sensors 7a and 7b indicate that significant changes in the incoming wave energy are observed in the surf zone. In order to get a more complete idea of the propagation and transformation in the surf zone, the predicted and observed long wave behaviour is compared. The temporal evolution of the predicted and observed bulk wave parameters for the infragravity waves and short waves are compared in Figure 15. Figure 15 shows that during the storm's peak intensity the model has the propensity to over predict the long waves but under predicted the incident sea-swell wave climate.

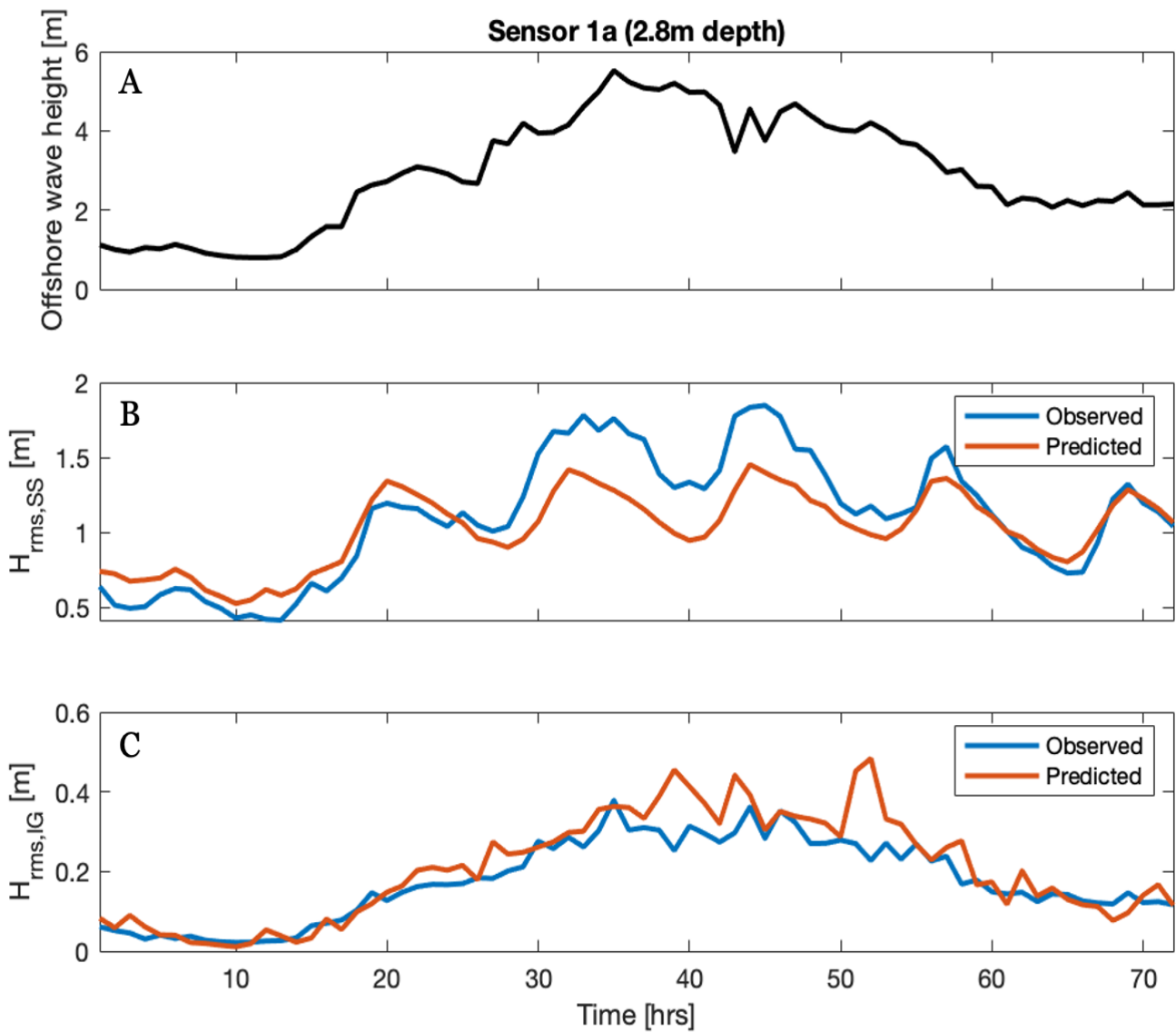


Figure 15: (A) Offshore wave height; (B) Predicted and observed short rms wave height; and (C) Predicted and observed infragravity rms wave heights at the seaward face of the inner bar at sensor 1a.

In addition, the results of the cross-shore evolution of the infragravity wave height after 24, 36, and 48 hours are presented in panels A, B, and C of Figure 16 respectively. Additionally, the cross-shore distribution of the predicted and observed rms wave height for the sea-swell waves is presented for hours 24, 36, and 48 in panels D, E, and F respectively. Panel A and D shows the cross-shore evolution of the infragravity wave height and short-wave height for the early development phase of the storm when the offshore wave height is 2.91m. Panel A shows that the model overestimated the infragravity wave height at all sensors along the transect. Furthermore, panel D shows that for the same offshore conditions the short-wave height is also over-predicted. However, this observed pattern shifts as the storm develops and the offshore wave height grows to 5.23m and 4.39m for hours 36 and 48 respectively. The cross-shore evolution of the short-wave height in panels E and F indicate that the short wave height is generally underestimated with the exception of the offshore

most sensor during hour 48. Nonetheless, the infragravity wave behaviour depicted in panels B and C is consistently overestimated throughout the duration of the storm.

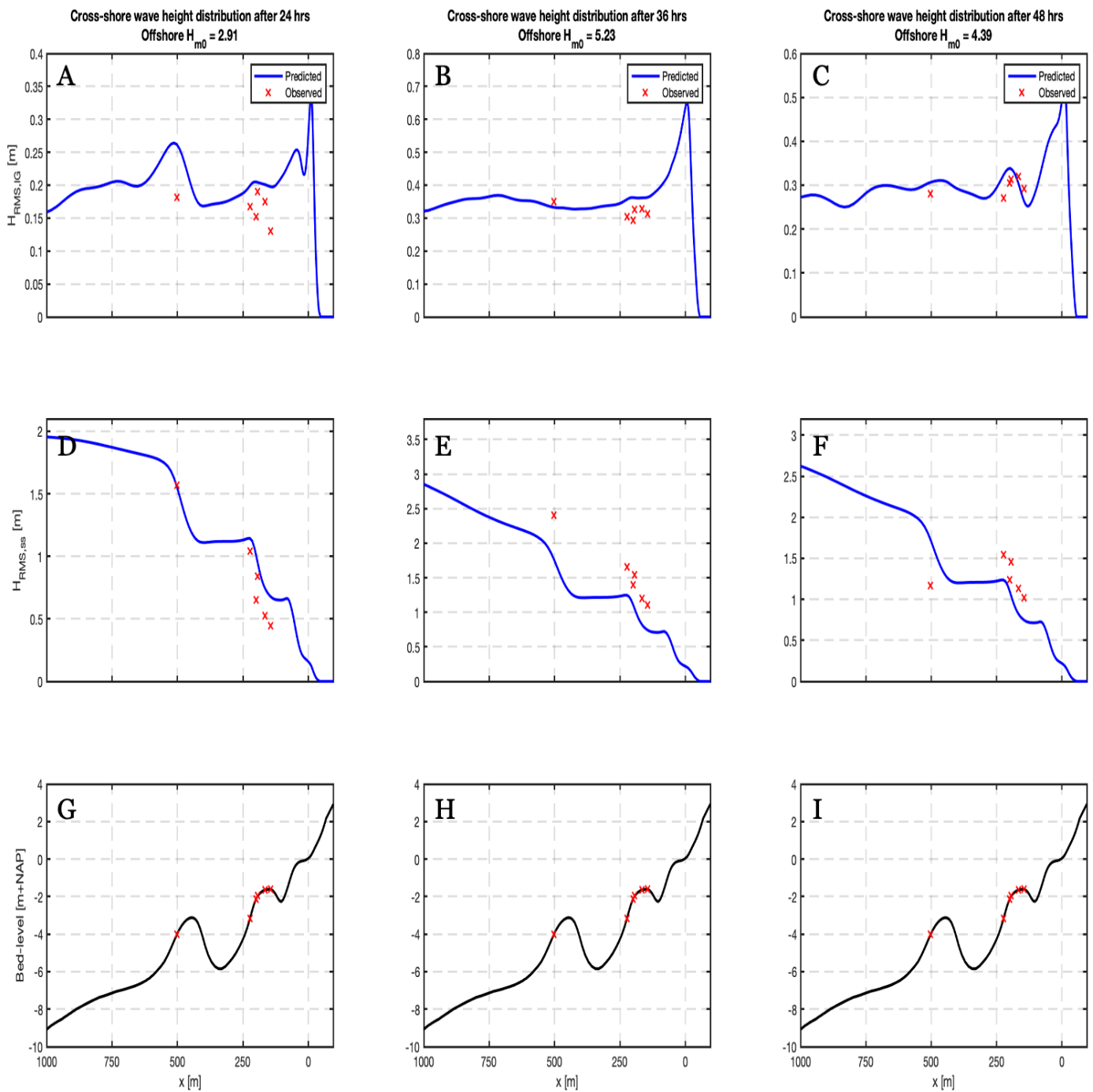


Figure 16: Cross-shore distribution of (A-C) infragravity rms wave height; (D-F) short rms wave height; (G-I) bathymetry and sensor locations.

The temporal evolution of the storm (see Figure 15) shows largest discrepancy between the predicted and observed infragravity wave heights occurs at hour 40 and hour 52 of the simulation. In Figure 17 and Figure 18 the cross-shore evolution of long and short waves is depicted for hours

40 and 52 of the simulation. For hour 40 of the simulation the infragravity wave height was over-predicted by an average of 13cm while the short-wave height was underpredicted by an average of 29cm. Similar cross-shore behaviour is observed for hour 52 of the simulation depicted in Figure 18. The average error in the infragravity and short-wave predictions is 21cm and 24cm respectively.

The predicted cross-shore evolution of the infragravity wave height shows that the model generally overestimates the long wave energy throughout the storm. This observation is further supported by the comparison of the predicted and observed infragravity wave heights in Figure 19. The solid black line represents perfect agreement between the observed and predicted values, and the dotted lines represent the 15% error bands. The comparison shows that the model generally overpredicts the most energetic waves in the surf zone. The comparison of the predicted and observed sea-swell wave heights in Figure 20 show relatively poorer predictions. The most energetic short waves tend to be under-estimated by the mode while the least energetic waves in the wave envelope were generally overestimated.

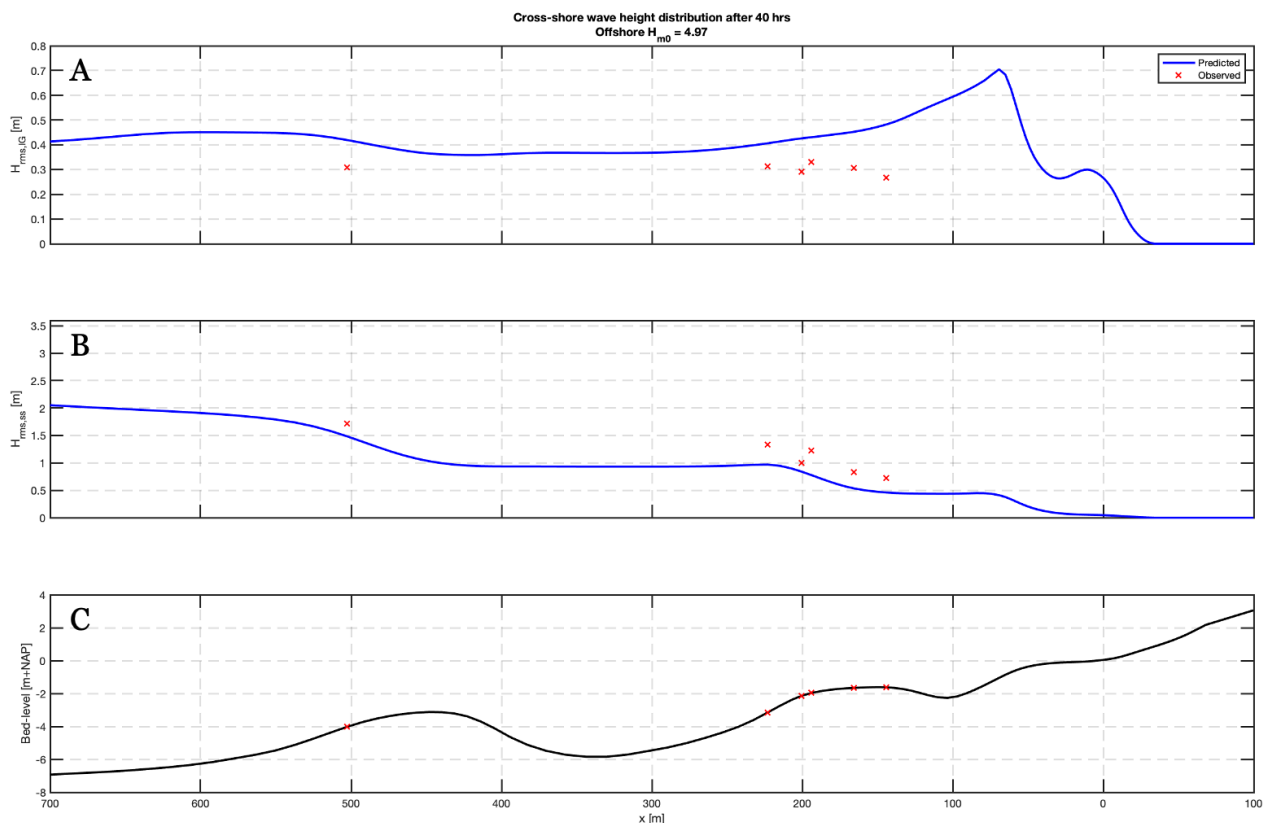


Figure 17: Cross-shore evolution of (A) infragravity rms wave height; (B) short rms wave height; (C) bathymetry and sensor locations for hour 40 of the simulation.

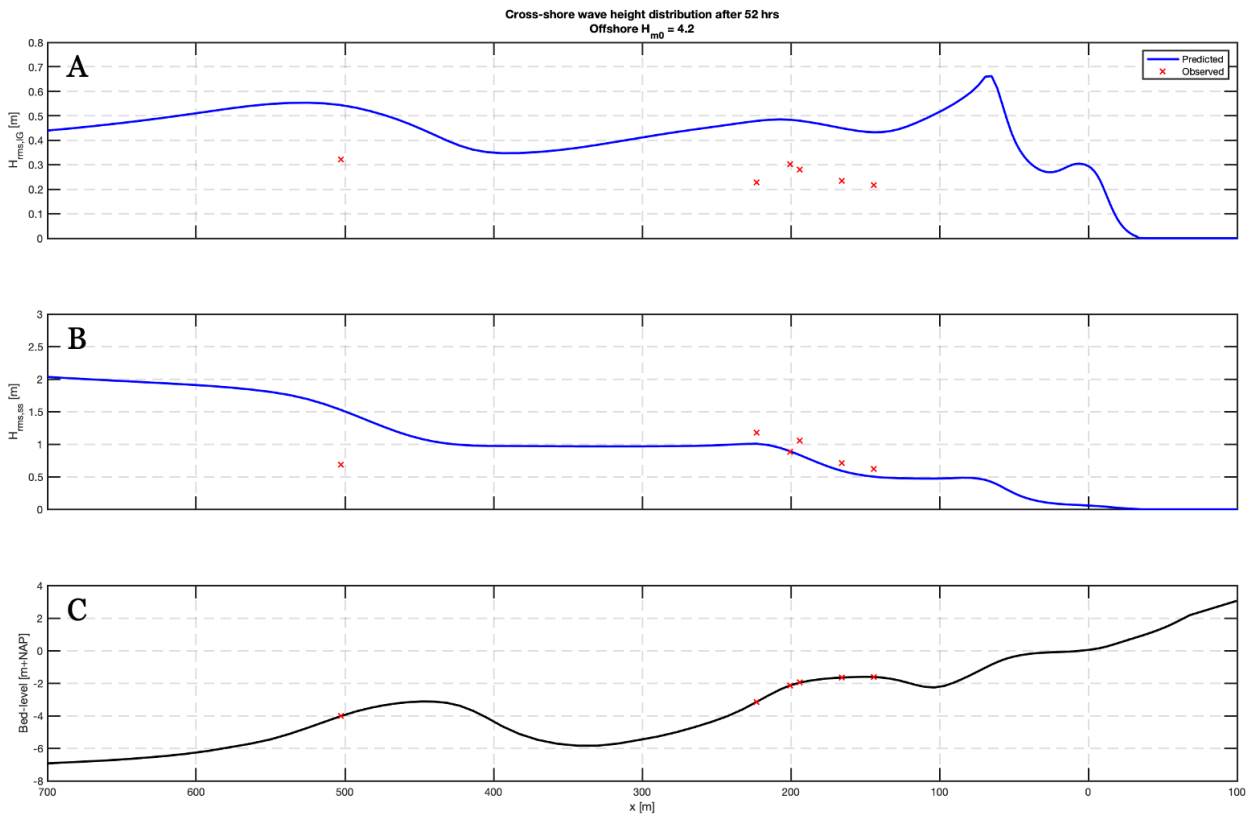


Figure 18: Cross-shore evolution of (A) infragravity rms wave height; (B) short rms wave height; (C) bathymetry and sensor locations for hour 52 of the simulation.

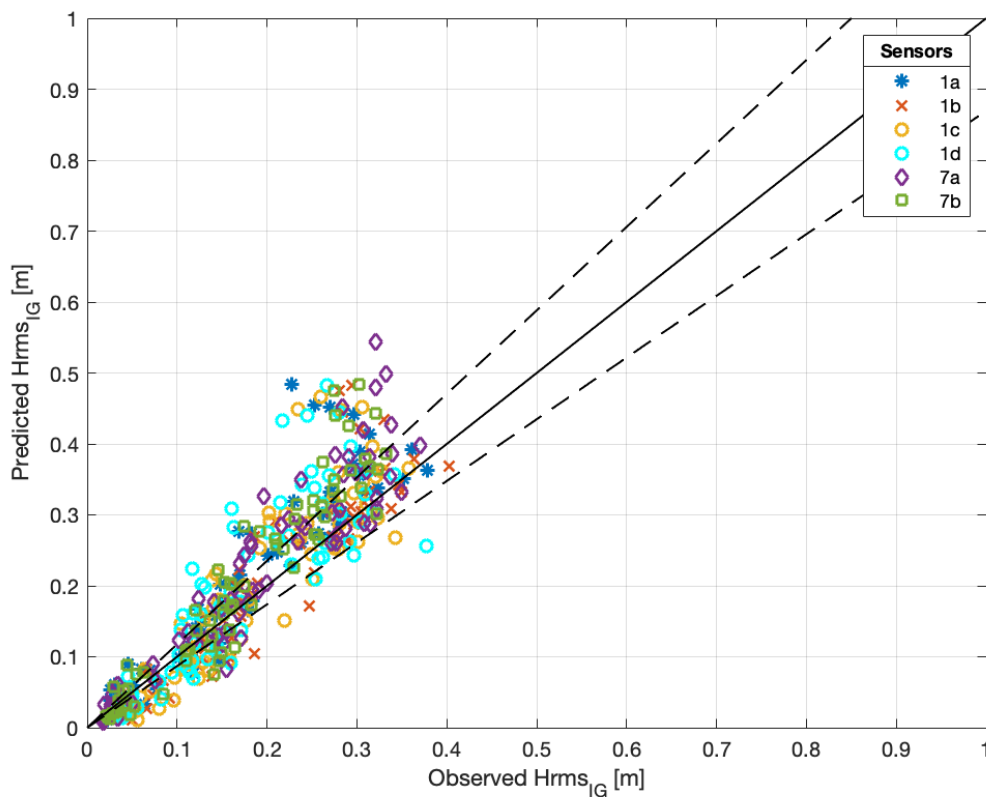


Figure 19: Predicted vs Observed infragravity wave height ($H_{rms,IG}$). Solid line indicates perfect agreements and dashed lines represent 15% error bands.

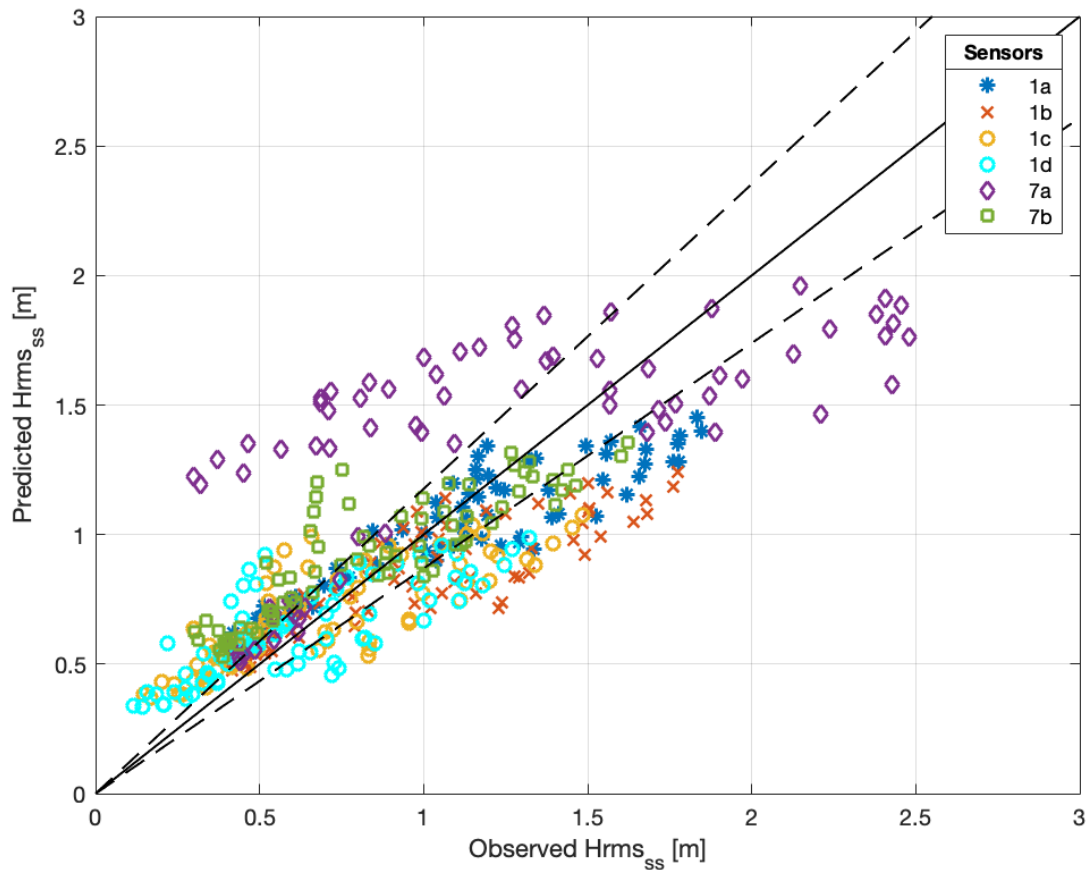


Figure 20: Predicted vs Observed sea-swell wave height ($H_{rms,ss}$). Solid line indicates perfect agreements and dashed lines represent 15% error bands.

4.2 Phase II: Impact of Free Long Waves on Dune Erosion

In the following section the results for the steep and mild profiles simulations for the second phase of the study are outlined.

4.3 Steep Profile

In Figure 21 the cross-shore evolution of several time-averaged hydrodynamic and morphodynamic parameters are presented. The rms infragravity wave height is portrayed in panel A. The comparison demonstrates that the maximum rms infragravity wave height increase from approximately 1.18m for the condition excluding free waves ($IG_{free} = 0$) to a maximum of 1.5m and 1.9m for the $IG_{free}=1$ and $IG_{free} = 2$ simulations respectively. In addition, the cross-shore evolution of the rms velocity of the long wave oscillatory component is presented in panel B. The comparison shows a similar trend with the time-averaged velocity increasing from a maximum of 1.47 ms^{-1} ($IG_{free} = 0$) to 1.64 ms^{-1} and 1.79 ms^{-1} for the $IG_{free} = 1$ and $IG_{free} = 2$ boundary conditions respectively. Furthermore, the cross-

shore evolution of the rms short wave height is plotted in panel C showing no discernible differences between the three simulations. In addition, the cumulative sediment transport rates per unit width are presented in panel D. The peak cumulative erosion at the upper dune face increases from 0.25m ($IG_{free} = 0$) to 0.50m ($IG_{free} = 1$) and 0.69m ($IG_{free} = 2$).

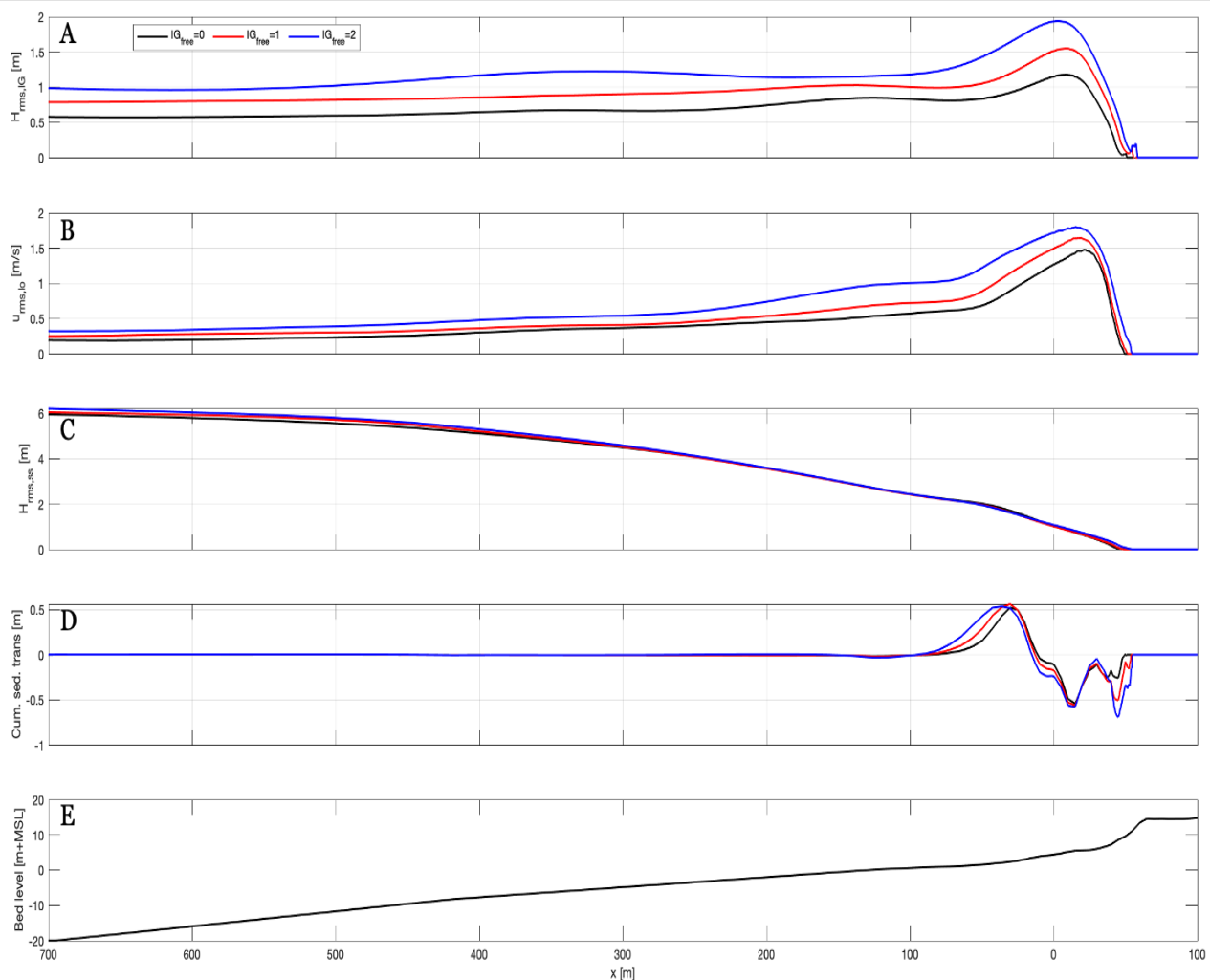


Figure 21: Steep slope cross shore distribution of: (A) rms infragravity wave height; (B) rms oscillatory long wave velocity component; (C) rms short wave height; (D) hourly mean of cumulative sediment transport where positive values correspond to accretion and negative values represent erosion; (E) bed level for $IG_{free} = 0$ (black line), $IG_{free} = 1$ (red line), and $IG_{free} = 2$ (blue line).

In order to gain a more comprehensive understanding of the sediment transport and dune erosion patterns observed in Figure 21 and Figure 28, the cross shore evolution of the time averaged correlation between the low frequency velocity component and short wave velocity variance is plotted in panel A of Figure 22. A correlation coefficient of -1 corresponds to the case when the long wave is 180° out of phase with incoming short-wave groups. Hence, a correlation of -1 is indicative

of the case when maximum short wave stirring coincides with the maximum offshore directed long wave velocity. On the other hand, a perfect correlation of 1 is indicative of the case when the short wave stirring coincides with the maximum onshore directed long wave velocity. The cross-shore evolution in panel A demonstrates that the case exclusive of free long waves (black line) has a correlation of -0.78 at the model border. Conversely the correlation for the $IG_{free} = 1$ and $IG_{free} = 2$ simulations at the boundary is -0.65 . Further necessary to explain the sediment transport patterns observed in the surf zone is the velocity moment of the interaction between the long wave velocity and the short-wave velocity variance as shown in panel B. At the shoreline the offshore directed velocity moment reaches a maximum at approximately $x=-35m$. The maximum velocity moment for the simulation excluding free long waves is $-0.32 \text{ m}^3\text{s}^{-3}$ ($IG_{free} = 0$), while the maximum long wave contribution to the velocity moment for the $IG_{free} = 1$ and $IG_{free} = 2$ simulations is $-0.37 \text{ m}^3\text{s}^{-3}$ and $-0.42 \text{ m}^3\text{s}^{-3}$ respectively. Moreover, closer to the shoreline at around $x=-35m$ the correlation between all three simulations is almost identical.

To further decompose the contributions of the wave velocities to the total sediment transport, the cross-shore evolution of the main constituents of the third odd velocity moment are presented in Figure 23. The plot compares the total odd velocity moment for the $IG_{free} = 0$ (black) and $IG_{free} = 2$ (blue), exhibiting a maximum offshore directed total velocity moment of $-1.00 \text{ m}^3\text{s}^{-3}$ and $-1.45 \text{ m}^3\text{s}^{-3}$ respectively. Furthermore, it is evident that the peak of the total third odd velocity moment for both simulations coincides with their respective peaks in the long wave contribution illustrated by the dotted lines in Figure 23.

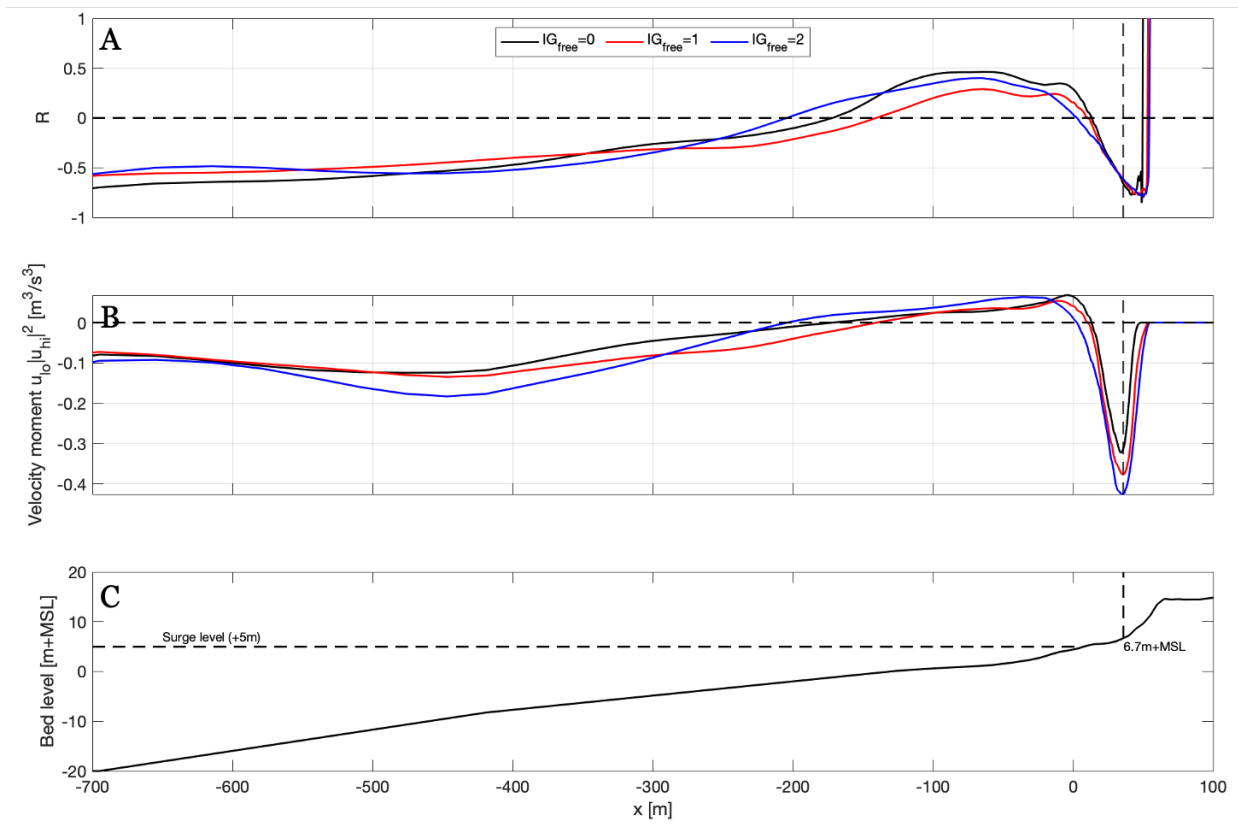


Figure 22: (A) Correlation between the u_{lo} and u_{hi}^2 ; (B) Velocity moment of the interaction between long wave velocity and short-wave velocity variance; (C) Step profile bed level. $IG_{free} = 0$ (black line), $IG_{free} = 1$ (red line), and $IG_{free} = 2$ (blue line).

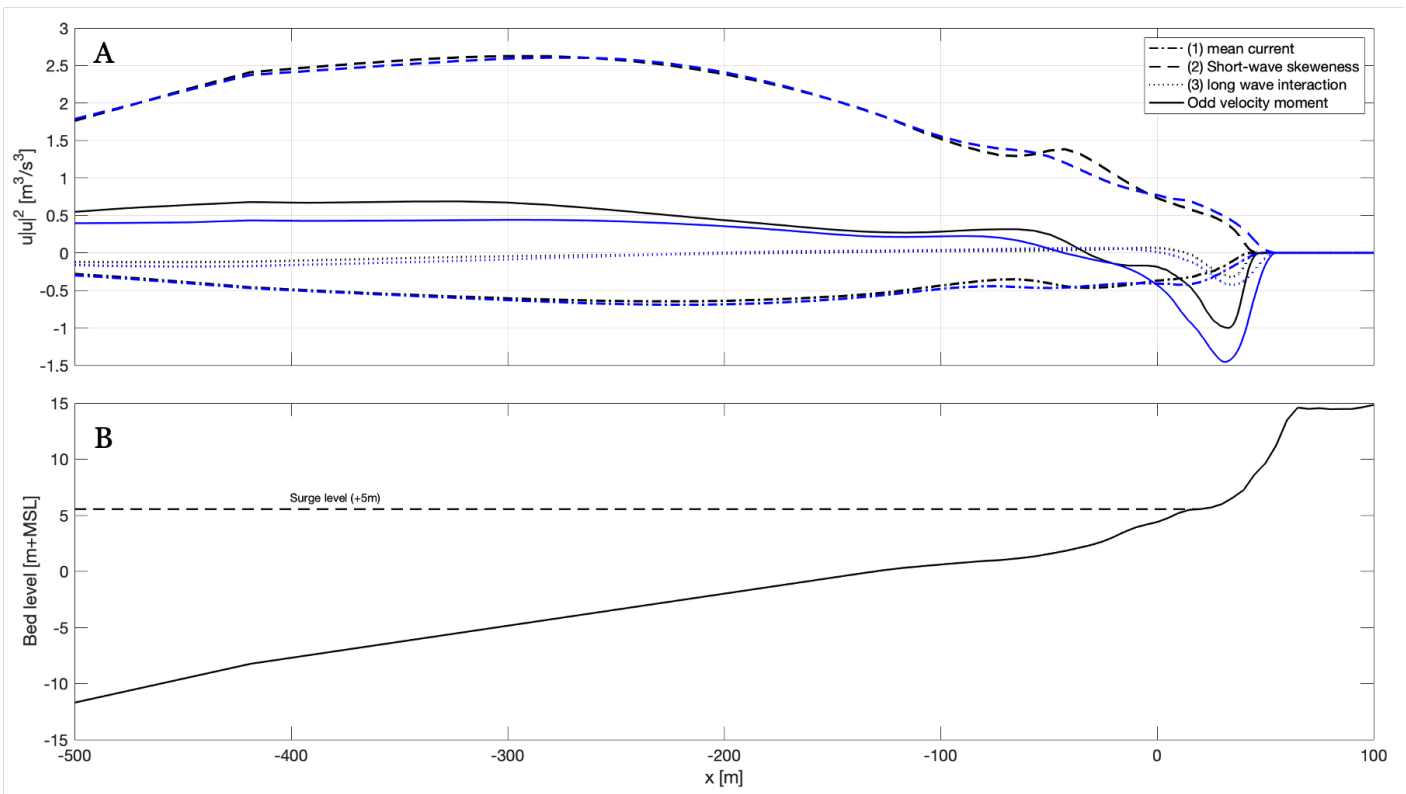


Figure 23: (A) Total odd velocity moments and their constituent components; black line represents $IG_{free} = 0$ and blue line represents $IG_{free} = 2$; (B) Step profile bed level.

4.4 Mild Profile

Similar to the previous section, the cross-shore evolution of the time averaged short and long wave heights, long wave velocities, and sediment transport rates are presented in Figure 24. The rms infragravity wave height portrayed in panel A of Figure 24 shows the wave heights reach a maximum level just shoreward of the point $x=0$. The peak wave height for the three simulations is 1.32m ($IG_{free} = 0$), 1.59m ($IG_{free} = 1$), and 2.02m ($IG_{free} = 2$). Further shoreward of the peak in wave infragravity wave heights a peak in the rms velocity corresponding to the long waves is observed in panel B. The peak rms long wave velocity is 1.51ms^{-1} ($IG_{free} = 0$), 1.60ms^{-1} ($IG_{free} = 1$), 1.74ms^{-1} ($IG_{free} = 2$). Analogous to the steep profile, the cross-shore evolution of the short-wave heights shows no distinguishable difference between the three boundary conditions. It is also worthy to note that a similar pattern is observed in the cross-shore evolution of the cumulative sediment transport rates. The shoreward most peak in erosion rates shows a pronounced increase in erosion with increasing long wave energy.

Furthermore, the cross-shore evolution of the correlation between the long wave velocity and short-wave velocity variance is plotted in panel A of Figure 25. The correlation coefficient at the boundary is -0.73 ($IG_{free} = 0$), -0.60 ($IG_{free} = 1$), -0.66 ($IG_{free} = 2$). The correlation exhibited in the mild profile is similar to the pattern observed in the steep profile where the correlation decreases with increasing long wave energy. The decrease in correlation is primarily due to the addition of long waves that are not phase locked to the propagating wave groups. In addition, the cross-shore evolution of the long wave contribution to the third odd velocity moment is illustrated in panel B of Figure 25. The plots exhibit a peak at the dune-face at approximately $x=25\text{m}$. The peak shows the maximum offshore directed contribution of the long wave velocity is located well above the dune-foot level. The plot also demonstrates that the long wave contribution to the velocity moment increase from $-0.33\text{ m}^3\text{s}^{-3}$ ($IG_{free} = 0$) to $-0.36\text{ m}^3\text{s}^{-3}$ ($IG_{free} = 1$) and $-0.40\text{ m}^3\text{s}^{-3}$ ($IG_{free} = 2$). A more comprehensive decomposition of the total third odd velocity moment for the $IG_{free} = 0$ and $IG_{free} = 2$ simulations are presented in panel A of Figure 29. The plot of the cross-shore evolution of the total velocity moment also exhibits a peak offshore directed velocity moment at approximately $x=25\text{m}$ coinciding with the peak in the long wave contribution discussed earlier.

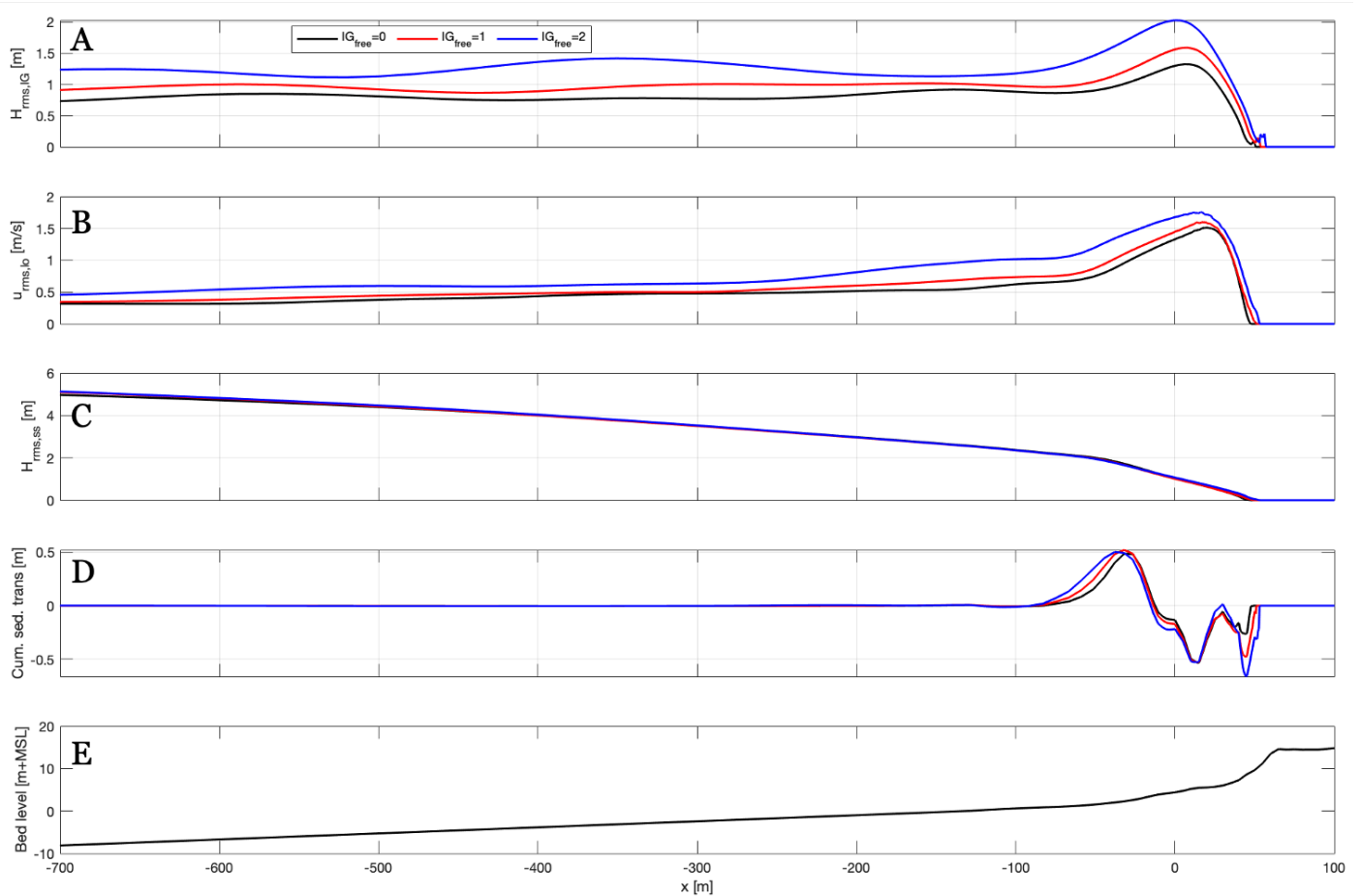


Figure 24: Mild slope cross shore evolution of: (A) rms infragravity wave height; (B) rms oscillatory long wave velocity component; (C) rms short wave height; (D) hourly mean of cumulative sediment transport where positive values correspond to accretion and negative values represent erosion; (E) bed level for $IG_{free} = 0$ (black line), $IG_{free} = 1$ (red line), and $IG_{free} = 2$ (blue line).

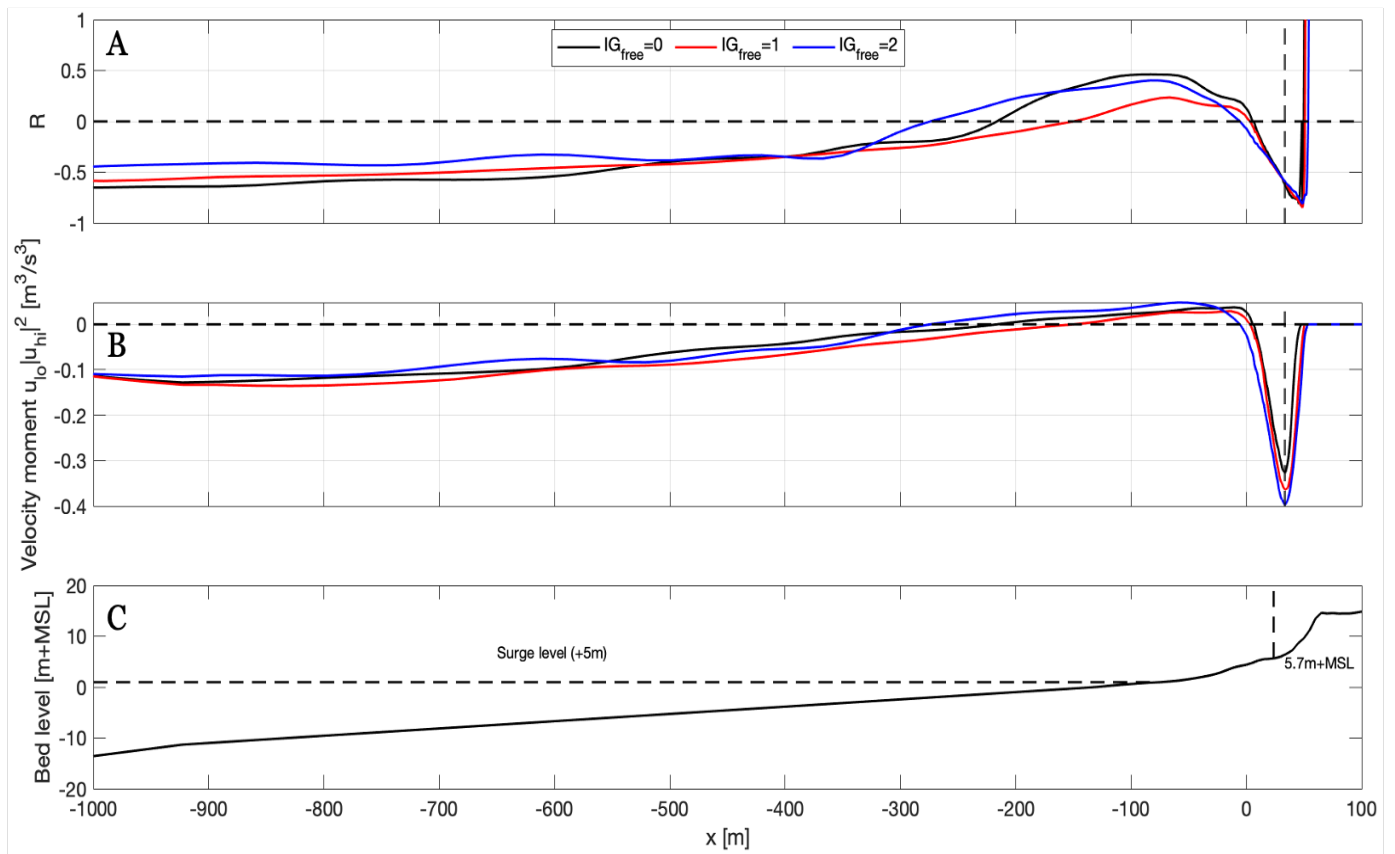


Figure 25: (A) Correlation between the u_{lo} and u_{hi}^2 ; (B) Velocity moment of the interaction between long wave velocity and short-wave velocity variance; (C) Step profile bed level. $IG_{free} = 0$ (black line), $IG_{free} = 1$ (red line), and $IG_{free} = 2$ (blue line).

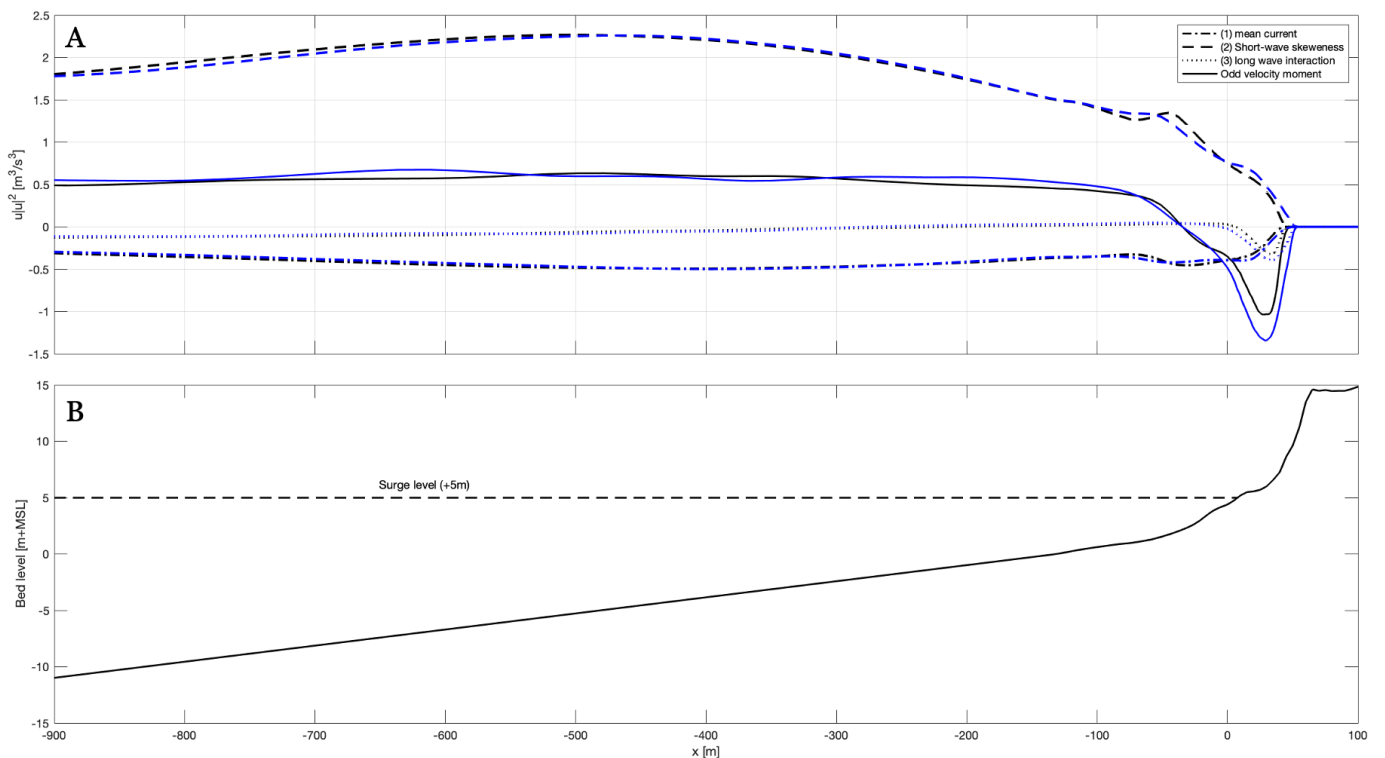


Figure 26: (A) Total odd velocity moments and their constituent components; black line represents $IG_{free} = 0$ and blue line represents $IG_{free} = 2$; (B) Mild profile bed level.

4.5 Steep and Mild Profile Comparison

Although similar cross-shore hydrodynamic patterns are observed between the steep and mild profiles, the impact of the added free long waves on dune erosion and runup for the steep profile are more pronounced. This is partially explained by the increased runup associated with the increased free long waves imposed at the boundary for both profiles. The wave runup levels associated with the long waves is tabulated in Table 9 and illustrated graphically in Figure 27.

From Figure 27 it is evident that the added free infragravity energy results in increased wave runup for both the mild and steep profiles. Although the 2% exceedance value is similar for the mild and steep profiles for the case when then the free infragravity energy is twice that of the bound energy ($IG_{free} = 2$), a considerable increase is observed in the maximum runup levels. The results demonstrate that although both profiles exhibited increased maximum runup levels with increasing free long wave energy, the increase is most pronounced on the steep profile. For the $IG_{free} = 2$ case a 29.4% increase in the maximum runup level is observed on the steep profile, compared with a 21.2% increase on the mild profile.

Table 9: Wave runup predictions for extreme storm conditions.

Profile	Maximum	$IG_{Free} = 0$	$IG_{Free} = 1$	$IG_{Free} = 2$
Mild	2% runup [m+MSL]	7.7	8.1	8.8
	% difference	NA	14.8	40.7
	Max. runup [m+MSL]	8.3	8.5	9.0
	% difference	NA	6.1	21.2
Steep	2% runup [m+MSL]	8.1	8.6	8.8
	% difference	NA	16.1	22.6
	Max. runup [m+MSL]	8.4	9.1	9.4
	% difference	NA	20.6	29.4

Further, the dune erosion profiles after the five-hour simulation under the extreme storm conditions for all three boundary conditions are presented in Figure 28 for the steep profile and Figure 29 for the mild profile. The area shaded in blue denotes the eroded sections of profile, while the red areas denote the accretion sections. With a surge level of +5m the wave attack follows the collision regime as the runup and wave attack collide with the dune above the dune-foot level (+3.00m). From panels A, B, and C of Figure 28 and Figure 29 it is evident that the erosion volume, highlighted in blue, increases with increasing long wave energy at the boundary. A summary of the dune erosion volumes per unit width for both profiles is presented in Table 10. The dune erosion volume increased

by 44.1% and 85.1% for the $IG_{free} = 1$ and $IG_{free} = 2$ cases respectively relative to the case excluding free infragravity energy for the steep profile. On the other hand, the eroded volumes for the mild profile increased by 36.4% and 58.1% for the $IG_{free} = 1$ and $IG_{free} = 2$ conditions respectively.

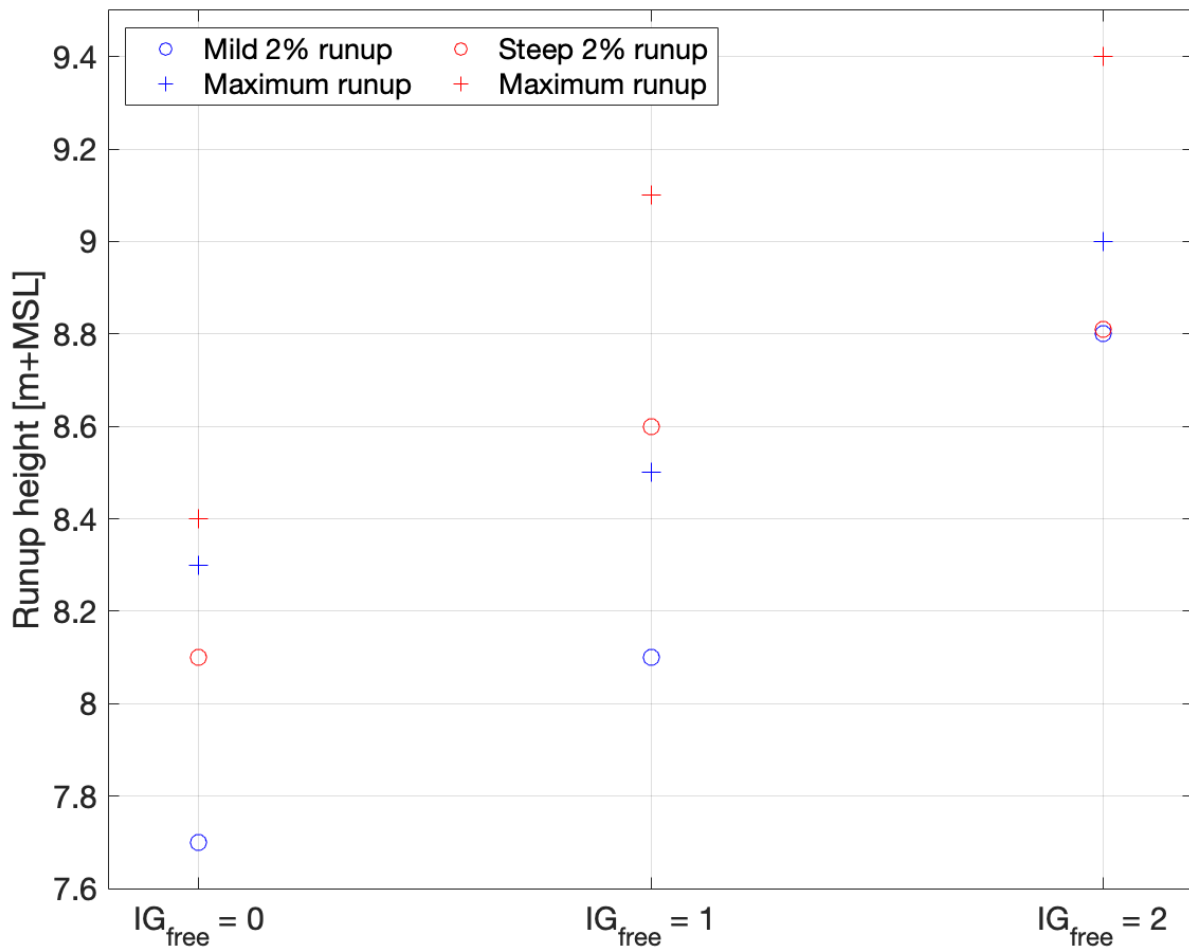


Figure 27: 2% exceedance (+) and maximum (o) runup predictions for extreme storm conditions; Mild profile shown in blue and steep profile shown in red.

Table 10: Dune erosion predictions for extreme storm conditions.

Profile	Maximum	$IG_{Free} = 0$	$IG_{Free} = 1$	$IG_{Free} = 2$
Mild	Dune erosion [m^3/m]	27.1	37.0	42.9
	% difference	NA	36.4	58.1
Steep	Dune erosion [m^3/m]	26.9	38.7	49.8
	% difference	NA	44.1	85.1

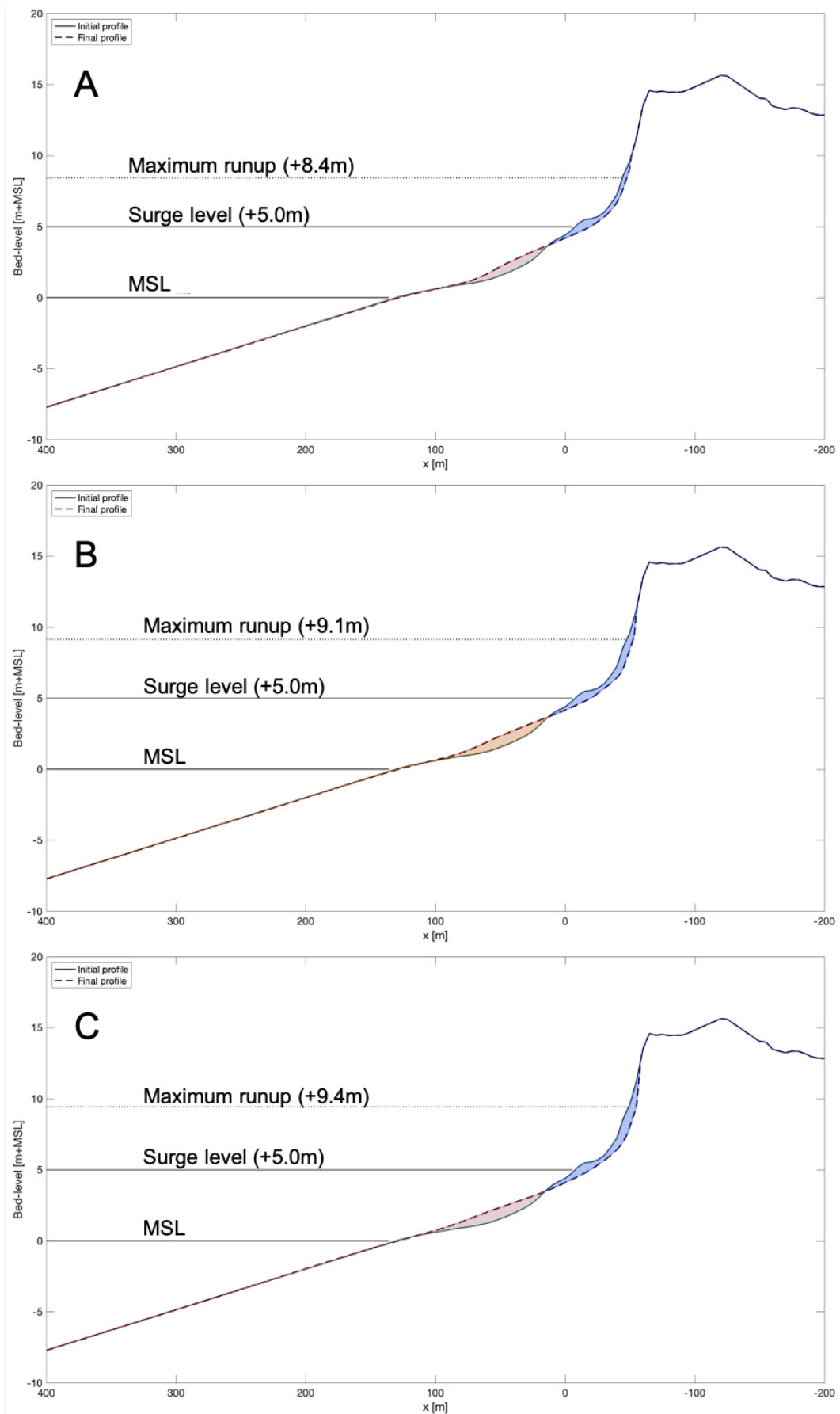


Figure 28: Step dune profile development for: (A) $IG_{free} = 0$, (B) $IG_{free} = 1$, (C) $IG_{free} = 2$ where blue shows erosion and red shows the accretion.

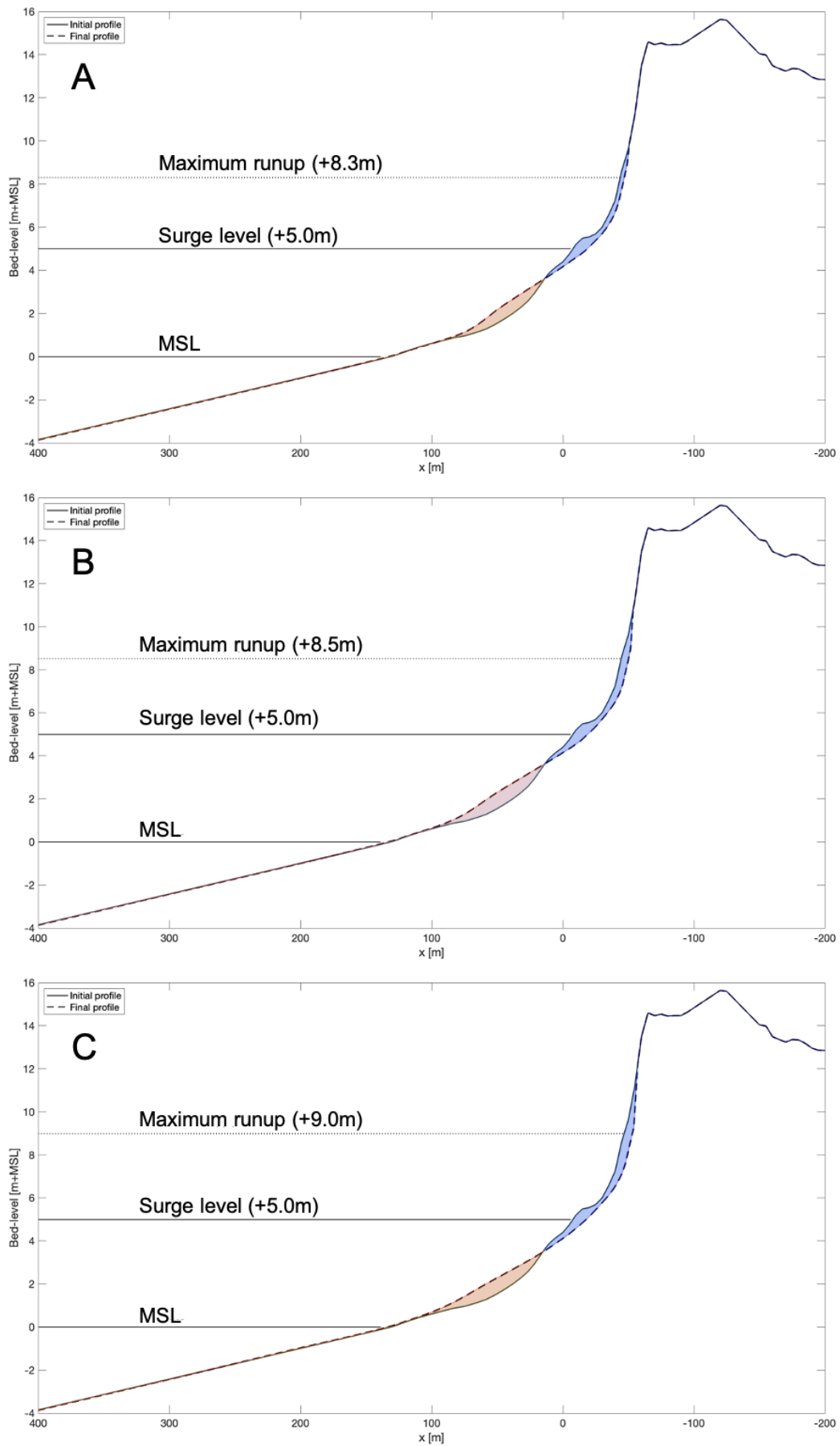


Figure 29: Mild dune profile development for: (A) $IG_{free} = 0$, (B) $IG_{free} = 1$, (C) $IG_{free} = 2$ where blue shows erosion and red shows the accretion.

5 Discussion

5.1 Phase I: Model-data comparison

In Phase I of the study an XBeach model was calibrated to recreate the conditions observed during the the October 24th, 1998 storm at Egmond aan Zee. The results show that by calibrating the roller breaker slope coefficient and breaker coefficient significant improvements in predicting long wave patterns in the surf zone are achieved. Setting the breaker slope coefficient to 0.15, breaker coefficient to 0.4, and directional width of the incoming waves to 30° the average root-mean square error in infragravity and short-wave predictions decreased by 0.13m and 0.05m respectively. In addition, the average skill increased to 0.69 and 0.73 for long and short-wave predictions respectively. The error in the short-wave predictions was largest at the most offshore sensor (7a) located on the seaward face of the outer bar. One possible explanation for the high error at sensor 7a is the high variation in the instantaneous short-wave energy and short-wave height observed across the duration of the storm. The temporal variation in the instantaneous wave height signal depicted in panel C of Figure 13 is caused by the subsequent arrival of wave groups. Furthermore, the relatively high error in predicting the short waves is partially due to the fact that in *Surfbeat* mode XBeach only resolves long waves. Short waves are not individually resolved therefore the asymmetry and skewness of propagating short waves in the surf zone is not captured by the model. This could lead to significant errors in short wave predictions in the surf zone. In addition, the 1D model does not fully resolve wave refraction. The lack of wave refraction in the surf zone partially explains the model's tendency to over-predict short wave energy during mild conditions. The 1D model also does not consider obliquely incident waves which could contribute to the errors between the model predictions and observations.

The model had the propensity to overpredicted the infragravity wave height during peak storm intensity as shown in Figure 15. Likewise, this observation is supported by the comparison of the predicted and observed infragravity wave heights shown in Figure 19. The scatter plot suggests that for relatively less energetic waves the predicted and observed infragravity waves are in good agreement. However, the model tends to overpredict the most energetic infragravity waves. This can be explained by several factors. The behaviour and growth of infragravity waves in the surf zone is influenced by both cross-shore and long-shore processes in the surf zone. In one-dimensional modelling long-shore processes such as long-shore currents and wave refraction are not fully resolved. In addition, overprediction is caused by the assumption that incoming infragravity waves

are exclusively bound waves produced by second-order equilibrium solutions. Further improvements in the predictions can be achieved by altering the offshore wave boundary conditions to better reflect the wave climate entering the domain. The boundary condition imposed at the wavemaker is characterized by the significant wave height and peak period measurements collected at the offshore directional wave buoy as part of the Coast-3D measurement campaign. The model imposes a JONSWAP spectrum characterized by the hourly significant wave height and peak period measurements and computes the underlying bound long waves following the K. Hasselmann (1962) method. However, as the storm grows in intensity the second-order equilibrium condition at the boundary will tend to over-estimate the incoming long wave energy. As a result, prediction improvements can be achieved by altering the boundary conditions.

The results of the comparison between the Coast-3D data and the model predictions suggest that the simulations typically explain about 70% of the measured infragravity and short-wave heights in the inner surf zone. The model however has the tendency to overpredict the infragravity wave energy even when the roller slope coefficient and breaker coefficient are calibrated. Ultimately, the XBeach *Surfbeat* model is shown to accurately recreate infragravity wave behaviour in the surfzone during a storm event. Therefore, the model is proven to be a robust platform to examine the impacts of imposing free long waves at the boundary on dune erosion predictions.

5.2 Phase II: Impact of Free Long Waves on Dune Erosion

Phase II of the study is primarily concerned with examining the impacts of free long waves on dune erosion predictions during storm events. The results presented in Table 10 show a significant increase in dune erosion with increasing free long wave energy for both the *steep* and *mild* profile. However, the results also suggest that the added free wave energy has a more pronounced effect on the *steep* slope. On a relatively mild slope the surfzone is wider meaning the effect of bottom friction is increased.

The increase in dune erosion volumes also coincides with increased maximum runup levels. As the waves run up higher up the dune face, avalanching becomes more prevalent. Avalanching is observed when the bed slope exceeds a pre-defined critical avalanching slope. If a cell has a bed slope which exceeds the critical slope, material is transferred to the adjacent cells to restore the slope to a stable value. It is considered that inundated sediments have a higher predisposition to slumping and therefore have a lower critical avalanching slope. Therefore, as the waves collide with

higher levels of the dune face the inundated sediments are more likely to slide down the dune face. Moreover, the cross-shore evolution of the third odd velocity moments demonstrate that the addition of free long waves at the boundary enhances the offshore directed long wave sediment transport contribution at the dune face.

In Addition, the results of Figure 23 and Figure 26 reveal that the contribution of the odd velocity moment between the long wave velocity and short wave velocity variance increase significantly when free long waves are imposed at the boundary. The direction of the bound long wave transport component to the total odd velocity moment is determined by the correlation between the long wave and short wave velocity signals, but the magnitude of the transport mechanism is determined by the product of the long wave velocity and short wave velocity variance. Although the correlation between the short and long wave velocity signals is similar for all three conditions the plots show that the long wave transport mechanism is enhanced by the increased velocities produced by the added free long waves.

The study reveals that the enhanced dune response is caused by increased runup at the shoreline and by the increase in the long wave contribution to the third odd velocity moment. Henceforth, the dune response is sensitive to changes in the offshore long wave boundary condition and is susceptible to considerable enhancement when incident free long waves are imposed at the boundary.

6 Conclusion

In phase I of this study the skill and ability of XBeach at predicting long wave hydrodynamics in the surf zone was evaluated by comparing the predictions to field observations during a storm event. The data was processed at several sensors across the profile within the surf zone to produce bulk wave estimates for long and short waves. Long wave estimates were produced by employing a spectral analysis of the water surface elevation signal at each sensor. The Coast-3D campaign provided valuable insight into the propagation and transformation of wave energy in the surf zone during a storm event.

Initially, the default Xbeach input parameters were used to produce a set of control results. Several parameters were calibrated to minimize the prediction errors, most prominently: the breaker slope coefficient for the roller model and the wave breaking coefficient. After several iterations, the root mean square error was reduced by 0.14m and 0.04m for the infragravity wave and short-wave predictions respectively. In addition, the skill factor for the infragravity and short-wave predictions improved to 0.69 and 0.73 respectively. The result of the optimization exercise revealed that Xbeach does have skill at predicting long waves during storm events. Furthermore, the study showed that Xbeach can accurately recreate the cross-shore evolution of infragravity wave energy observed during storm events. However, the model tends to overpredict long wave energy for high incoming short-wave energy and underpredicts the long wave energy for relatively low short-wave energy. Henceforth, Infragravity waves are overpredicted at the deepest sensors which recorded the highest incoming short-wave energy. Overall, the results of the first modelling exercise demonstrated that XBeach in *surbeat* mode is a suitable numerical model for recreating long wave patterns observed along the Dutch coast during storm events.

Phase II of the study was principally concerned with evaluating the effects of long wave boundary conditions on wave-runup and dune erosion predictions at the shoreline. Two planar beach profiles were considered, a *steep* profile ($\beta \sim 0.4$), and relatively *mild* profile ($\beta \sim 0.2$). The simulations were run with the WTI settings optimized for morphological modeling along the Dutch coast coupled with a surface elevation time series boundary condition. Three iterations of the boundary conditions were considered:

- $IG_{free} = 0$: Excluding free infragravity waves at the boundary, which served as the control simulation.
- $IG_{free} = 1$: Including free infragravity wave energy equal to the bound long wave energy.
- $IG_{free} = 2$: Including free infragravity wave energy equal to double the bound long wave energy.

The results for both the *steep* and *mild* profiles demonstrated that the inclusion of free infragravity waves at the domain boundary resulted in remarkable increases in the maximum wave runup and dune erosion at the coastline. The $IG_{free} = 1$ simulation yielded a 44.1% and 36.4% increase in dune erosion volume for the *steep* and *mild* profiles respectively, while the $IG_{free} = 2$ simulation yielded an 85.1% and 58.1% increase in eroded dune volume for the *steep* and *mild* profiles respectively.

The results suggest that the dune response is sensitive to changes in offshore infragravity wave boundary conditions. It is imperative to note that the dune erosion volumes produced by the simulations in XBeach are overpredicted as the model tends to overpredict the long wave energy during storm conditions. The relative enhancement of the dune response to the imposed free long waves is thus the most principal outcome of the study. Further, the results demonstrate that the increase in dune response is mainly due to the increased runup levels and enhanced long wave transport mechanism close to the shoreline.

Previous studies such as Naporowski (2020) have shown that the contribution of bound long wave energy during a storm event represents about 60% of the total long wave energy. Hence, one can expect the dune response of $IG_{free} = 1$ tests to be more representative of conditions expected at the Dutch coastline during storm events.

7 Recommendations

Imposing free infragravity waves at the model boundary resulted in a considerable increase in the morphodynamic response at the shoreline. The North Sea is a semi-confined basin in which strong storms are repeatedly observed. Furthermore, several studies have noted the prevalence of free infragravity waves in the North Sea and have described the ability of free waves to propagate long distances relatively unhindered in basins with gradual bed level changes. Henceforth, it is critical to consider the contribution of free waves to wave runup and dune erosion predictions in numerical models. Although Rijkswaterstaat possesses a large database of information valuable to infragravity wave analysis and prediction, efforts should be diverted in simplifying the process of data collection in order for the data to be readily available for coastal modelers. Also, resources can be invested in improving the quality of the field measurements to include directional information. This could allow for the distinction between free and bound long waves and could improve predictions in the directional spreading of the wave spectrum. Including a more complete representation of the observed wave climate at a model boundary would result in more robust and reliable predictions of dune failure and inundation and allow for a more comprehensive understanding of dune behavior during storms.

In order to better understand the evolution of long waves in the surf zone it is also critical to consider wave reflection at the shoreline. Following the method by Sheremet et al. (2002) the incoming and outgoing infragravity energy fluxes and the corresponding reflection coefficient at the shoreline can be computed. Distinguishing between the incoming and outgoing long wave energy flux in the surf zone can improve predictions, and further explain the dynamics of long waves in the surf zone.

Likewise expanding the model to a 2DH model can potentially yield improved results by resolving longshore currents and directional spreading. Furthermore, 2D models can resolve wave refraction in the surf zone which can improve short wave predictions. Obliquely incident short and long waves can also be considered in a 2D model. Currently, the 1D model only considers normally incident free long waves. However, the incoming free long waves generated at distant sources may be obliquely incident. Testing the impact of free infragravity waves for milder storms and milder beach slopes can help portray a more comprehensive understanding of infragravity wave dynamics in the surfzone.

8 Appendix A: Model Results for the October 24, 1998 Storm Event

The full set of results and input variables for the Phase I study are presented here.

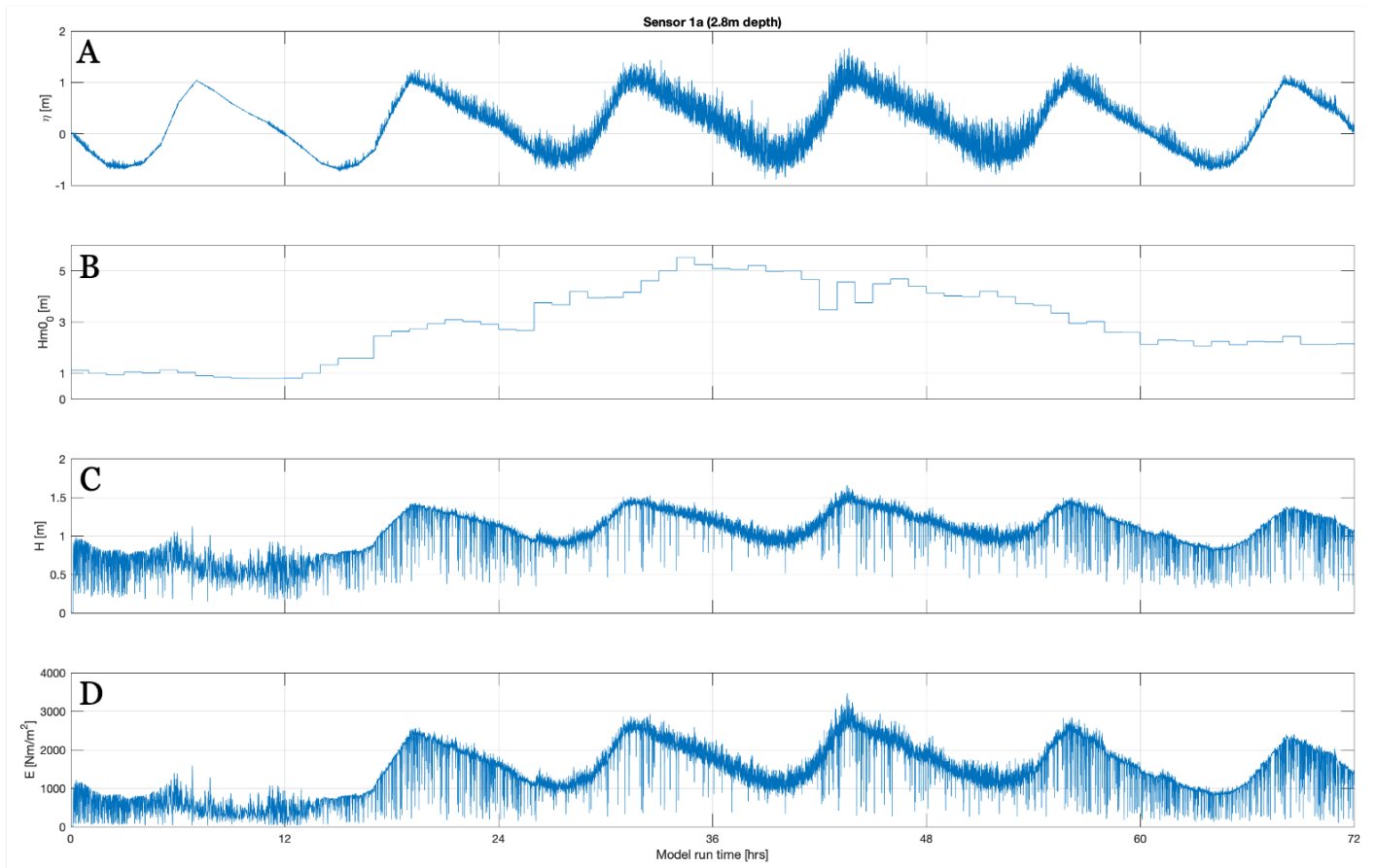


Figure 30: (A) Low frequency water surface elevation; (B) Offshore wave height; (C) instantaneous short wave height; and (D) instantaneous wave energy time series for sensor 1a.

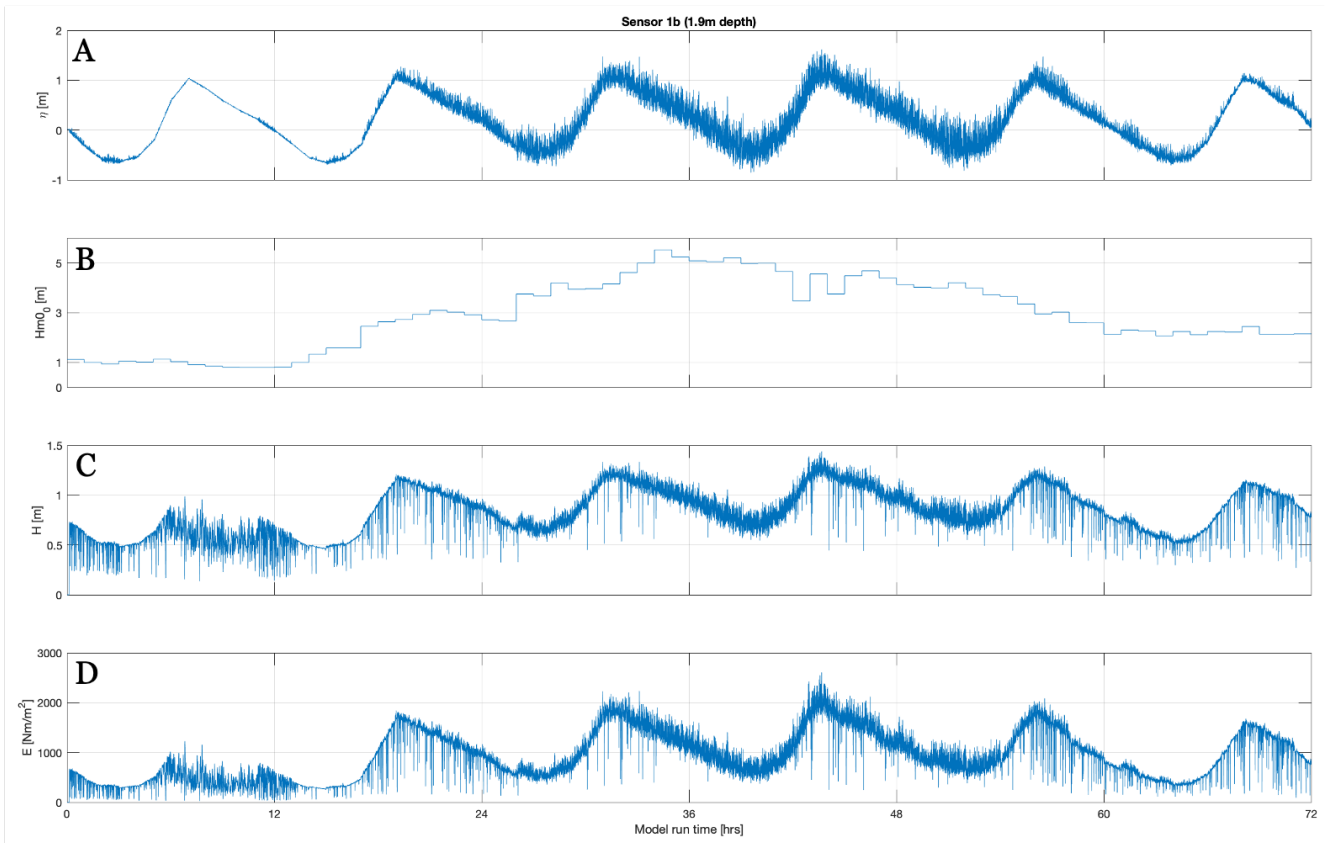


Figure 31: (A) Low frequency water surface elevation; (B) Offshore wave height; (C) instantaneous short wave height; and (D) instantaneous wave energy time series for sensor 1b.

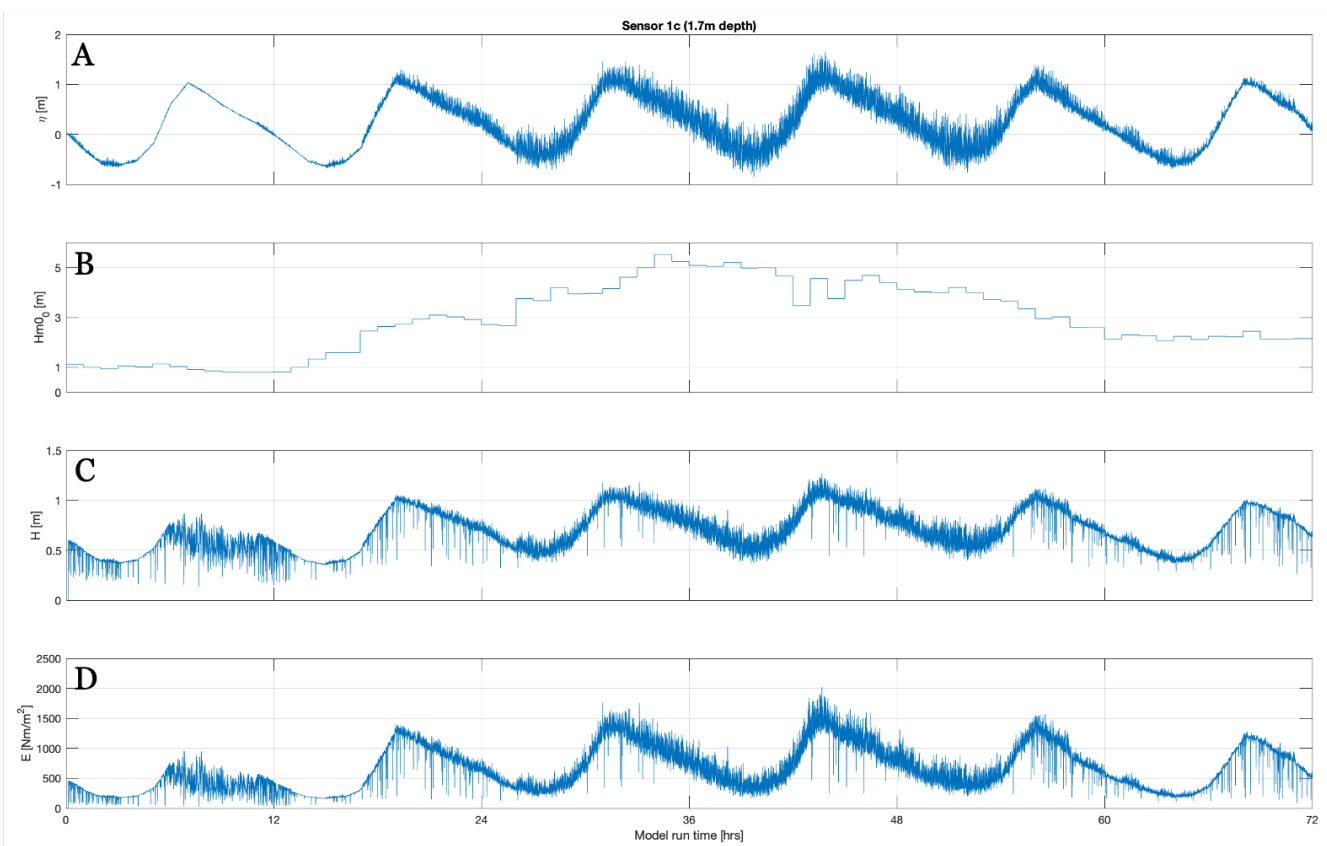


Figure 32: (A) Low frequency water surface elevation; (B) Offshore wave height; (C) instantaneous short wave height; and (D) instantaneous wave energy time series for sensor 1c.

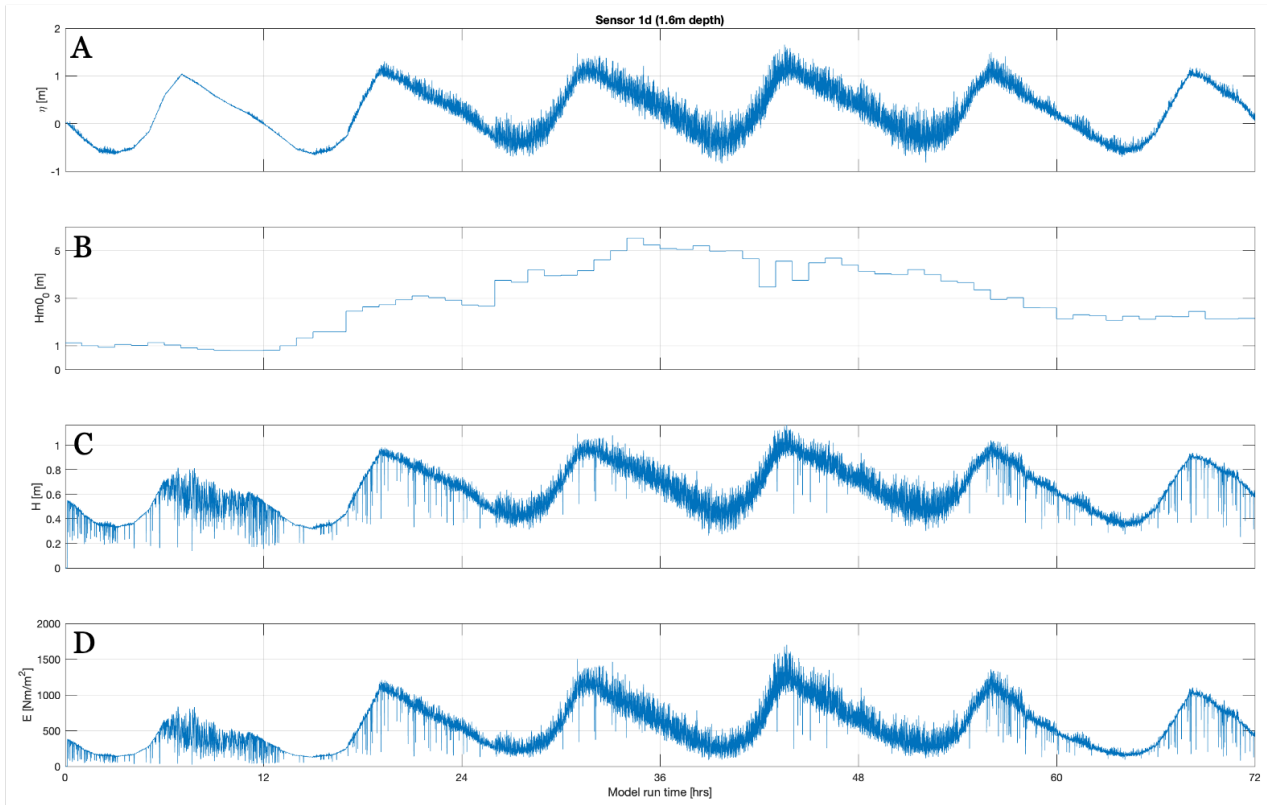


Figure 33: (A) Low frequency water surface elevation; (B) Offshore wave height; (C) instantaneous short wave height; and (D) instantaneous wave energy time series for sensor 1d.

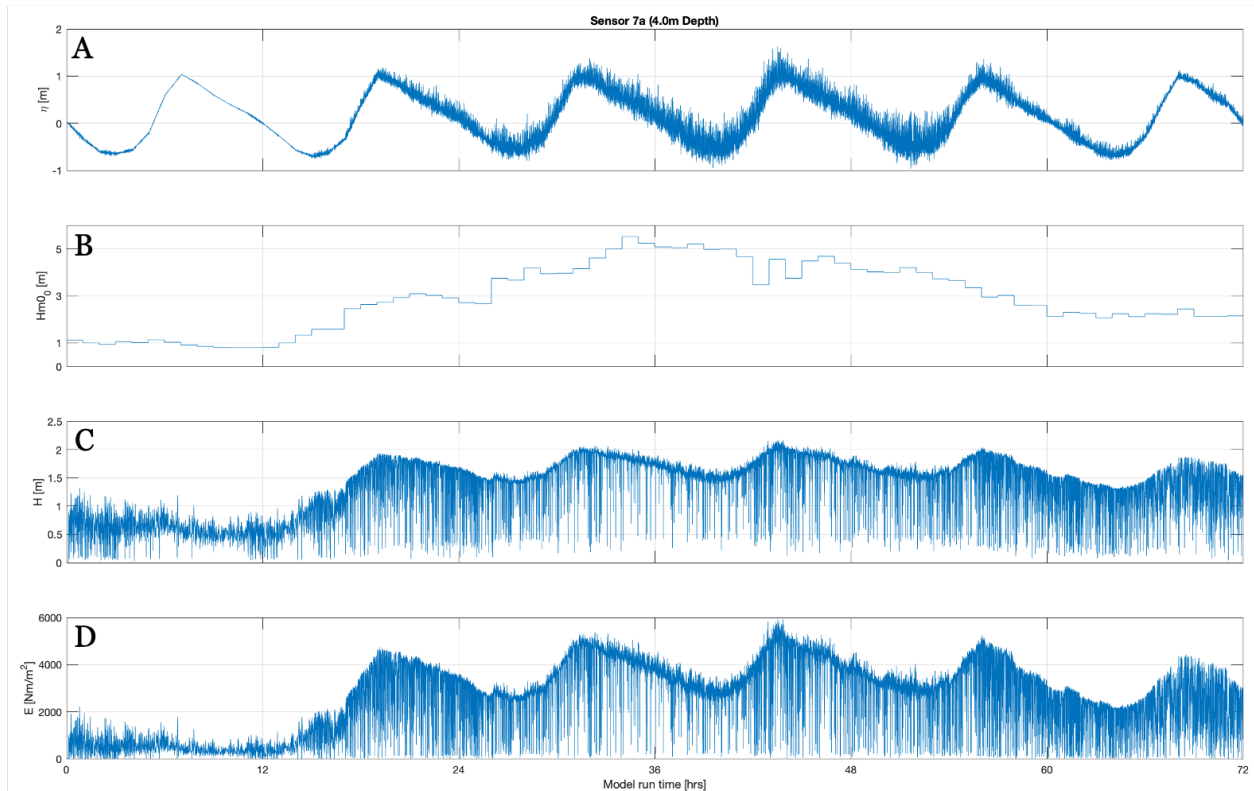


Figure 34: (A) Low frequency water surface elevation; (B) Offshore wave height; (C) instantaneous short wave height; and (D) instantaneous wave energy time series for sensor 7a.

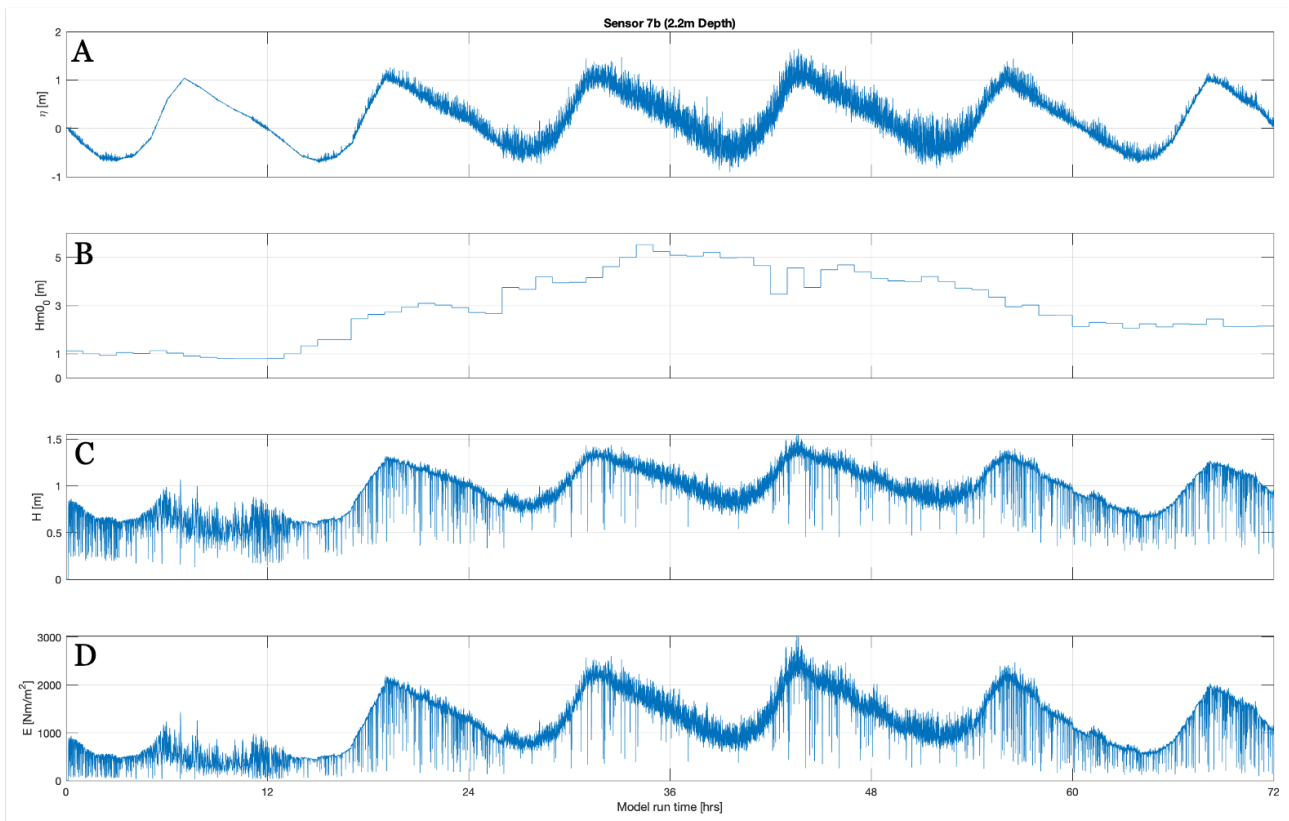


Figure 35: (A) Low frequency water surface elevation; (B) Offshore wave height; (C) instantaneous short wave height; and (D) instantaneous wave energy time series for sensor 7b.

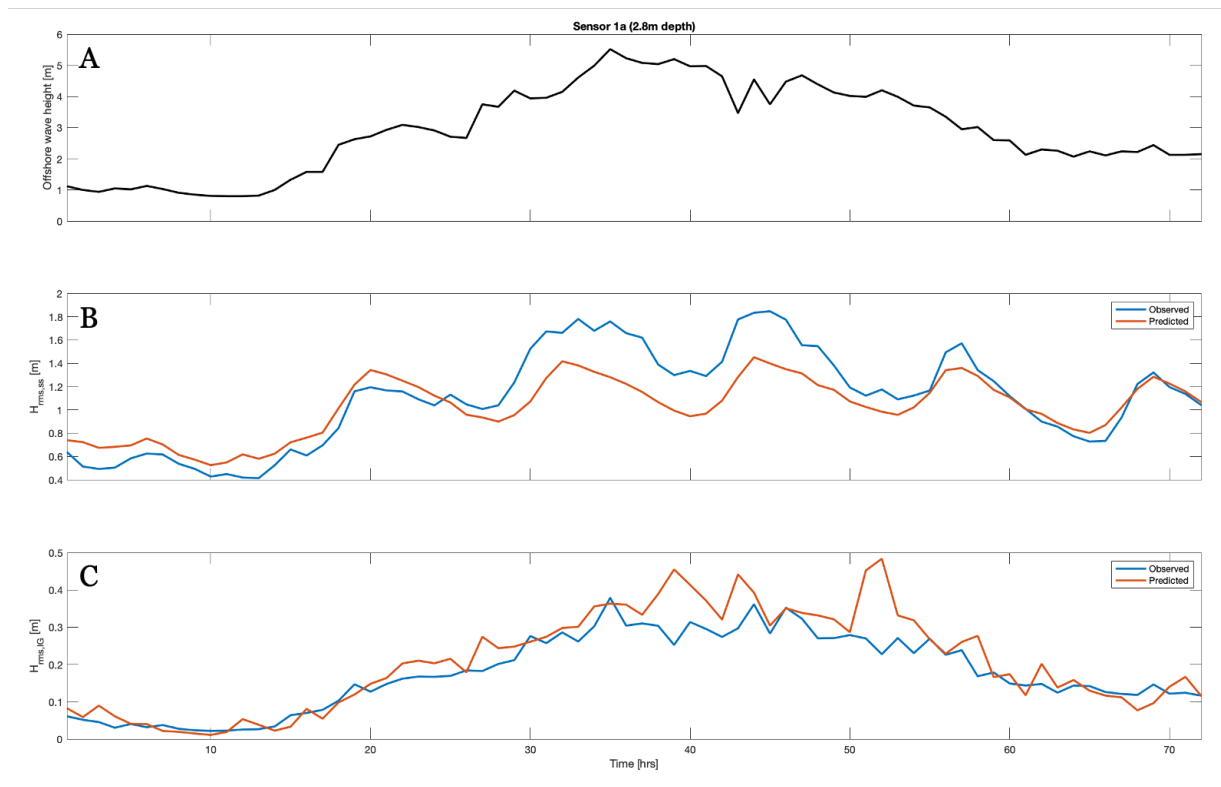


Figure 36: (A) Offshore wave height; (B) Predicted and observed short rms wave height; and (C) Predicted and observed infragravity rms wave heights at the seaward face of the inner bar at sensor 1a.

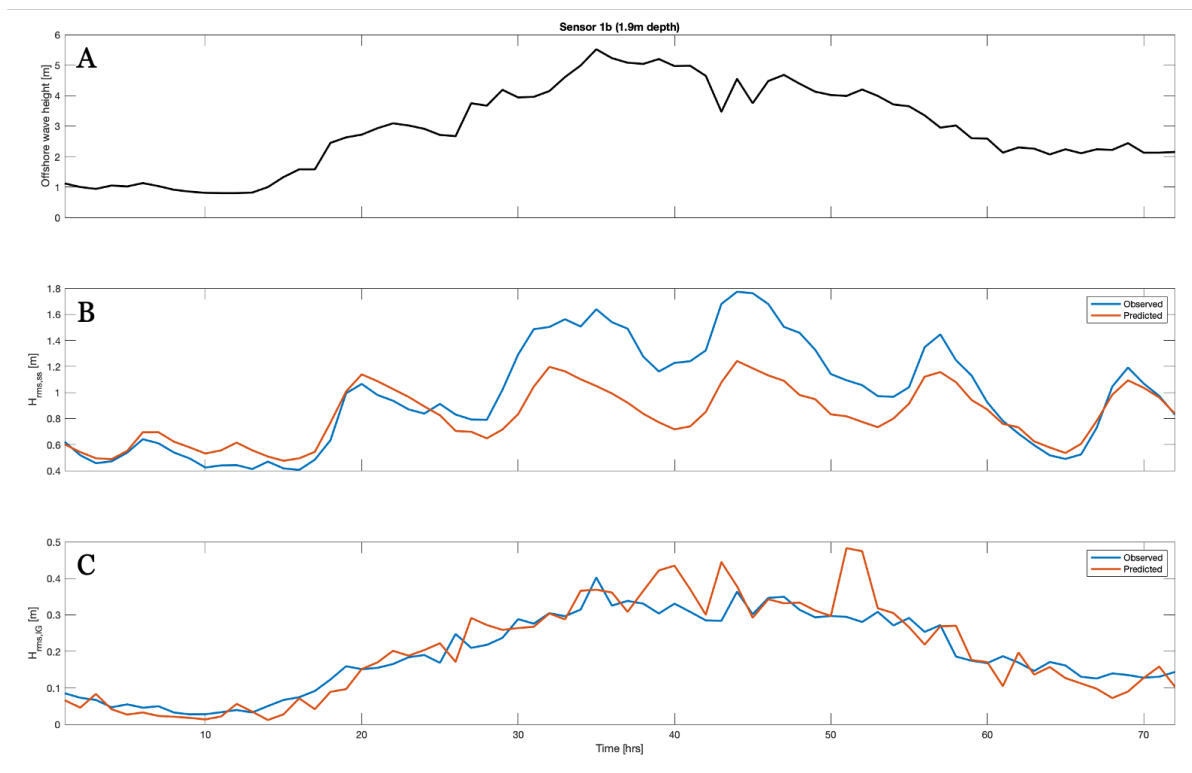


Figure 37: (A) Offshore wave height; (B) Predicted and observed short rms wave height; and (C) Predicted and observed infragravity rms wave heights at the seaward face of the inner bar at sensor 1b.

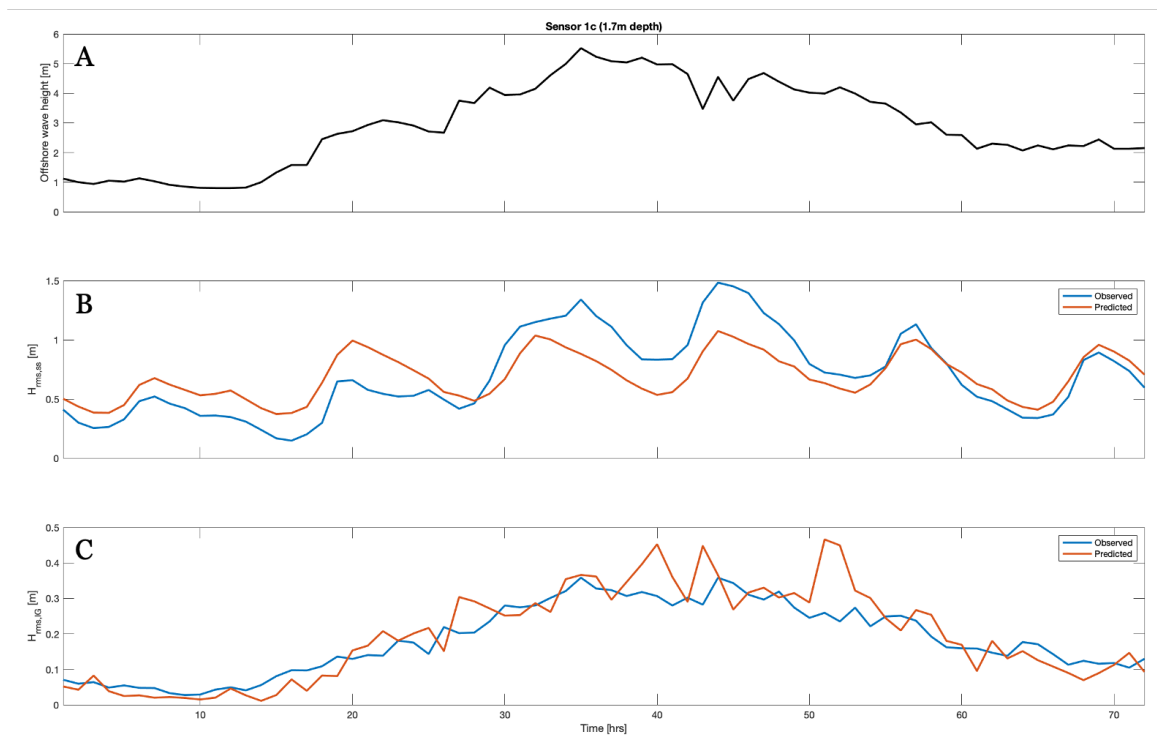


Figure 38: (A) Offshore wave height; (B) Predicted and observed short rms wave height; and (C) Predicted and observed infragravity rms wave heights at the seaward face of the inner bar at sensor 1c.

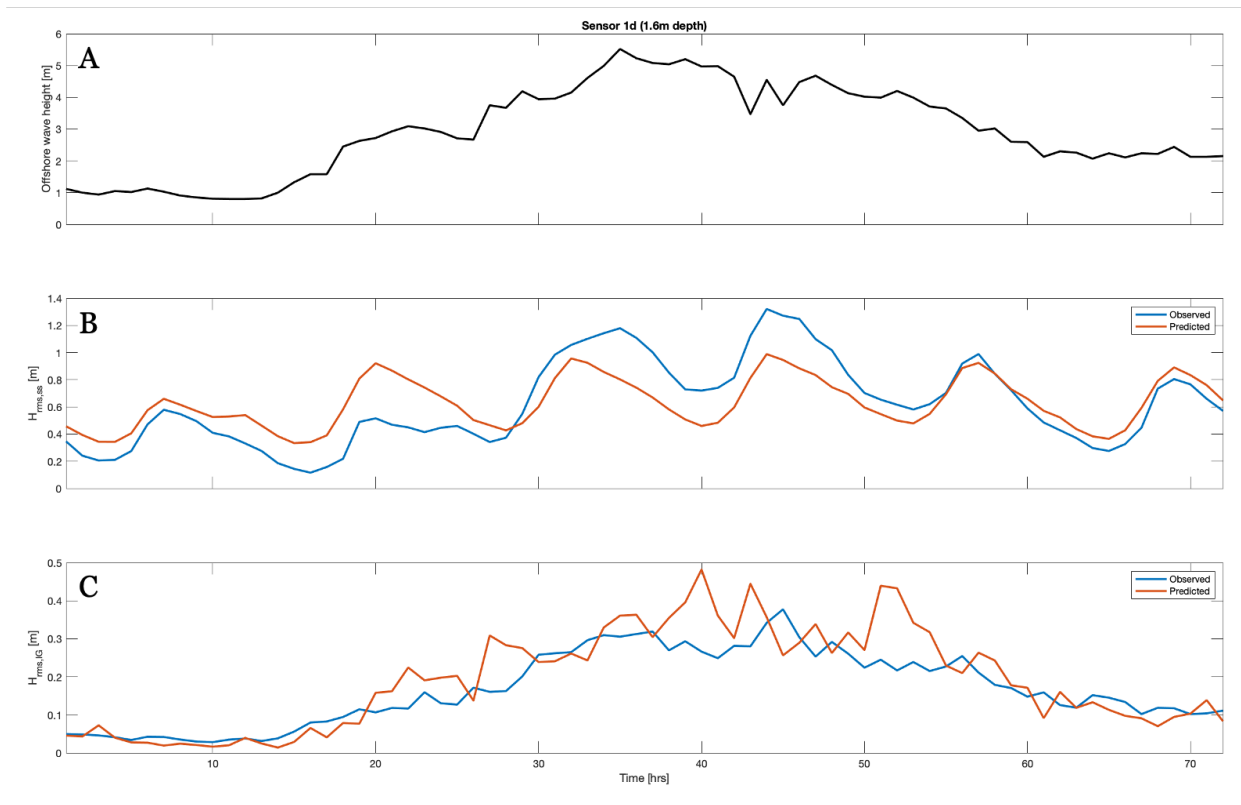


Figure 39: (A) Offshore wave height; (B) Predicted and observed short rms wave height; and (C) Predicted and observed infragravity rms wave heights at the seaward face of the inner bar at sensor 1c.

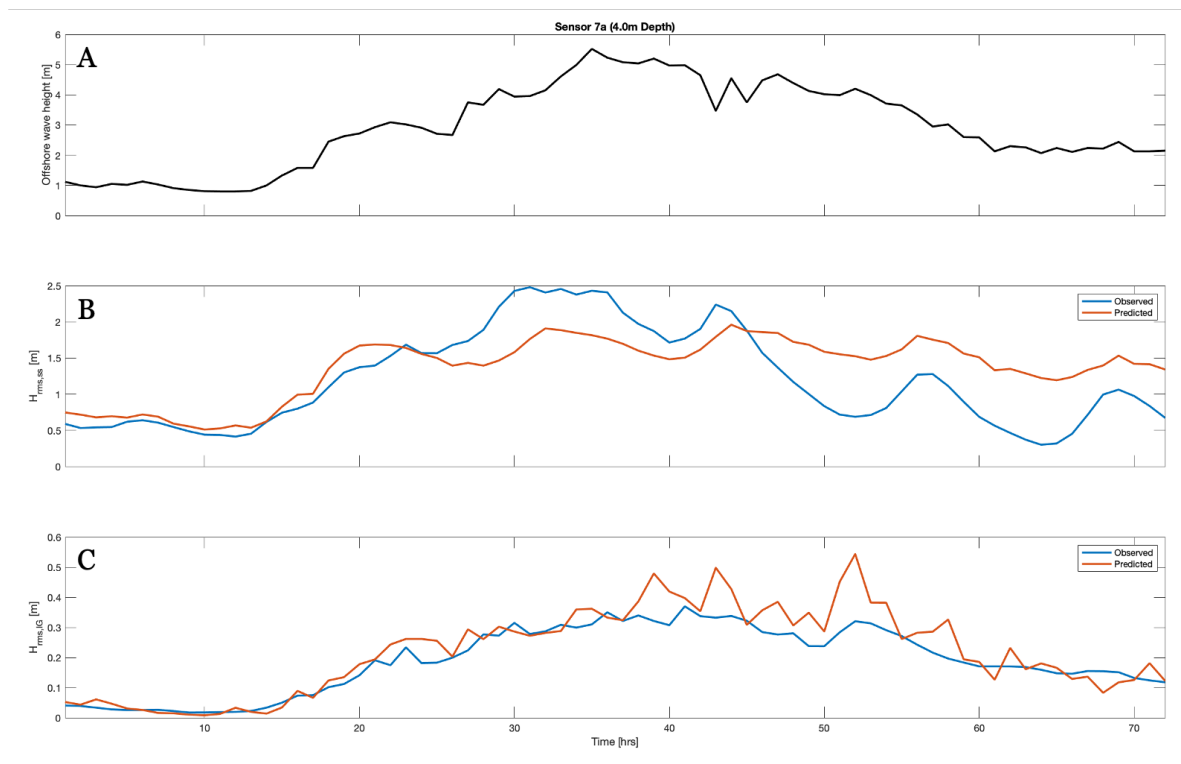


Figure 40: (A) Offshore wave height; (B) Predicted and observed short rms wave height; and (C) Predicted and observed infragravity rms wave heights at the seaward face of the inner bar at sensor 7a.

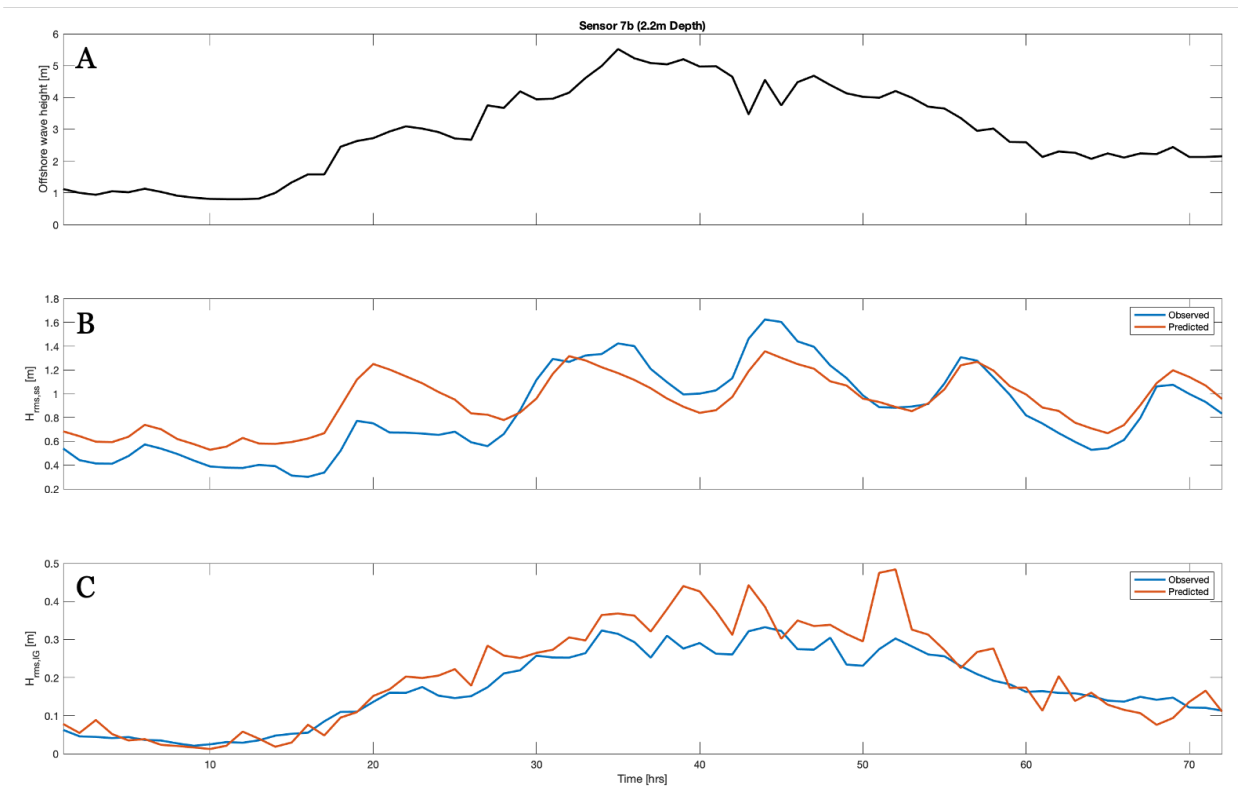


Figure 41: (A) Offshore wave height; (B) Predicted and observed short rms wave height; and (C) Predicted and observed infragravity rms wave heights at the seaward face of the inner bar at sensor 7b.

References

- A.H. Sallenger, Jr. (2000). Storm Impact Scale for Barrier Islands. *Journal of Coastal Research*, 16(3), 890-895. Retrieved from <http://www.jstor.org/stable/4300099>
- Ardhuin, F., Rawat, A., & Aucan, J. (2014). A numerical model for free infragravity waves: Definition and validation at regional and global scales. *Ocean Modelling*, 77, 20-32. doi:<https://doi.org/10.1016/j.ocemod.2014.02.006>
- Battjes, J. A., Bakkenes, H. J., Janssen, T. T., & van Dongeren, A. R. (2004). Shoaling of subharmonic gravity waves. *Journal of Geophysical Research: Oceans*, 109(C2). doi:10.1029/2003jc001863
- Battjes, J. A., & Janssen, J. P. F. M. (1978). Energy Loss and Set-Up Due to Breaking of Random Waves. In *Coastal Engineering 1978* (pp. 569-587).
- Bertin, X., de Bakker, A., van Dongeren, A., Coco, G., André, G., Ardhuin, F., . . . Tissier, M. (2018). Infragravity waves: From driving mechanisms to impacts. *Earth-Science Reviews*, 177, 774-799. doi:<https://doi.org/10.1016/j.earscirev.2018.01.002>
- Biésel, F. (1952). EQUATIONS GÉNÉRALES AU SECOND ORDRE DE LA HOULE IRRÉGULIÈRE. *La Houille Blanche*(3), 372-376. Retrieved from <https://doi.org/10.1051/lhb/1952033>
- Bosboom, J., & Stive, M. J. F. (2015). *Coastal Dynamics 1*: Delft Academic Press.
- Bromirski, P. D., Sergienko, O. V., & MacAyeal, D. R. (2010). Transoceanic infragravity waves impacting Antarctic ice shelves. *Geophysical Research Letters*, 37(2). doi:10.1029/2009gl041488
- Deigaard, R., Jakobsen, J. B., & Fredsøe, J. (1999). Net sediment transport under wave groups and bound long waves. *Journal of Geophysical Research: Oceans*, 104(C6), 13559-13575. doi:10.1029/1999jc900072
- Do, K., Shin, S., Cox, D., & Yoo, J. (2018). Numerical Simulation and Large-Scale Physical Modelling of Coastal Sand Dune Erosion. *Journal of Coastal Research*, 85, 196-200. doi:10.2112/SI85-040.1
- Duncan, J. H. (1981). An Experimental Investigation of Breaking Waves Produced by a Towed Hydrofoil. *Proceedings of the Royal Society of London. Series A, Mathematical and Physical Sciences*, 377(1770), 331-348. Retrieved from <http://www.jstor.org/stable/2397189>
- Fiedler, J. W., Smit, P. B., Brodie, K. L., McNinch, J., & Guza, R. T. (2019). The offshore boundary condition in surf zone modeling. *Coastal Engineering*, 143, 12-20. doi:<https://doi.org/10.1016/j.coastaleng.2018.10.014>
- Galappatti, R. (1983). A depth integrated model for suspended transport. *Journal for Hydraulic Research*, 23, 359-377.

- Gallagher, E. L., Elgar, S., & Guza, R. T. (1998). Observations of sand bar evolution on a natural beach. *Journal of Geophysical Research: Oceans*, 103(C2), 3203-3215. doi:10.1029/97jc02765
- Geer, P. v., Bieman, J. D., Hoonhout, B., & Boers, M. (2015). *XBeach 1D - Probabilistic model: ADIS, settings, Model Uncertainty and Graphical User Interface*. Retrieved from
- Guza, R., & Thornton, E. (1982). Swash Oscillations on a Natural Beach. *Journal of Geophysical Research*, 87, 483-491. doi:10.1029/JC087iC01p00483
- Hasselmann, K. (1962). On the non-linear energy transfer in a gravity-wave spectrum Part 1. General theory. *Journal of Fluid Mechanics*, 12(4), 481-500. doi:10.1017/S0022112062000373
- Hasselmann, K. (1963). A statistical analysis of the generation of microseisms. *Reviews of Geophysics*, 1(2), 177-210. doi:10.1029/RG001i002p00177
- Hasselmann, K., Barnett, T., Bouws, E., Carlson, H., Cartwright, D., Enke, K., . . . Walden, H. (1973). Measurements of wind-wave growth and swell decay during the Joint North Sea Wave Project (JONSWAP). *Deut. Hydrogr. Z.*, 8, 1-95.
- Heijer, K. d. (2012). *Sensitivity of Dune Erosion Prediction During Extreme Conditions*. Paper presented at the 4th International Conference on Estuaries and Coasts, Water Resources University, Vietnam.
- Herbers, T. H. C., Elgar, S., Guza, R. T., & O'Reilly, W. C. (1995). Infragravity-Frequency (0.005–0.05 Hz) Motions on the Shelf. Part II: Free Waves. *Journal of Physical Oceanography*, 25(6), 1063-1079. doi:10.1175/1520-0485(1995)025<1063:Ifhmot>2.0.Co;2
- Holthuijsen, L. H. (2007). *Waves in Oceanic and Coastal Waters*. Cambridge: Cambridge University Press.
- Holthuijsen, L. H., Booij, N., & Herbers, T. H. C. (1989). A prediction model for stationary, short-crested waves in shallow water with ambient currents. *Coastal Engineering*, 13(1), 23-54. doi:[https://doi.org/10.1016/0378-3839\(89\)90031-8](https://doi.org/10.1016/0378-3839(89)90031-8)
- Huntley, D., & Bowen, A. (1975). Comparison of the hydrodynamics of steep and shallow beaches. In *Nearshore sediment dynamics and sedimentation* (pp. 69-109): Wiley London.
- Kannberg, J. F. (2018). *Wave Runup and Infragravity Energy in the Surf Zone*. University of California, San Diego.
- Longuet-Higgins, M. S., & Stewart, R. W. (1962). Radiation stress and mass transport in gravity waves, with application to 'surf beats'. *Journal of Fluid Mechanics*, 13(4), 481-504. doi:10.1017/S0022112062000877
- Longuet-Higgins, M. S., & Turner, J. S. (1974). An 'entraining plume' model of a spilling breaker. *Journal of Fluid Mechanics*, 63(1), 1-20. doi:10.1017/S002211207400098X
- Munk, W. H. (1949). Surf beats. *Eos, Transactions American Geophysical Union*, 30(6), 849-854. doi:10.1029/TR030i006p00849

- Nairn, R. B., Roelvink, J. A., & Southgate, H. N. (1991). Transition Zone Width and Implications for Modelling Surfzone Hydrodynamics. In *Coastal Engineering 1990* (pp. 68-81).
- Naporowski, R. (2020). *Long waves in the North Sea: Distribution, generation and measurement methods*. Delft University of Technology, Delft, The Netherlands. Retrieved from <http://resolver.tudelft.nl/uuid:833a3284-e37c-463f-91c9-9e705eaf94a6>
- Rawat, A., Arduin, F., Ballu, V., Crawford, W., Corela, C., & Aucan, J. (2014). Infragravity waves across the oceans. *Geophysical Research Letters*, *41*(22), 7957-7963. doi:10.1002/2014gl061604
- Reniers, A., Roelvink, D., & Dongeren, A. v. (2001). Morphodynamic Response to Wave Group Forcing. In *Coastal Engineering 2000* (pp. 3218-3228).
- Reniers, A. J. H. M., & Battjes, J. A. (1997). A laboratory study of longshore currents over barred and non-barred beaches. *Coastal Engineering*, *30*(1), 1-21. doi:[https://doi.org/10.1016/S0378-3839\(96\)00033-6](https://doi.org/10.1016/S0378-3839(96)00033-6)
- Reniers, A. J. H. M., van Dongeren, A. R., Battjes, J. A., & Thornton, E. B. (2002). Linear modeling of infragravity waves during Delilah. *Journal of Geophysical Research: Oceans*, *107*(C10), 1-1-1-18. doi:10.1029/2001jc001083
- Rijn, L. C. v. (2007). Unified View of Sediment Transport by Currents and Waves. I: Initiation of Motion, Bed Roughness, and Bed-Load Transport. *Journal of Hydraulic Engineering*, *133*(6), 649-667. doi:doi:10.1061/(ASCE)0733-9429(2007)133:6(649)
- Rijnsdorp, D. P., Ruessink, G., & Zijlema, M. (2015). Infragravity-wave dynamics in a barred coastal region, a numerical study. *Journal of Geophysical Research: Oceans*, *120*(6), 4068-4089. doi:10.1002/2014jc010450
- Roelvink, D., Reniers, A., van Dongeren, A., van Thiel de Vries, J., McCall, R., & Lescinski, J. (2009). Modelling storm impacts on beaches, dunes and barrier islands. *Coastal Engineering*, *56*(11), 1133-1152. doi:<https://doi.org/10.1016/j.coastaleng.2009.08.006>
- Roelvink, D. J. A., & Reniers, A. (2011). *A Guide to Modeling Coastal Morphology*.
- Roelvink, J. A. (1993). Dissipation in random wave groups incident on a beach. *Coastal Engineering*, *19*(1), 127-150. doi:[https://doi.org/10.1016/0378-3839\(93\)90021-Y](https://doi.org/10.1016/0378-3839(93)90021-Y)
- Roelvink, J. A., & Stive, M. J. F. (1989). Bar-generating cross-shore flow mechanisms on a beach. *Journal of Geophysical Research: Oceans*, *94*(C4), 4785-4800. doi:10.1029/JC094iC04p04785
- Ruessink, B. G., Miles, J. R., Feddersen, F., Guza, R. T., & Elgar, S. (2001). Modeling the alongshore current on barred beaches. *Journal of Geophysical Research: Oceans*, *106*(C10), 22451-22463. doi:10.1029/2000jc000766
- Ruessink, B. G., van Enckevort, I. M. J., Kingston, K. S., & Davidson, M. A. (2000). Analysis of observed two- and three-dimensional nearshore bar behaviour. *Marine Geology*, *169*(1), 161-183. doi:[https://doi.org/10.1016/S0025-3227\(00\)00060-8](https://doi.org/10.1016/S0025-3227(00)00060-8)

- Sheremet, A., Guza, R. T., Elgar, S., & Herbers, T. H. C. (2002). Observations of nearshore infragravity waves: Seaward and shoreward propagating components. *Journal of Geophysical Research: Oceans*, *107*(C8), 10-11-10-10. doi:10.1029/2001jc000970
- Stive, M. J. F., & Vriend, H. J. d. (1995). Shear Stresses and Mean Flow in Shoaling and Breaking Waves. In *Coastal Engineering 1994* (pp. 594-608).
- Stockdon, H. F., Holman, R. A., Howd, P. A., & Sallenger, A. H. (2006). Empirical parameterization of setup, swash, and runup. *Coastal Engineering*, *53*(7), 573-588. doi:<https://doi.org/10.1016/j.coastaleng.2005.12.005>
- Svendsen, I. A. (1984). Wave heights and set-up in a surf zone. *Coastal Engineering*, *8*(4), 303-329. doi:[https://doi.org/10.1016/0378-3839\(84\)90028-0](https://doi.org/10.1016/0378-3839(84)90028-0)
- Symonds, G., Huntley, D., & Bowen, A. (1982). Two-Dimensional Surf Beat: Long Wave Generation by a Time-Varying Breakpoint. *Journal of Geophysical Research*, *87*, 492-498. doi:10.1029/JC087iC01p00492
- Tucker, M. J., & Deacon, G. E. R. (1950). Surf beats: sea waves of 1 to 5 min. period. *Proceedings of the Royal Society of London. Series A. Mathematical and Physical Sciences*, *202*(1071), 565-573. doi:doi:10.1098/rspa.1950.0120
- van Dongeren, A., Battjes, J., Janssen, T., van Noorloos, J., Steenhauer, K., Steenbergen, G., & Reniers, A. (2007). Shoaling and shoreline dissipation of low-frequency waves. *Journal of Geophysical Research: Oceans*, *112*(C2). doi:10.1029/2006jc003701
- Van Geer, P., Den Bieman, J., Hoonhout, B., & Boers, M. (2015). XBeach 1D—Probabilistic model: ADIS, Settings, Model uncertainty and Graphical User Interface. *Tec. Rep*, 1209436-1209002.
- van Thiel de Vries, J. (2009). *Dune Erosion During Storm Surges*. (PhD). Delft University of Technology,
- Vellinga, P. (1982). Beach and dune erosion during storm surges. *Coastal Engineering*, *6*(4), 361-387. doi:[https://doi.org/10.1016/0378-3839\(82\)90007-2](https://doi.org/10.1016/0378-3839(82)90007-2)
- Whitham, G. B. (1965). A general approach to linear and non-linear dispersive waves using a Lagrangian. *Journal of Fluid Mechanics*, *22*(2), 273-283. doi:10.1017/S0022112065000745
- Willard J. Pierson, Jr., John, J. T., & John, A. W. (1952). THE THEORY OF THE REFRACTION OF A SHORT CRESTED GAUSSIAN SEA SURFACE WITH APPLICATION TO THE NORTHERN NEW JERSEY COAST. *Coastal Engineering Proceedings*, *1*(3). doi:10.9753/icce.v3.8